ABSTRACT

WANG, JIAXIN. Monte Carlo Optimization of Coincidence Prompt Gamma-Ray Neutron Activation Analysis**.** (Under the direction of Professor Robin P. Gardner.)

Prompt Gamma-Ray Neutron Activation Analysis (PGNAA) is a non-destructive, rapid on-line method for determination of the elemental composition of bulk coal and other granular solid samples. However, PGNAA has an inherently large background due to the neutron source, natural radioactivity and non-sample response. Introducing the gamma-gamma coincidence technology into PGNAA could highly suppress all interference and eliminate some entirely. To overcome or alleviate the main drawback of coincidence PGNAA, which is a low coincidence counting rate, the system has to be optimized. This optimization at present relies on Monte Carlo simulation. The CEARCPG specific purpose code is the first and only code that is now available to simulate the normal and coincidence spectra of PGNAA. The MCNP5 code has been used in parameter study, dose rate and other suitable parts of this work.

To achieve a better accuracy and efficiency, the detector response function (DRF) used in CEARCPG has been updated with DRFs that generated by a new code named CEARDRFs. CEARDRFs can generate relatively accurate detector response functions for cylindrical or rectangular NaI and BGO detectors in speed that are hundreds of times faster than MCNP5. CEARCPG has also been modified to execute on Linux clusters. Other improvements have been made to the CEARCPG code, including parallel and differential operator (DO) features for the application of the Monte Carlo Library Least Squares approach.

With all the improvements to Monte Carlo simulation codes, the coincidence PGNAA could be optimized. For lab size samples, the paraffin moderator has been optimized for thickness. Through rearranging detectors or using different shape detector, the ratio of improvement can be up to 66.5 and 223.7 for single and coincidence response respectively compared to the original coincidence arrangement. There is also higher efficiency for higher energy gamma-rays for certain cases. For large size sample, the self-moderation of the bulk coal is sufficient. A new detector choice, a plastic scintillation detector, has been investigated to utilize its large volume and excellent time resolution. The simulated 2D coincidence spectra show the feasibility of using the plastic detector as a trigger to another detector that has better energy resolution. The ratio of improvement can be up to 2.5 and 6.2 for single and coincidence responses respectively compared with placing two 6”x6” cylindrical detectors in the opposite of neutron source.

Among all the interferences, the fission gamma-ray source remains the major one while the interference from the analyzer structural material also contributes significantly. Q-value projection on the 2D spectra could further suppress the interference. The MCLLS analysis on the Q-value projected spectra shows better accuracy than using the total coincidence spectra.

With proper shielding, the dose rate around the analyzer is pretty low.

The funding of this work has been provided by the Center for Engineering Application of Radioisotopes (CEAR) at North Carolina State University (NCSU).

Monte Carlo Optimization of Coincidence Prompt Gamma-Ray Neutron Activation Analysis

by
Jiaxin Wang

A dissertation submitted to the Graduate Faculty of
North Carolina State University
in partial fulfillment of the
requirements for the Degree of
Doctor of Philosophy

Nuclear Engineering

Raleigh, North Carolina

2011

APPROVED BY:

Dr. Robin P. Gardner, Chair	Dr. Dmitriy Y. Anistratov
Dr. Richard M. Lindstrom	Dr. Peter Bloomfield

DEDICATION

To my respected parents: Wang, Shutai and Lu, Lanxiu.

To my lovely wife: Zhu, Yan.

BIOGRAPHY

Jiaxin Wang was born in China on August 18, 1983. He is the only son of Mr. Shutai Wang and Mrs. Lanxiu Lu. He spent his youth in Linyi, Shandong.

Jiaxin received his Bachelor’s Degree in Engineering Physics in 2005 from Tsinghua University, China. After that, He worked as a research assistant for a year at Key Laboratory of Atomic, Molecular & Nano Science, China.

In 2006, he entered the PhD program in the Nuclear Engineering Department at North Carolina State University and worked as a research assistant on Monte Carlo simulation and nuclear instrumentation for radiation measurement applications under Prof. Gardner’s advisory. Along his study towards PhD degree in Nuclear Engineering, Jiaxin received his Master’s Degree in Statistics from NC State University in 2009.

Jiaxin married with Yan Zhu in 2006.

ACKNOWLEDGEMENTS

The author would like to express his deep gratitude and appreciation Dr. Robin P. Gardner for his invaluable guidance and continuous encouragement and moral support throughout the graduate study.

The author would also like to extend his warmest thanks to other members of the committee: Dr. Richard M. Lindstrom, Dr. Dmitriy Y. Anistratov, and Dr. Peter Bloomfield for helping achieve such an important milestone in his life. Appreciation is also extended to other professors and staff in the Department of Nuclear Engineering: Dr. Mohamed A. Bourham, Dr. Steven C. Shannon, Mr. Gerry Wicks .etc.

To all of the current and former students at CEAR, the author would like to express his warmest thanks, with special thanks to Dr. Xiaogang Han and Dr. Libai Xu.

The author is also grateful for the financial support of the Associates Program for Nuclear Techniques in Oil Well Logging presently supported by Baker Hughes, Weatherford, EXXON Mobil, Halliburton, Pathfinder and Los Alamos National Laboratory.

Finally the author would like to express his heartfelt thanks to his parents and wife, for their love, giving, encouragement, understanding, and patience.

TABLE OF CONTENTS

LIST OF FIGURES

LIST OF TABLES

1 INTRODUCTION

1.1 Overview

Neutron activation analysis (NAA) is an analytical technique used for both qualitative and quantitative analysis of major, minor, and trace elements in samples from almost every conceivable field of scientific or technical interest. According to the time of measurements NAA can be separated into two categories: Prompt Gamma Neutron Activation Analysis (PGNAA), where measurements are performed during the irradiation time; and Delayed Gamma Neutron Activation Analysis (DGNAA) or Instrumental Neutron Activation Analysis (INAA), where the measurements are performed after the irradiation.

Prompt gamma-rays are emitted during neutron interactions including neutron capture interaction and neutron inelastic scattering interaction, with the elements in the sample of interest. The basic principle behind the neutron radioactive capture process which dominates neutron interaction in low energy region is that the excited compound nucleus which is formed by capturing the incident neutron then degrades quickly (less than 10-14 seconds) to the ground level by emitting gamma-rays which are unique for each isotope. These prompt gamma-rays are in energies that are characteristic of the target nucleus, and can be detected to identify elements or isotopes when gamma-ray spectrometry is used. This approach is called prompt gamma-ray neutron activation analysis (PGNAA). In many cases, there also yield radioactive nuclei, which also de-excites by emitting one or more characteristic delayed gamma-rays, but at a much slower rate according to the unique half-life of each radioactive nucleus. The technique of analyzing elements by measuring these delayed gamma rays is called delayed gamma-ray neutron activation analysis (DGNAA) or instrumental neutron activation analysis (INAA). All of these instances are illustrated in figure 1-1.

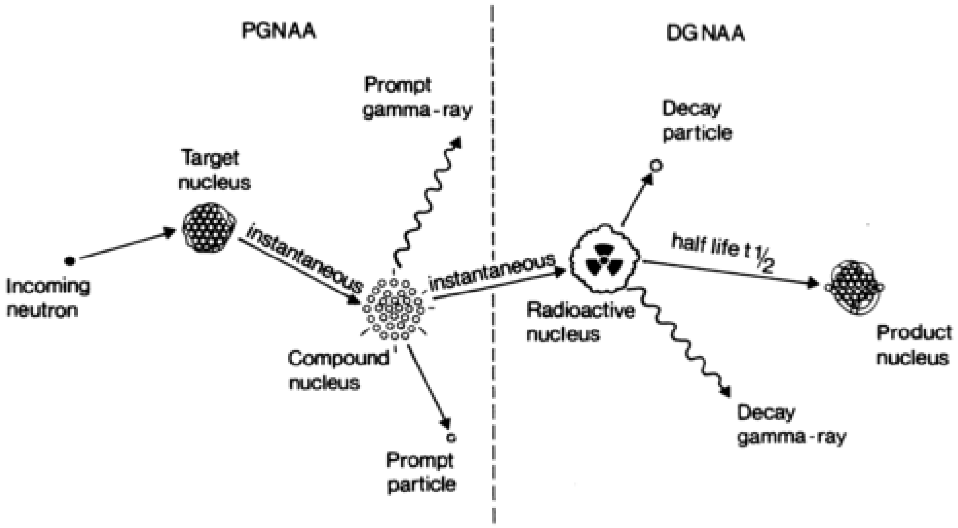

Figure 1-1 The physical process of Neutron Activation Analysis

Many reviews and papers have been published on NAA and its applications (Greenwood, 1979; Anderson, 1982; Lindstrom, 1994, 1997; Paul, 2000), and two extensive bibliographies have also been compiled (Gladney, 1979; Glascock, 1984). Comparing to the more commonly used DGNAA/INAA, PGNAA is a nondestructive, simultaneous method and theoretically applicable to all elements. However, PGNAA has to face the relatively complicated gamma spectra, the interferences from the neutron source, the structure material, and interferences from the natural background, pulse pile-up and summing effect (Metwally, 2004). The gamma-gamma coincidence technique is a possible way to overcome these drawbacks.

1.2 Coincidence Technique

Kim, Speecke and Hoste(1965) and Kim and Hoste(1965) have some of the earliest gamma-gamma coincidence measurements. They were interested in determining the concentration of copper, silver and antimony in bismuth. Their results were based on scalar counts and yielded results with considerable errors.

In elemental analysis, the gamma-gamma coincidence technique has already been demonstrated by Ehmann and Vance (1991), Meyer (1987), Meyer et al. (1993), Jakubek et al.(1998), and Koeberl and Huber (2000), especially in determining Ir and Se in geological samples at ppm level. Their main goal was to improve the sensitivity of the method by suppressing the continuous background and reducing spectral interference.

Another important area of the gamma-gamma coincidence measurements is the determination of the excited states of elements (Demanins and Raicich, 1992, 1994, Jungclaus et al., 1994, Moon et al, 2001, Medeiros et al, 2001 and Ember et al., 2002). This technique has also been tried to apply in cascade spectrometer for resonant reactions (Pallone and Demaree, 2009) at typical ion beam analysis facilities by selecting only events that match the desired combination of photon emissions and rejecting other events to reduce the background and improve the signal to noise ratio (SNR)

Instead of requiring a coincidence relation with a selected full-energy peak, some useful attempts were done by Ember (2002 and 2004), Gardner and Walid (2000 and 2004). In Ember's work (2002), they proposed to define a coincidence relation not with a single peak, but with a selected part of the spectrum containing several peaks and a part of their Compton continuum to increase the coincidence efficiency. All the coincidence events were included in Gardner and Walid's work (2000 and 2004) and Q-value summing and diagonal window projection offline analysis were proposed and validated to better utilize the coincidence information.

In Gardner's (2000) work, a feasibility study was done by using the coincidence counting approach. Their main concern was to apply this approach to PGNAA application. They used NIM modules, NaI detectors and neutron source from the reactor and Cf-252. The results showed that the coincidence measurement can efficiently reduce the background and increase the signal-to-noise (S/N) ratio. In Metwally's (2004) work, CAMAC modules based on SPARROW multi-parameter data acquisition system was used. Recently, the new advanced digital signal processing (Tomlin et al., 2008) has been used to replace conventional analog electronics in gamma-gamma coincidence measurement at the National Institute of Standards and Technology (NIST), using two HPGe gamma-ray detectors in NAA.

The coincidence technology has also been used in other area like Beta-gamma coincidence (Luca et al., 2000 and Ashrafi et al., 2008) to detector low level gamma, and coincidence between cosmic-ray muons (Jokovic et al., 2009). Instead of using NaI, BGO or HPGE detectors, one detector studied there was plastic scintillation. It will also be interesting to test it in gamma-gamma coincidence.

The main disadvantage is that coincidence PGNAA is very time consuming due to the low coincidence counting rate. Thus, the coincidence PGNAA need to be optimized to improve the gamma-ray detector counting rate, both single and coincidence. Thanks to the development of modern computer and Monte Carlo codes, most of the optimization work could be done with Monte Carlo simulation.

1.3 Overview of Monte Carlo Work

Monte Carlo simulation for the PGNAA device has been conducted for several years. Before 1991, the roles that Monte Carlo simulation played in the PGNAA systems were mostly focused on predicting the spectral responses that could be used to compare with experimental spectrum or optimize the PGNAA analyzer systems in their design stage. A variety of specific Monte Carlo simulation codes were reported in the past. They are: McPNL, developed in CEAR which modeled the spectral response of dual-spaced gamma-gamma litho-density logging tools (Mickael et al., 1988), McDN, developed in CEAR (Mickael et al., 1988), and MOCA (Pinault et al., 1989) etc. However, the concept of MCLL.s algorithm (Shyu et al., 1991, 1993) greatly extended the application of Monte Carlo simulation, since it made possible to use simulated elemental library spectra to apply the Least-Square fitting to analyze the unknown sample spectra. The application of MCLLS algorithm has been reported in a paper (Shyu et al., 1993), where elemental library spectra were generated by a specific Monte Carlo code, CEARPGA I.

CEARPGA I is the first specific Monte Carlo code publicly reported to implement MCLLS algorithm for PGNAA analyzer. It was developed on the basis of many previous research works on modeling PGNAA devices, which mostly were done at CEAR of North Carolina State University. It inherits many features from its previous versions. The Clark first developed a Monte Carlo code to model the system of borehole geometry (Clark et al., 1982), which incorporated the correlated sampling approach that allow the calculation of the reference sample and comparison samples at the same time. It used continuous energy treatment of neutron transport by using piecewise fitted neutron cross sections of ENDF/B-V. Yuan modeled the system of transmission geometry (Yuan et al., 1987), where some features extracted from those used in the previous version. These new features included implicit capture scheme for gamma-ray generation and Russian roulette for particle termination. A further improvement (Jin et al., 1987) was done for modeling the complete pulse-height spectral response of PGNAA of bulk media and borehole configuration, where Ge (Li) detector response function was first used to generate the pulse-height spectrum when all the simulation histories were finished. To implement the Monte Carlo library least squares algorithm, Shyu modified Jin's Monte Carlo code to extend the capability of generating elemental library spectra (Shyu et al, 1993). A further improvement were done later by Guo (1997) who added the functions of generating the gamma-ray library spectra from neutron inelastic scattering reaction and radioisotope decay gamma-ray library, and included the NaI detector response functions obtained by another Monte Carlo simulation code developed by Peplow et al. (1994).

The CEARPGA I was developed with much effort on accuracy and efficiency. The major variance reduction techniques used include: russian roulette, truncated exponential probability density function, direction biasing, discrete importance function, stratified sampling approach, expected value splitting approach, correlated sampling and detector response function. To solve the big weight problem caused by expected value splitting approach in code CEARPGA I, Zhang developed the next generation code CEARPGA II (Zhang, 2003) by using analogy interpolation method. However, another error will be introduced when applying analog linear interpolation method to generate the true elemental spectra, especially at low energy region.

Both code CEARPGA I and CEARPGA II are originally designed to simulate the single library elemental spectra. CEARCPG (Han, 2005) was developed at CEAR for this purpose of simulating the coincidence spectra. CEARCPG is the first specific Monte Carlo code for elemental analysis by using coincidence technique. It can generate the single library spectra and the coincidence spectra of interested elements at the same time. The single library spectra and coincidence spectra will be served as elemental library spectra for the next step, Library Least – Squares fitting. The most contributions of Han’s work is a new algorithm to sample the neutron-produced coincidence gamma-rays that completely follow the principles of nuclear physics.

To the best of our knowledge, the other code that is capable of doing coincidence prompt gamma-ray simulation is GEANT4 (Agostinelli et al., 2003). GEANT4 is a popular general purpose simulation environment, and was developed by CERN (European Organization for Nuclear Research). Its object-oriented design and implementation in C++ means that the code is flexible and can be enhanced easily through class inheritance, and it is well supported by geometry visualization and data analysis utilities. The most attractive feature of GEANT4 is the abundant set of physics processes. However, GEANT4 need to be modified to simulate neutron induced prompt gamma-rays correctly (Xu, 2006) because GEANT4 uses a certain theoretical model called the Photon Evaporation Model to simulate the neutron capture reaction. The Q-value of the neutron capture reaction is calculated based on the incident neutron energy instead of fixed Q-values as in our common knowledge. This difference causes the subsequent prompt gamma ray information to be totally wrong. Also, GEANT4 is almost a pure analog method without many variance reduction techniques. Its simulation speed is not good. Thus, GEANT4 is not used in this work.

One thing should be noted is detector response function (DRF) that has been used since CEARPGA I. Instead of experiments, the DRF that ever used were all generated from simulation. The DRF used in CEARPGA I was generated by code Monte (Peplow et al., 1994) for certain cylindrical NaI detector only. Later, the NaI nonlinearity and Compton continuum adjustments were added through code G03 (Gardner and Sood, 2000) and the new DRF were used in CEARPGA II and CEARCPG. In order to optimize the coincidence PGNAA with new scintillation detectors, different shapes and sizes, a new DRF generation code need to be developed.

1.4 Review of PGNAA Analysis Methods

Peak analysis and Library Least Squares (LLS) are two popular methods to do quantitative analysis of the measured PGNAA gamma spectrum. It was pointed out in early research that the library least-squares method is about 2.5 times better than the single peak analysis method (Gardner et al., 1997).

For the single peak analysis, peak intensities are not only related to the elemental weight fraction but also related to the sample matrix and the correction methods used. In large sample, the correction is more difficult, because neutron and gamma flux, in both energy and space, are changed in a highly non-trivial, non-separable, and composition dependent way (Holloway and Akkurt, 2003). The MCLLS method can fix the matrix problem automatically because when generate the elemental library spectra, the Monte Carlo code should consider the shielding (attenuation) prompt gamma rays and the interference from the elements automatically.

The MCLLS method has many advantages which make it a desirable method for various applications including: (1) it is the most fundamental approach; (2) it is capable of giving the most accurate results possible since the entire spectrum can be used; (3) it automatically provides an estimate of the standard deviation of each calculated elemental amount in the presence of all other components; and (4) peak interferences are automatically accounted for. One difficulty is that elemental libraries must be available for all elements present in the sample of interest. In MCLLS approach these libraries are provided by Monte Carlo simulation

(CEARCPG) rather than by experiment, so this problem has been substantially tackled. Another difficulty is that MCLLS usually requires several iterative Monte Carlo runs to achieve the best results, which is very time-consuming. Thus, the differential operator approach needs to be implemented into CEARCPG, which only requires one Monte Carlo run.

2 DETECTOR RESPONSE FUNCTION

2.1 Overview

Detector response function (DRF) is a very important inherent property of detector. As implied by the name, it is the detector response to a series of monoenergetic source of that radiation. A Detector response function, denoted by $D(E',E)$, where E is incident gamma or X-ray energy and $E'$is pulse height gamma or X-ray energy, gives the pulse height spectral energy distribution for any specific gamma-ray or X-ray incident energy. Figure 2-2 shows an example of DRF. As a probability density function (pdf), DRF's integral over all pulse height energy is unity.

Accurate detector response functions have become increasingly useful and needed for many applications, including the construction of spectral libraries for use in the Monte Carlo library least squares (MCLLS) analysis method for inverse elemental analysis of prompt gamma-ray neutron activation analysis (PGNAA) and energy-dispersive X-ray fluorescence (EDXRF) analyzers.

There are several advantages of using detector response functions in Monte Carlo simulation, including:

(1) DRFs could be pre-calculated or pre-measured and take care of the inside tracking of detector. Thus, each gamma-ray history is tracked only outside the

detector, saving as much as 50% of the total tracking time for each gamma-ray history in the Monte Carlo simulation;

(2) DRFs can be made considerably more accurate by empirical or semi-empirical methods than directly tracking inside the detector, which make the use of DRFs yield better accuracy in spectral simulations and is critical in following least square analysis;

(3) DRFs could 'naturally' apply detector resolution to simulated flux spectra to smooth it. Most Monte Carlo codes including the most popular general purpose MCNP5 try to apply it directly to each history. Using of DRF could further reduce the simulated history number by 1 or 2 magnitudes to reach the same statistical requirements.

In PGNAA application, the specified purpose Monte Carlo code is used to simulate particles outside the detector and first tracking the prompt gamma rays to the point that they are incident on the detector. These incident gamma-ray spectra or called flux spectra for each element are saved and DRFs are subsequently used to convolute these spectra into detected pulsed-height spectra. Then further spectra analysis could be applied with the simulated pulsed-height spectra and the experimental spectra. The flow chart of the whole process is plotted in figure 2-1. Therefore, accurate detector response functions are very critical to PGNAA application.

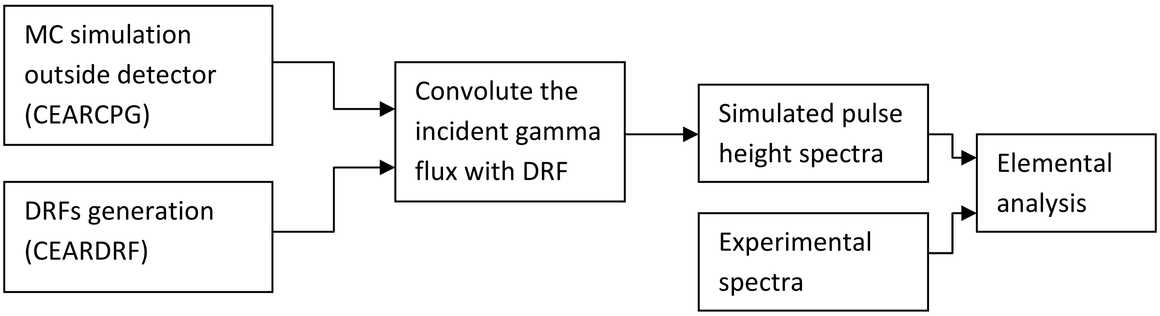

Figure 2-1 General flow chart of PGNAA application with DRFs

2.2 Detector Response Function Generation

Because the same detector has been repeatedly used under different situations, the particle-transport inside the detector (DRF) could be pre-generated to improve future simulation speed and accuracy. Generation of detector response function usually has three ways (Gardner et al., 1986).

(1). Experimental approach. Heath (Heath 1964, 1974) is the pioneer in this area. His gamma-ray spectrum catalogs on NaI, Ge(Li) and Si(Li) detectors are still reliable source to benchmark simulation work. However, the disadvantage of this approach is also obvious. First of all, it is hard to have access to and maintain many monoenergetic sources, since the half lives of some are very short. Secondly, there are always features that present in experimental spectra that are not part of DRF. For example, gamma-ray that backscattered to detector from surrounding materials and 0.511 MeV annihilation photons are not legit parts of detector response function. In the upper spectra of figure 2-2 (Heath, 1964), all the spectra have backscatter peaks in the lower energy side. Finally, the experiments are very time consuming and issues like gain-shift need to be carefully treated for all the DRF.

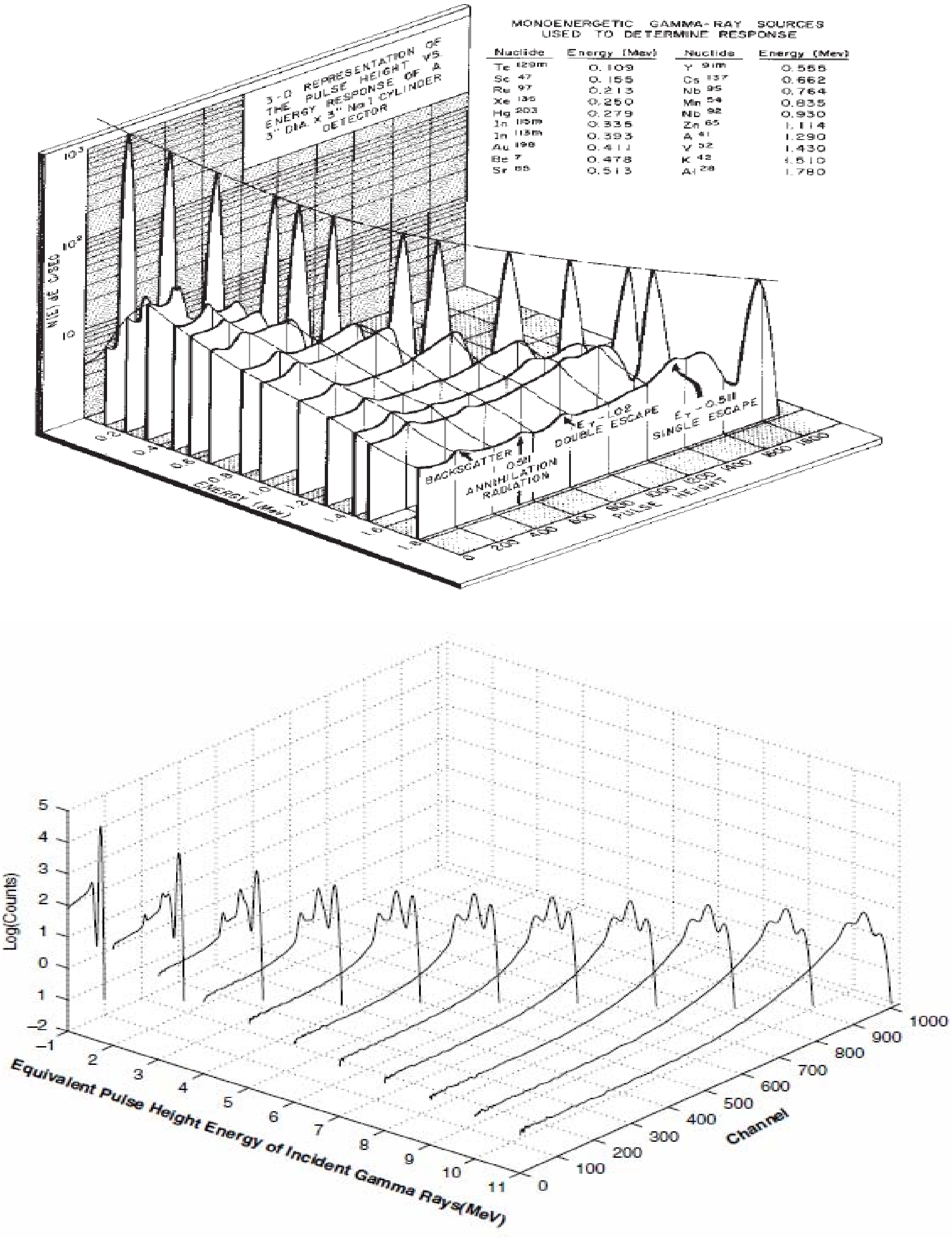

MONOENERGETIC GAMMA-RAY SOURCES
USED TO DETERMINE RESPONSE

Nuclide	Energy (Mev)	Nuclide	Energy (Mev)
Te ^{129m}	0.109	Y ^{91m}	0.555
Sc ^{47}	0.155	Cs ^{137}	0.662
Ru ^{97}	0.213	Nb ^{95}	0.764
Xe ^{135}	0.250	Mn ^{54}	0.835
Hg ^{203}	0.279	Nb ^{92}	0.930
In ^{115m}	0.335	Zn ^{65}	1.114
In ^{113m}	0.393	A ^{41}	1.290
Au ^{198}	0.411	V ^{52}	1.430
Be ^{7}	0.478	K ^{42}	1.510
Sr ^{85}	0.513	Al ^{28}	1.780

Figure 2-2 Three-dimensional model of DRF
3"x3" NaI detector to monoenergetic gamma radiation, the upper one is experimental results and the below one is from simulation.

(2). Monte Carlo approach. Detector response is simulated strictly following the basic principles with Monte Carlo methods, utilizing the normal exact geometrical description of the detector and the exact physics of photon and electron transport. In principle, one could use Monte Carlo simulation entirely to produce DRFs if all of the pertinent detector characteristics were known exactly. Most general purpose Monte Carlo simulation codes, like MCNP5 (2008), EGS (2000) and ITS (2005), could be considered be in this category. And the simulation results are usually considered to be accurate enough. However, the approach is very time consuming as there are lots of interactions/scattering following full physics, while the eventual fates of lot of tracking results are to deposit all energy in the detector. Also, some features of detector are nearly impossible to determine, like the imperfections within the crystal. Hence, there are several parts of DRFs that cannot be treated correctly by this approach, including the detector resolution or called the standard deviation of the Gaussian distribution of the pulse height distribution, the flat continuum from zero to full energy peak and low energy side of the full energy peak for Ge(Li) and Si(Li) detectors.

(3). Hybrid approach. It is naturally to combine the Monte Carlo approach with some empirical or semi-empirical parameters that acquired from experiments. In this way, some unnecessary tracking of particles could be avoid to accelerate the simulation and empirical or semi-empirical parameters could be used to correct some features of detector. It has been used by many previous works, like semi-empirical approach for DRFs of the semi conductor Ge (Jin et al., 1986; and Lee et al., 1987) and Si(Li) detectors (Yacout et al., 1986; Gardner et al., 1986; and He et al., 1990) and NaI detector (Peplow et al., 1994; and Gardner et al., 2004). At CEAR, we also maintain a local version of MCNP5 (Wang et al., 2008), which has been implemented some empirical parameters to improve accuracy and been simplified in electron transport to save time. This is also the approach used in this work of CEARDRFs to speed up the simulation and improve accuracy, although this method does not give much insight into the physical processes that take place inside the detector.

The Center for Engineering Application of Radioisotopes (CEAR) has over 20 years' history of research on detector response functions. A variety of specific DRF generation models and codes were developed at CEAR in the past for both semi-conductor and scintillation detectors. Most of these codes can generate DRFs by separate components and then sum them up. Some of the first work in generating the entire spectra was done by Berger and Seltzer (1972). Code MONTE (Peplow et al., 1994) is the first one that demonstrated for generating entire spectra DRF for gamma rays incident on NaI detectors with improved physics. The approach was demonstrated for gamma-rays with energy from 0.5 to 10.5 MeV incidents on 3”x3” and 6”x6” cylindrical detectors, while source position is fixed at 10cm away from the one surface. To properly treat the non-linearity effect of NaI crystal and the lower estimation of flat continuum, code G03 and G04 (Gardner et al., 2004) were developed.

To optimize the PGNAA application, the interest naturally expanded to generate DRFs for more scintillation detectors, more detector shapes and sizes, which gave birth to the simple but accurate detector generation code CEARDRFs developed by the author. The code CEARDRFs could generate detector response functions for gamma-rays incident on scintillation detectors (NaI, BGO, .etc) with various shapes (cylinder or rectangle) and different sizes. Theoretically, it can be applied to all kinds of scintillation detectors with proper experimental data.

2.3 Physics in CEARDRFS

The Monte Carlo model used in CEARDRFs to generate the entire pulse height spectra including two parts: photon treatment and electron treatment. Both of them need the geometry part to handle the transport.

2.3.1 Geometry Treatments

Whenever the direction is assumed to be isotropic, the direction is sampled by the introduction of two independent random variables, the polar angle θ (or $\mu=\cos\theta$) and the azimuthal angle ϕ . It is described as follows.

$$\mu = 2\xi_1 - 1 \qquad \varphi = 2\pi\xi_2 \tag{2-1}$$

where ξ_1, ξ_2 are two random numbers between 0 and 1

The direction cosines (Ω_1 ,Ω_2 , Ω_3) of the direction in the Cartesian system can thus be obtained by,

$$\Omega_1 = \sqrt{1-\mu^2}\cos\varphi \qquad \Omega2 = \sqrt{1-\mu^2}\sin\varphi \qquad \Omega3 = \mu \tag{2-2}$$

Force method is used for the initial gamma to force the gamma-ray hit the detector.

When sampling the path length, the normal exponential probability density function as shown below will be used to determine the flight distanced d:

$$p(x) = \Sigma_t \exp(-\Sigma_t x), \text{ For } 0 \le x \le \infty \qquad (2\text{-}3)$$

and the distance d is determined by

$$d = -\frac{1}{\Sigma_t} \ln \xi \qquad (2\text{-}4)$$

where Σ_t is the macroscopic total cross section of the detector.

This distance d is to be compared with the distance to the detector boundary D to determine whether it is necessary to continue the sampling process for the flight distance. If d ≤ D, the next interaction position will be in the detector or on its boundary, this indicates that the sampling process of flight distance to the next interaction is completed, and the next interaction position is calculated by

$$\begin{aligned} x &= x_0 + d\Omega_1 \\ y &= y_0 + d\Omega_2 \\ z &= z_0 + d\Omega_3 \end{aligned} \qquad (2\text{-}5)$$

where (x_0, y_0, z_0) is the current position. If d ≥ D, it means that the gamma will leave the detector and the gamma history will be terminated.

2.3.2 Photon Treatments

Simple photon treatment is used in CEARDRFs. This method is very similar to the simple mode used in MNCP. The coherent scattering is not considered.

CEARDRFs only considers the three basic gamma-ray interactions (Knoll, 2000) with matter photoelectron effect (pe), pair production (pp), Compton scattering (cs).

Total micro-cross section σ_t is regarded as the sum of the three components,

$$\sigma_t = \sigma_{pe} + \sigma_{pp} + \sigma_{cs} \tag{2-6}$$

Photoelectron Effect

In the photoelectron absorption process, a photon undergoes an Interaction with an absorber atom in which the photon completely disappears. In its place, an energetic photoelectron is ejected by the atom from one of its bound shells. The photoelectron appears with an energy given by,

$$E_{e-} = E - E_b \tag{2-7}$$

where E is the incident gamma energy and E_b represents the binding energy of photoelectron in its original shell.

The photoelectrons in this interaction are assumed to be emitted in an isotropic distribution, and E_b is assumed to be neglectable comparing to incident gamma energy. The CEARDRFs continues track the ejected electron with simple treatments that will be described below.

Compton Scattering

The interaction process of Compton scattering takes place between the incident photon and electron in the absorbing material. It is the predominant interaction mechanism for low-energy gamma rays. The scattered photon energy can be calculated by the following equation,

$$E' = \frac{E}{1 + \frac{E}{m_0 c^2 (1 - \cos\theta)}} \tag{2-8}$$

where $m_0 c^2$ is the rest-mass energy of the electron (0.511MeV) and θ is angle between the direction of scattered photon with respect to its original direction.

The angular distribution of scattered gamma-ray is predicted by the Klein-Nishina formula for the differential cross section $d\sigma / d\Omega$

$$\frac{d\sigma}{d\Omega} = Zr_0^2 \left(\frac{1}{1 + \alpha(1 - \cos\theta)} \right)^2 \left(\frac{1 + \cos^2\theta}{2} \right) \left(1 + \frac{\alpha^2 (1 - \cos\theta)^2}{(1 + \cos^2\theta)[1 + \alpha(1 - \cos\theta)]} \right) \tag{2-9}$$

where $\alpha = h\nu / m_0 c^2$ and r_0 is the classical electron radius. Kahn rejection method (Kahn, 1954) is used in CEARDRFs to sample the angle θ. The scattered gamma-ray continues to be tracked until meeting the terminating conditions.

The photon transfers a portion of its energy to the electron named recoil electron. The recoil electron energy E_{e-} and the direction θ_e of recoil electron with respect to the original photon direction can be calculated by the following equation,

$$E_{e-} = E - E' \tag{2-10}$$

$$\cos\theta_e = \frac{E / E' - \cos\theta}{\sqrt{(E/E')^2 - 2(E/E') + 1}} \tag{2-11}$$

The CEARDRFs continues track the recoil electron with simple treatments.

Pair Production

If the gamma rays energy exceeds twice the rest-mass energy of an electron (1.02 MeV), the process of pair production is energetically possible. In the interaction (which must take place in the coulomb field of a nucleus), the photon disappears and is replaced by an electron-positron pair. All the excess energy carried in by the photon above 1.02 MeV required to create the pair goes into kinetic energy share by the positron and electron. The available energy for the electron and positron is evenly split between them,

$$E_{pkin} = E_{ekin} = \frac{1}{2}(E - 2m_0c^2) \tag{2-12}$$

The polar angle, θ_p, of the emission for the electron and positron is assumed to be selected randomly between 0 and θ_m (J.K. Shultis, 2000),

$$\cos\theta_m = m_0c^2 / E \tag{2-13}$$

Then the azimuthal angle θ_z is chosen isotropically and the positron azimuthal angle is taken as the opposite ($\theta_z \pm 180^\circ$). The electron and position will continue be tracked in CEARDRFs with the simple electron treatments.

If the positron will eventually annihilate (not leaving the detector) after slowing down in the detector, two annihilation photons are normally produced as secondary products of the interaction. Each of them has an energy equivalent to the rest mass of the electron. The direction of the first photon is chosen isotropically and the second is taken to be in exactly the opposite direction. The subsequent fact of this annihilation radiation has an important effect on the response of gamma-ray detectors. The two annihilation photons continue to be tracked separately until they meet the termination conditions.

Sample The Interaction Type

Three types of gamma ray interactions pre-dominate the energy range from 10 keV to 12 MeV as discussed above. Of these three interactions, the photoelectric effect predominates in the lower energy range, the pair production is important only for gamma rays of higher energies (>1.02 MeV) and Compton scattering predominates in intermediate energies.

The probability function used to sample the interaction type can be described as follows,

$$p_j = \frac{\Sigma_j}{\Sigma_t}, \quad j = 1(pe), 2(cs), 3(pp) \tag{2-14}$$

where Σ_t is the total macroscopic cross section in the material, and Σ_{pe} is the macroscopic cross section of photoelectric effect, and Σ_{pp} is the macroscopic cross section of pair production and Σ_{cs} is the macroscopic cross section of Compton scattering. The interaction j is sampled if

$$\sum_{k=1}^{j-1} p_k \le \xi < \sum_{k=1}^{j} p_k \tag{2-15}$$

where ξ is the random number between 0 and 1.

Photon Cross Section

CEARDRFs inherits a NJOY (MacFarlane, 1994) pre-processing nuclear data from other CEAR codes. The photon cross section are extracted from EPDL library and are processed into three separate tables, which are total cross section table (Gtotal.xs), Compton scattering cross section table (Gcmptn.xs), and pair production table (Gpp.xs). These tables cover all the elements from Z=1 to 100 and the energy range now from 10 KeV to 20 MeV, which make the code expandable to all kinds of scintillation detectors theoretically. The old G03 code used cross sections that take from Heath data (Heath, 1957), which is only for NaI detector.

Terminating Gamma-rays

There are three ways to terminate gamma particle history. (1) Gamma particle escape the system; (2) Gamma particle has photoelectric interaction and (3) Gamma particle energy is lower than the energy cut.

2.3.3 Electron Treatments

An electron is slowed down as a result of both coulombic interactions with (atomic) electrons and radiation loss (Bremsstrahlung). Range, the continuous slowing-down approximation, combining with Bremsstrahlung, is usually a good approximation for electron transport.

Electron Range

The first step of the treatment for electron transport is calculating the extrapolated range of the electron, R_e, through the medium without any major interactions. The equation (Katz and Penfold, 1952) used to calculate range R_e is,

$$R_e = \frac{aE^{(b-c\ln E)}}{\rho} \tag{2-16}$$

where R is in cm, E is in MeV, ρ is in g/cm^3, and a, b, c are empirical parameters.

There a, b and c values (Table 2-2) are fitted with Pages' data (Figure 2-3) (Pages et al., 1972) for NaI detector and BGO detector. For BGO ($Bi_4Ge_3O_{12}$), there is no compound data available. The weighted summation of Bismuth, Germanium and Oxygen was used. Then density of NaI and BGO is 3.667 g/cm^3 and 7.13 g/cm^3 respectively.

Distance Traveled without Interaction

According to the electron range, the distance traveled without interaction by an electron with certain energy needs to be sampled. An electron continues in a straight line losing energy by ionization until a major interaction occurs and takes it out of the original path direction. Then, the probability distribution function for the distance traveled by the electron before a major interaction occurs would be uniform between zero and the calculated range R_e. A modified pdf (Peplow et al., 1994) was created to treat the slightly greater distance. The approximation to the probability distribution, p(d) per cm, to travel a distance d cm was made by using,

$$p(d) = 2(1+3d / R_e) / (5R_e) \tag{2-17}$$

Then the same geometry treatments as photon are applied to check whether the electron leave the detector. If not, the electron will be updated to a new position.

Table 2-1 Range parameters for NaI and BGO detector calculated from Pages' data

	a	b	c
NaI	0.69361	1.15080	0.083893
BGO(E<=0.1MeV)	0.68223	1.24847	0.068837
BGO(0.1MeV<E<=1MeV)	0.69894	1.14744	0.119043
BGO(E>1MeV)	0.70506	1.10863	0.080150

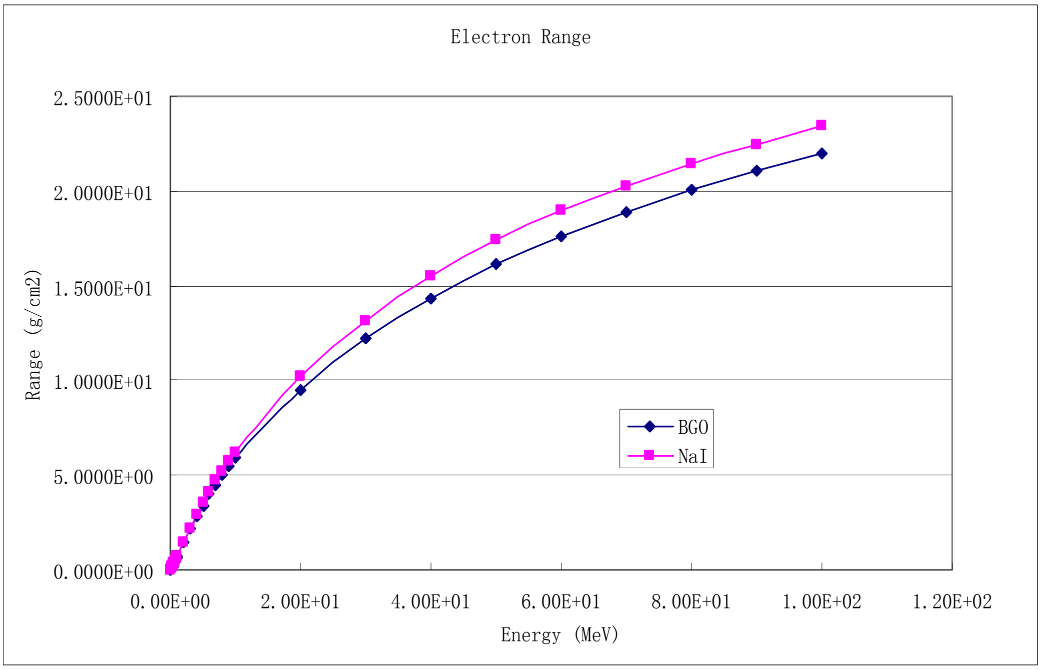

Figure 2-3 Range energy relationships of NaI & BGO detectors (Pages et al., 1972)

The electron then loses energy by ionization as it moves through this distance. Using this range-energy relationship, the new energy of the electron, *E'*, after moving through distance *d* and losing energy due to ionization collisions is calculated to be:

$$E' = \exp[\frac{b}{2c} - \sqrt{(\frac{b}{2c})^2 - \frac{1}{c}\ln(\frac{\rho(R_e - d)}{a})}] \tag{2-18}$$

The difference of the original energy of the electron and its new energy is deposited in the detector, as long as the path does not leave the detector.

Bremsstrahlung Radiation

After traveling to major interaction at a new position inside the detector, the direction of the electron will change. The radiation energy loss of the electron by production of bremsstrahlung radiation contributes to the change. Radiative energy loss is dominant for electrons at higher energy while collisional energy loss is dominant for lower energy and is characterized by the stopping power. Instead of modeling the radiative production of bremsstrahlung by use of the stopping power, empirical value τ was used as an approximation, which means for an electron kinetic energy, *T*, the ratio, τ, of the major interactions that are treated as producing bremsstrahlung radiation.

$$\tau = \begin{cases} eff \cdot T & T \leq 10/eff \text{ MeV} \\ 1 & T > 10/eff \text{ MeV} \end{cases} \tag{2-19}$$

The *eff* values in table 2-2 were found empirically to make the spectra shapes similar to the experimental spectra.

Table 2-2 Empirical *eff* parameter for NaI and BGO detector

	3”x3” NaI *	**6”x6” NaI ***	**2”x2” NaI**	**2”x2” BGO**	**2”x4”x16” NaI**
eff	0.3	0.2	0.5	0.25	0.25

* Berger et al., 1972, and Halbleib et al., 1992

It is easy to understand that for the same scintillator, the larger the size, the less possible that bremsstrahlung photon will eventually escape. For BGO detector, because it is denser than NaI, there are less bremsstrahlung photons escaping from detector than NaI detector of the same size. For the rectangular NaI detector, the large face is usually used in detection, which raises the possibility that bremsstrahlung photons escape from detector.

The energy of bremsstrahlung photons are picked from a distribution given by Hansen and Fultz (1960). An energy scaled version of this curve in figure 2-4 is used for other energies. The electron angle is scattered at 90 degree and the photon is emitted in the original direction of the electron. The electron continues with an energy reduced by the energy of bremsstrahlung photon. Both electron and photon are tracked until meeting the termination conditions.

Terminating Electrons

There are two ways to terminate electron history. (1) Electron escapes the system; (2) Electron deposits all energy inside the detector or below the energy cut.

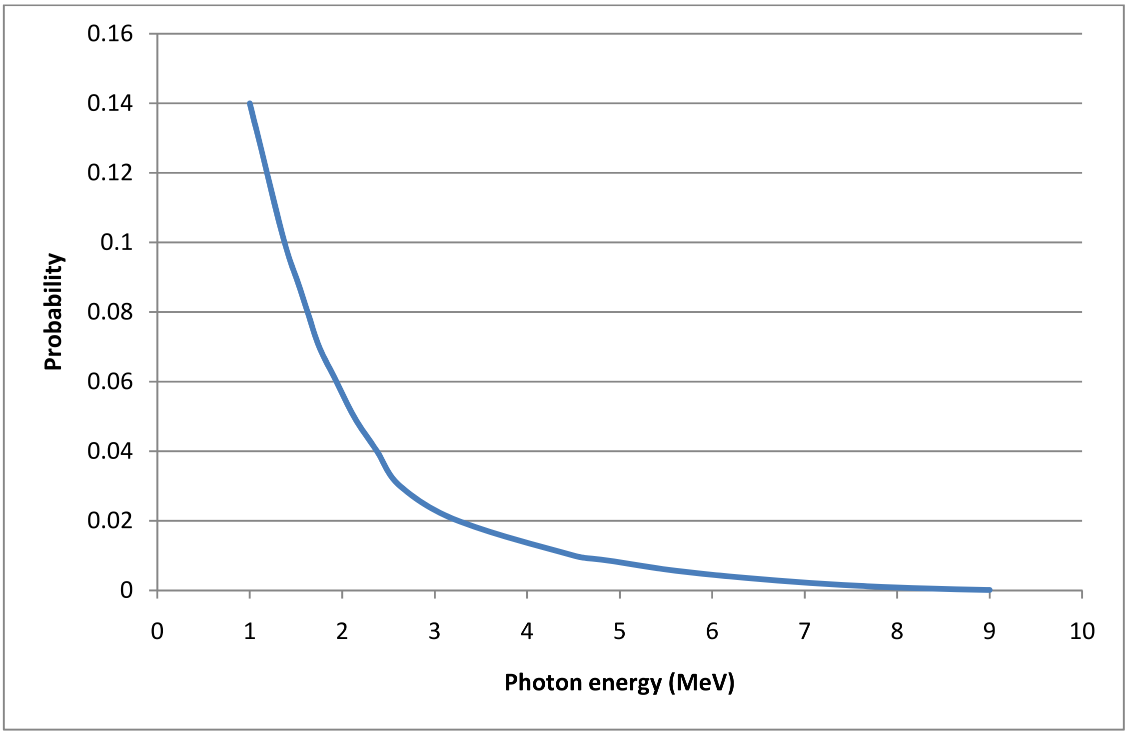

Figure 2-4 Bremsstrahlung photon energy distribution of 10 MeV electron in thick target

2.4 Adjustments in CEARDRFs

Following the above physics, it is still not good enough to generate accurate detector response function. Certain adjustments need to be done in CEARDRFs including scintillator's nonlinearity and flat continuum adjustment. Also, to account for detector resolution, proper Gaussian broadening parameters need to be extracted from experiments.

2.4.1 Nonlinearity

Nonlinearity effect in scintillation detectors is of great interests nowadays as it affects the peak positions, especially the escape peaks (Gardner et al., 2004). It causes the peak position mismatch between simulated detector response function and experiment. Although there is no widely accepted explanation of this phenomenon, Rooney and Valentine (Rooney et al., 1996, 1997 and Valentine et al., 1994, 1998) have done good experimental works to quantify this phenomenon in different kinds of scintillation detectors. Their experiments involve a range of electron energies generated from Compton scatters to measure the nonlinearity by a Compton coincidence technique (CCT). They treat the scintillation detectors' nonlinearity with electron energy deposited. The electron energy versus relative scintillation yield per electron energy for NaI and BGO are plotted in figure 2-5 based on Rooney and Valentine's work, then empirical models were fitted to describe this relationship.

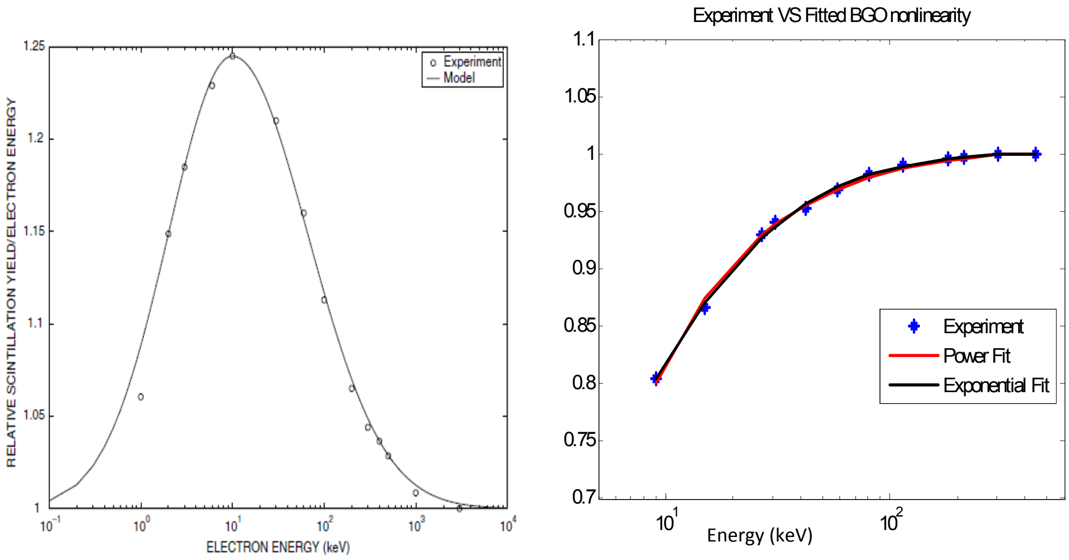

Figure 2-5 Experiment versus model for NaI (left) and BGO (right) nonlinearity with electron energy

The following relationship can be used to formulate the relative NaI and BGO scintillation efficiency versus deposited electron energy (light yield per electron energy).

$$N_{\mathrm{e}}(E_e) = a + b\exp(\frac{-(\ln E_e - k_1)^{k_2}}{k_3}) \tag{2-20}$$

The model data versus experiments also plotted in figure 2-5, and the five parameter values are listed in table 2-3 below.

Table 2-3 Range parameters for NaI and BGO detector calculated from Pages' data

	a	***b***	***k₁***	***k₂***	***k₃***
NaI ($E_e \le 10keV$)	1.000	0.245	2.3026	2	5.1946
NaI ($E_e > 10keV$)	1.000	0.245	2.3026	2	7.1635
BGO	1.0006	-0.3862	0.4918	1.8224	3.9363

The equation has been put in CEARDRFs to handle scintillation detector nonlinearity. When an electron deposits all or part of its energy in the detector, the tallied energy E_t will be the energy deposited multiplied by scintillation efficiency N_{e}

$$E_t = N_{\mathrm{e}}(E_{edep}) \cdot E_{edep} \tag{2-21}$$

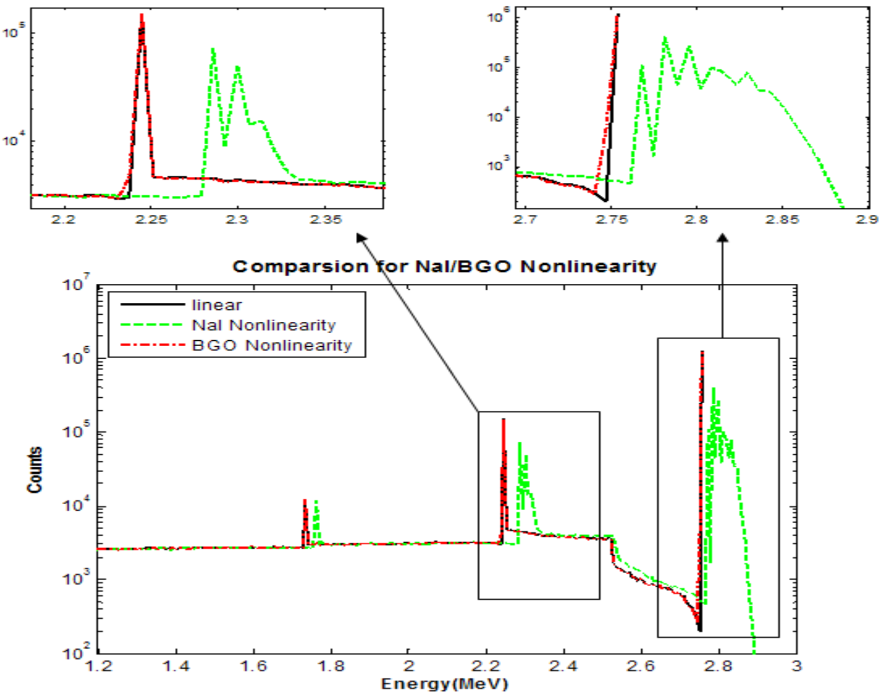

Figure 2-6 Simulated nonlinearity effect of NaI and BGO detector of 2.754 MeV gamma

The simulated flux spectra (without considering detector resolution) for Na-24 high energy peak (2.754 MeV) with linear scintillation efficiency, NaI nonlinearity and BGO nonlinearity are plotted in figure 2-6 respectively. The three peaks are full energy peak, single escape peak and double escape peak from high energy to low. It is easy to see that NaI nonlinearity has a large influence on the peak positions (shift to right side) and has different effects on different energy peaks (single escape peak is shifted further to the right than other two). BGO nonlinearity's influence is small, a little bit shift to lower energy side of peaks. The difference between incident gamma energy and pulse height gamma energy (peak position on flux spectra) is the results of scintillator nonlinearity. After putting in the nonlinearity, the detector response function could match the experimental spectra very well as shown in figure 2-7 (Gardner et al., 2004).

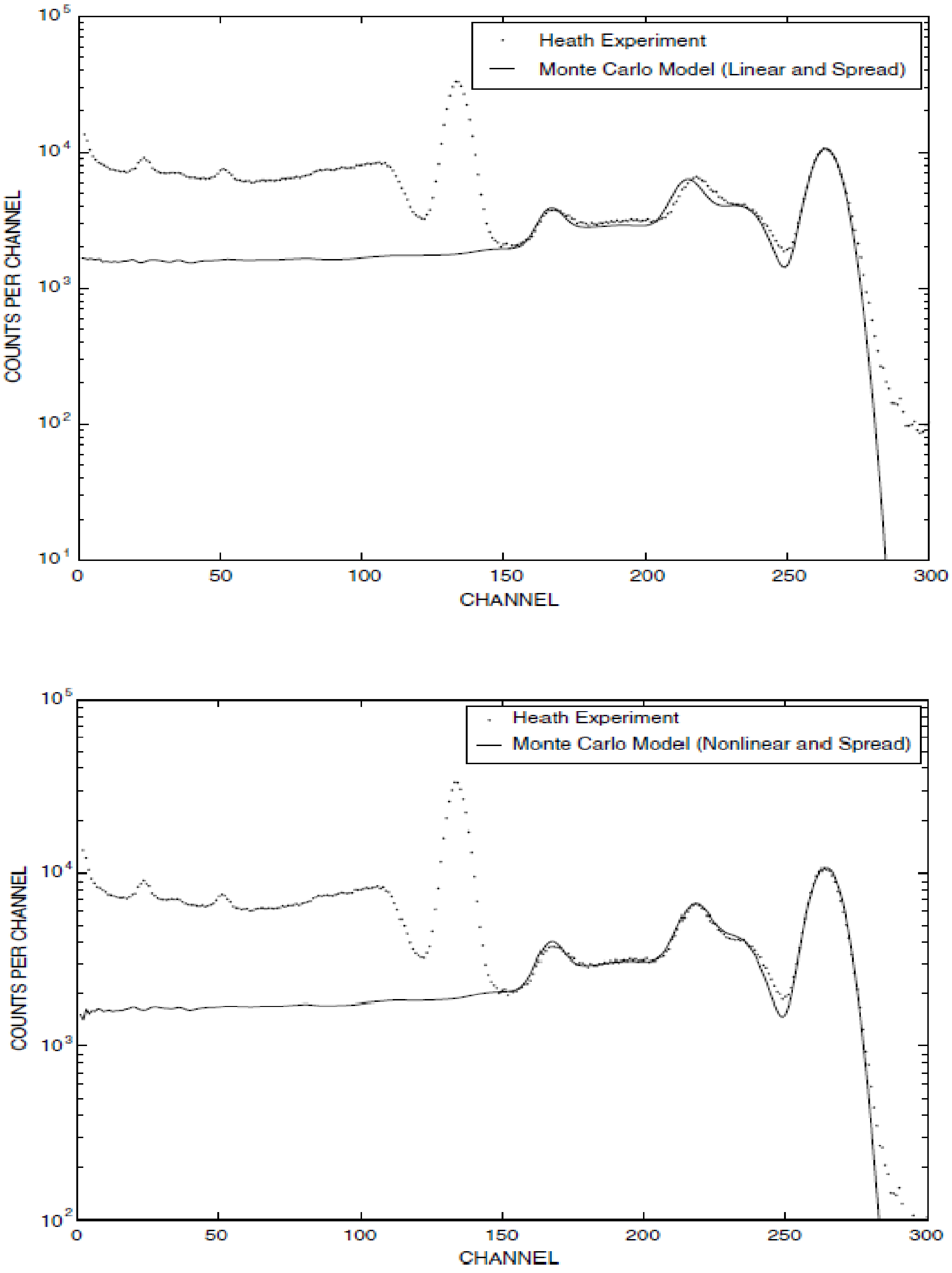

Figure 2-7 Simulated detector response function with and without nonlinearity versus experiment

Normally, this nonlinearity only depends on scintillator type. When we tried to apply this to rectangular shape NaI detector (2”x4”x16”), which is commonly used in homeland security application, we found that it was not as nonlinear as the cylinder shape. The largest face was used in experiment. Thus, light transport efficiency parameter *lte* was introduced to account for the light loss in transport, which is quite normal in long shape detector. For the detector we tested, *lte*=0.2 will make the simulated detector response function match experiments well.

2.4.2 Flat Continuum

With basic principles that utilize the normal exact geometrical description of the detector and the exact physics of photon and electron transport, the intensity of Compton flat continuum in Monte Carlo generated detector response function is often as much as an order of magnitude or more smaller than observed in experiments (Gardner et al., 2004). The physical mechanism of this phenomenon is not very clear, but Gardner believed that detector imperfections and electron channeling from the detector crystal were the reasons. The detector imperfections might cause additional traps of electrons for a period long enough that they are lost from a given photon interaction sequence. Electron channeling from the detector crystal make it easier for electrons to escape from detector.

Both detector imperfection and electron channeling are not easy to put in the Monte Carlo simulation. Thus, a pseudo electron range by a trial-and-error fit to experimental results to take care of the unknown extent of these detector phenomena. In practice, the electron range in CEARDRFs is multiplied by an arbitrary value. The best multiplier will be determined by trial-and-error for the detector case of interest.

In Gardner's work, a model form for the electron range multiplier is taken as

$$\begin{aligned} R_e &= 1 + A_1 \exp(-A_2 E_I) + A_3 \exp(-A_4 E_I) \\ A_1 &= 39.662, A_2 = 3.4052, A_3 = 1.5434, A_4 = 0.1576 \end{aligned} \tag{2-22}$$

where E_I is incident photon energy, A_1 to A_4 are parameters to be derived from experimental data. This model approaches unity as incident photon energy going higher. However, the author found that this model cannot be expanded to BGO detector and NaI detector in other shapes. Although proper multiplier could be determined through trial-and-error to fit the experiments well, more experimental data are still needed to derive reliable models for these detectors.

2.4.3 Gaussian Broadening

Due to the finite resolution of real radiation detectors and statistical effects, the measured spectrum for a mono-energetic photon source will appear as a broadened peak at the source energy. The shape of this peak is approximately Gaussian (characterized in equation 2-23) with the center at the source energy and a width which is characteristic of the specific detector.

$$G(E) = \frac{A}{\sigma\sqrt{2\pi}} \exp\left(-\frac{(E-E_0)^2}{2\sigma^2}\right) \tag{2-23}$$

where *E* is the broadened energy, E_0 is the energy of the tally, *A* is normalization constant and σ is Gaussian standard deviation.

The initial tallied spectra from CEARDRFs is not a "real" spectrum, it is a kind of "spectra flux" without considering the effect of detector resolution as shown in figure 2-6. Thus, proper Gaussian broadening should be applied to the “spectra flux” to get a practical detector response function.

To determine the Gaussian distribution, one needs to know the mean (μ) which is incident particle energy and standard deviation (σ). The formula used in MCNP5 to calculate σ is specified as follows:

$$\sigma = FWHM/\sqrt{8\ln 2} = FWHM/2.3548 \tag{2-24}$$

$$FWHM = a + \sqrt{b(E + cE^2)} \tag{2-25}$$

where E is the photon particle energy in MeV and a, b and c are user-provided Gaussian parameters, FWHM is the full width half maximum, which could be determined from experiments. Instead of using the same formula as MCNP5, we found that the following formula is also a good choice,

$$\sigma = dE^e \tag{2-26}$$

where σ is the standard deviation in MeV, E is the photon particle energy in MeV. Only two parameters are needed and after taking the natural logarithm on both sides, the two parameters could be determined from linear equation.

$$\ln\sigma = \ln d + e\ln E \tag{2-27}$$

For example, the following table 2-4 could be obtained from experiments of 2”x2” NaI detector experiments,

Table 2-4 Experimental data of 2”x2” NaI detector to determine Gaussian broadening parameters

E(MeV)	Elow	Ehigh	FWHM	Sigma	lnE	lnSigma
0.411(Au198)	0.3912	0.4309	0.0397	0.016859	-0.88916	-4.08287
0.662(Cs137)	0.6357	0.6857	0.05	0.021233	-0.41249	-3.8522
1.12(Sr46)	1.0832	1.1558	0.0726	0.03083	0.113329	-3.47925
1.332(Co60)	1.2883	1.3701	0.0818	0.034737	0.286682	-3.35994
2.754(Na24)	2.6777	2.8244	0.1467	0.062298	1.013054	-2.77583

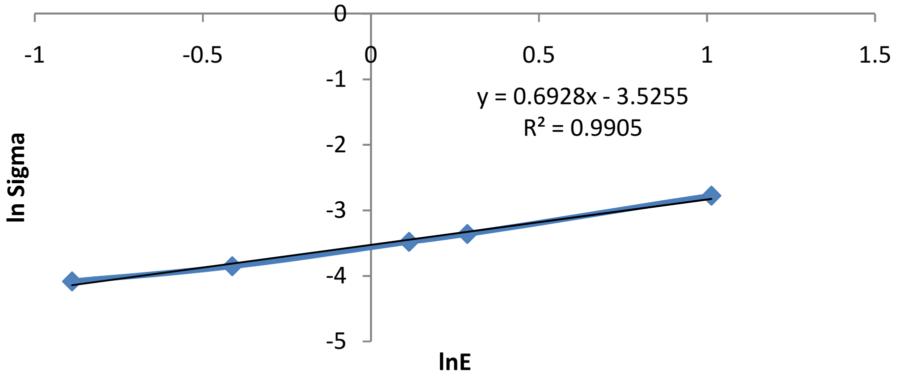

Figure 2-8 Linear fitting of equation (2-27) on 2”x2” NaI experimental data

The experimentally determined Gaussian broadening parameters are listed in table 2-5 for various detectors. Although there is slight difference between different detectors, even in same size, the table can serve as a reference and are the default values in CEARDRFs.

Table 2-5 Gaussian broadening parameters for different detectors.

	2”x2” NaI	**3”x3” NaI**	**6”x6” NaI**	**2”x2” BGO**	**2”x4”x16” NaI**
d	0.02953	0.03027	0.02609	0.04221	0.02721
e	0.6928	0.6593	0.6027	0.6363	0.6224

One issue should be pointed out is the additional broadening introduced by nonlinearity, which should be compensated. More details could be found in Gardner’s research (2004).

In CEARDRFs, the Gaussian broadening is applied after all simulation histories have been done instead of applying to each history as MCNP5 does. Some researchers (Metwally et al., 2004, Gardner et al., 2007) show that this approach can reduce the total number of histories of the simulation by up to two orders of magnitude to reach the same statistical requirements.

2.5 Benchmark Experiments

Cylindrical NaI detector response functions generated by G03, the former version of CEARDRFs, have been proven to agree with experiments well and show a large improvement over MCNP5 generated DRFs (Gardner et al., 2004). After expanding to new scintillator and more shapes, more experiments are also needed to benchmark CEARDRFs.

2.5.1 Experiments Setup

The experiment setup shown in figure 2-9 left was used by Heath. The source is 10cm away from the center of front face of detector. The detector is shielded in a thick lead box. The major difference between the conditions of the Heath experiments and the CEARDRFs conditions are,

(1) The experiments were done in air rather than vacuum;

(2) The experiments have surroundings, like lead shielding, rather than being in an infinite vacuum, and there is aluminum can around the detector and PMT.

(3) The CEARDRFs only treats a single gamma-ray energy and doesn't consider beta particles or other gamma-rays that might be present from a given radioisotopes.

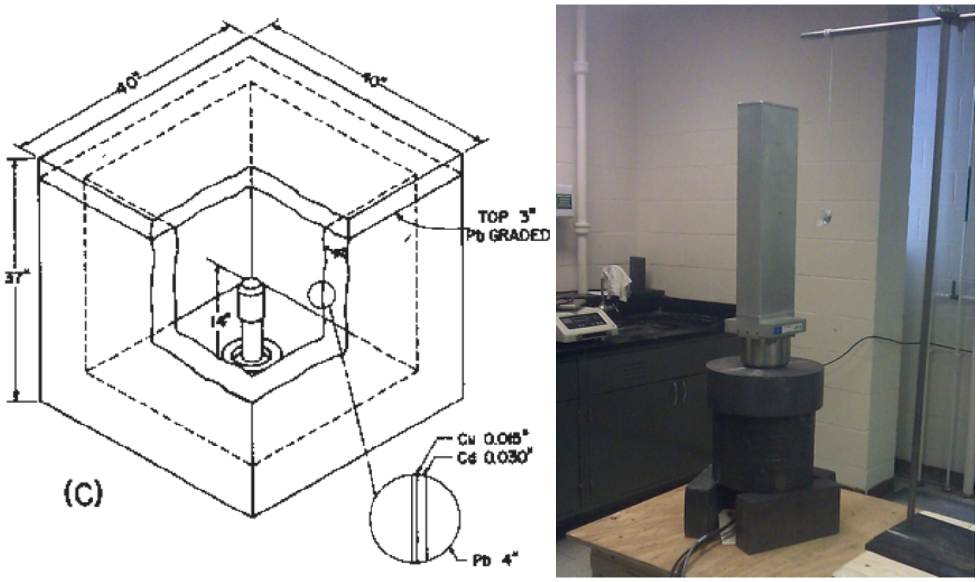

Figure 2-9 Experiment setup of Heath (left) and rectangular NaI detector at CEAR (right)

Thus, our experiments were carried out in a big empty room to reduce the scattering from the surrounding environments, although the scattering cannot be eliminated thoroughly. For cylindrical detectors, the radioisotopes were placed 10cm away from the center of from surface. For rectangular detector, they were placed 10cm away from the center of the largest surface.

In the following comparisons, if more than one gamma-ray energy emitted from radioisotopes, then CEARDRFs generated single energy DRF will be summed up according to the emitting percentage to compare to experiments. Four radioisotopes were used to verify the CEARDRFs generated DRF (table 2-6).

Table 2-6 Radioisotopes used in CEAR experiments

	Cs-137		**Co60**		**Na24**		**Al28**
Energy(MeV)	0.662	0.033*	1.173	1.332	1.368	2.754	1.779
Probability	0.8998	0.0727	1.00	1.00	0.9999	0.9986	1.00

* Combination effects from Ba137m beta particles.

2.5.2 2”x2” BGO Cylindrical Detector

The comparisons among experiments, MCNP5 generated DRFs and CEARDRFs generated DRFs for 2”x2” BGO cylindrical detector are plotted in figure 2-10 to 2-13. All spectra are normalized to their highest peaks. Overall, CEARDRFs generated DRFs show large improvements over MCNP5 generated DRFs and agree with CEAR experiments quite well. The improvements include more accurate full energy peak to Compton continuum ratio, full energy peak to full energy peak ratio and full energy peak to escape peaks ratio, better valley shape, and more accurate peak positions after proper gain-shifting.

Please note that, in figure 2-10 and 2-11, the peaks around 0.2-0.3 MeV are backscattering peaks, which originate from the gamma-rays that scattered back from surrounding materials. The backscattering peak is not legit part of DRF as stated in previous section. For Na24 and Al28, we had to make them from PULSTAR reactor at NCSU as they are short life isotopes. For some reasons, there were some contaminations which contribute to the low energy parts in figure 2-12 and 2-13. In figure 2-10, the difference between spectra CEARDRF and CEARDRF-add is the x-ray escape peak from BGO crystal was added back in the second spectra which makes a perfect shape of the low energy side of full energy peak. As energy goes higher, this does not need to be treated separately.

2.5.3 2”x4”x16” NaI Rectangle Detector

The comparisons among experiments, MCNP5 generated DRFs and CEARDRFs generated DRFs for 2”x4”x16” BGO cylindrical detector are plotted in figure 2-14 to 2-16. All spectra are normalized to their highest peaks. Overall, CEARDRFs generated DRFs show large improvements over MCNP5 generated DRFs and agree with CEAR experiments quite well. Other discussions are similar to 2”x2” BGO detector.

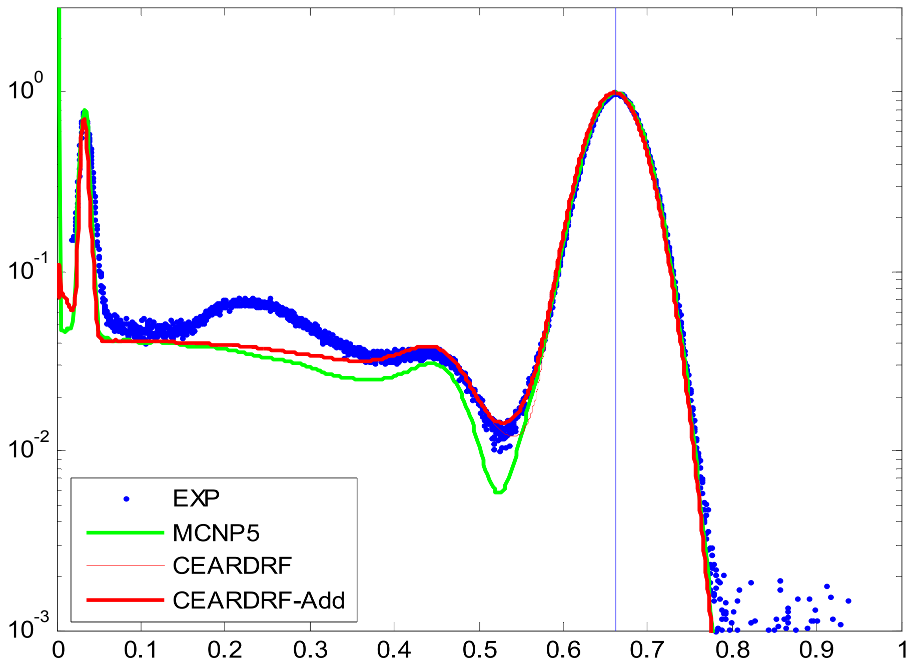

Figure 2-10 Comparison among Cs137 experiment, MCNP DRF and CEARDRFs DRF for 2”x2” BGO

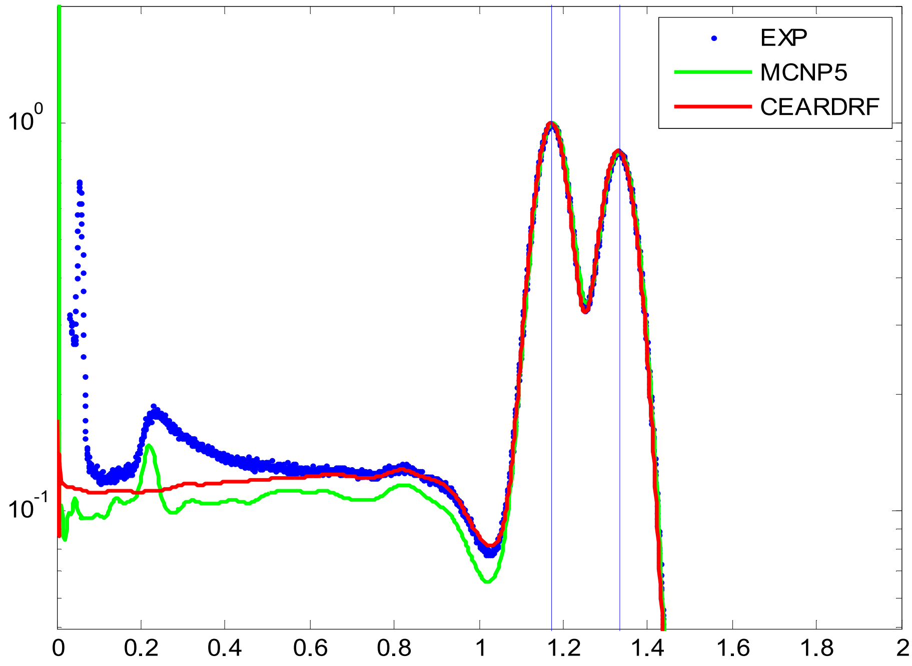

Figure 2-11 Comparison among Co60 experiment, MCNP DRF and CEARDRFs DRF for 2”x2” BGO

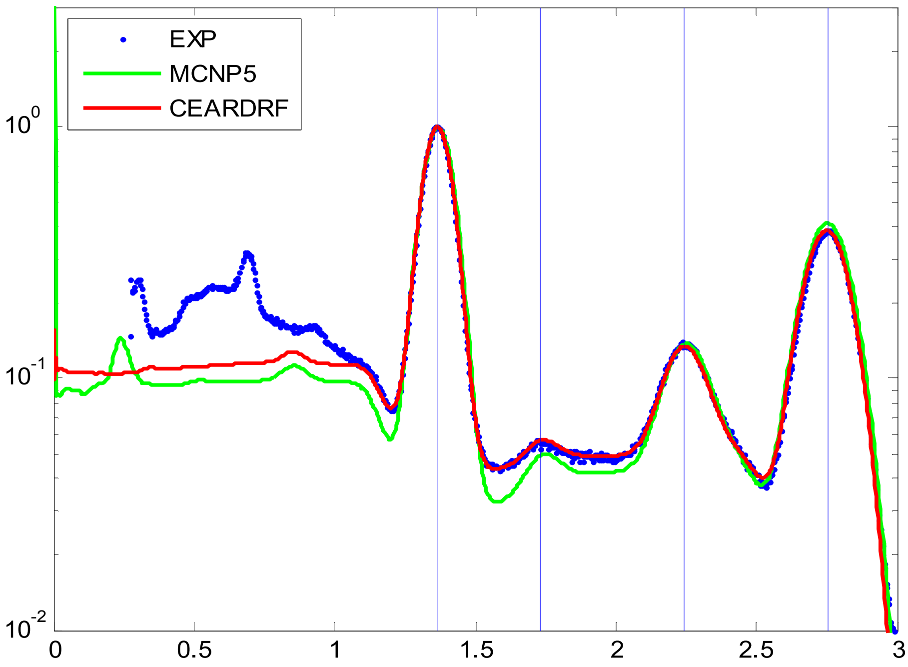

Figure 2-12 Comparison among Na24 experiment, MCNP DRF and CEARDRFs DRF for 2”x2” BGO

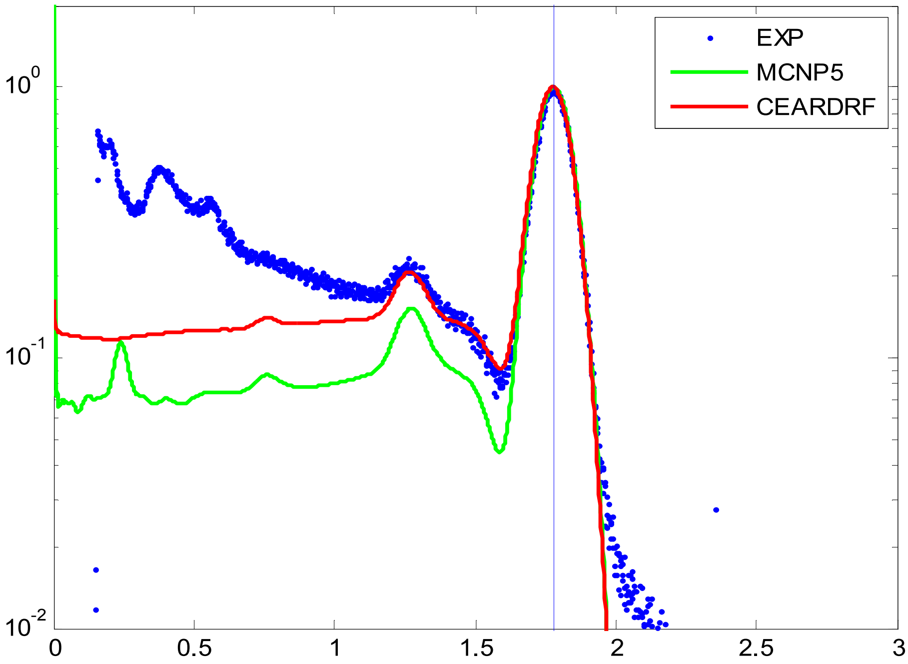

Figure 2-13 Comparison among Al28 experiment, MCNP DRF and CEARDRFs DRF for 2”x2” BGO

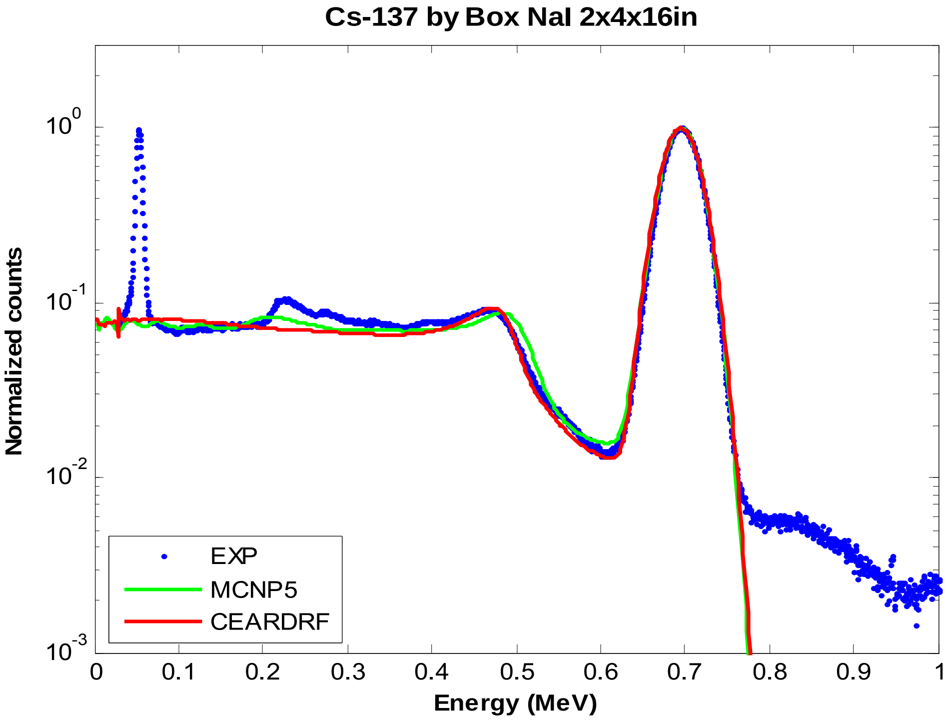

Figure 2-14 Comparison among Cs137 experiment, MCNP DRF and CEARDRFs DRF for 2”x4”x16” NaI

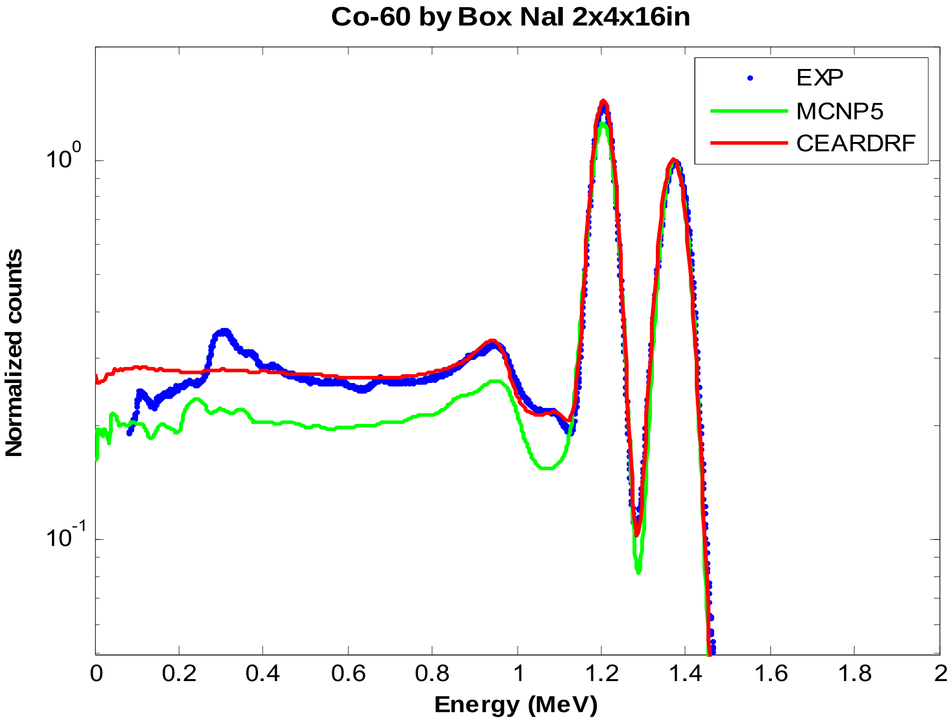

Figure 2-15 Comparison among Co60 experiment, MCNP DRF and CEARDRFs DRF for 2”x4”x16” NaI

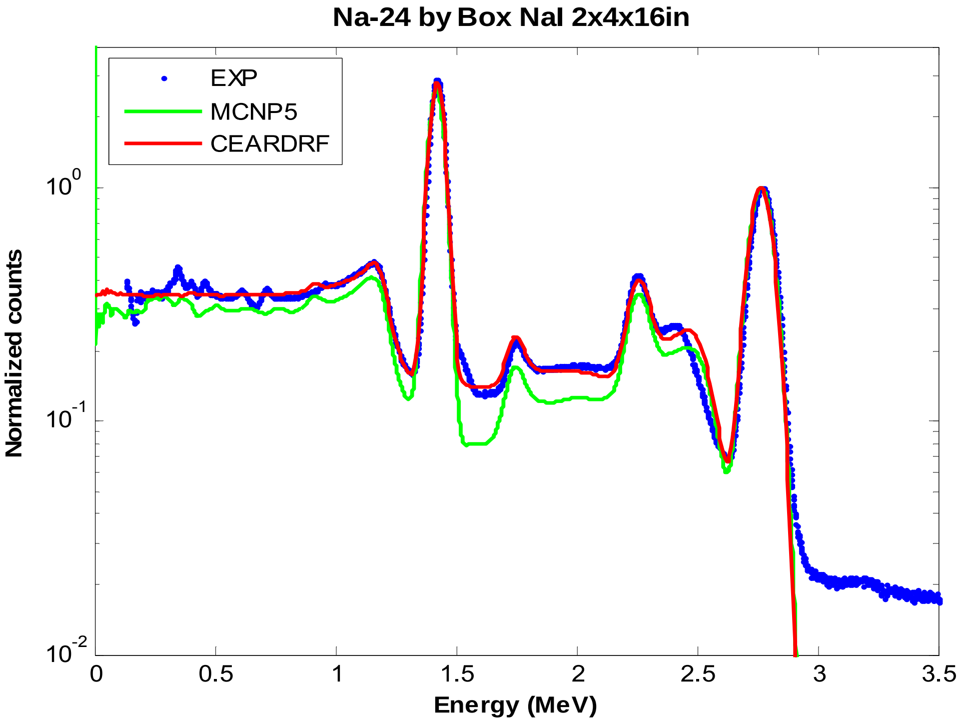

Figure 2-16 Comparison among Na24 experiment, MCNP DRF and CEARDRFs DRF for 2”x4”x16” NaI

2.6 Features and applications of CEARDRFs

The code CEARDRFs can generate accurate detector response functions for cylindrical or rectangular NaI and BGO detectors as shown in previous sections. With empirical parameters of scintillation detector nonlinearity, flat continuum adjustment and Gaussian broadening, there are big improvements over the most popular and widely recognized general purpose Monte Carlo code MCNP5. Also, the generation of detector response function is much faster than MCNP5. For 2.754MeV energy, only 59 seconds are need for the execution of CEARDRFs. That is over hundreds of times speed improvements that benefited from the hybrid empirical approaches. Also, with user provided parameters, the code CEARDRFs can be easily expanded to other type of scintillators such as LaBr, LSO, .etc. We currently do not hold these types of detectors at CEAR. Otherwise, these empirical parameters will have been put in the code.

As shown in figure 2-1, the code CEARDRFs is usually used with another Monte Carlo code to handle the outside of detector. It could be some specified purpose code like CEARXRF or CEARCPG that we have been using, or other general purpose Monte Carlo code like MCNP5. For the better accuracy, the path length through detector of the incident gamma-rays should be recorded to adjust the weight when scoring, as the source position fixed in CEARDRFs when generating detector response function.

3 CODE CEARCPG

3.1 Overview of CEARCPG

The PGNAA Monte Carlo simulation codes have been developed at CEAR for decades. Rooted from numerous efforts of CEAR, CEARCPG (Han, 2005) was developed as the first specific code that can be used to simulate both the single and coincidence spectrum of coincidence PGNAA, including relatively complicated neutron and photon transportation. For neutron, the two most important reactions related to prompt gamma-rays, neutron capture and inelastic scattering reaction completely follow the principles of nuclear physics, which empower the simulation of coincidence prompt gamma-rays. For photon, the three major interactions, Compton scattering, photoelectric and pair production, are included in the code. The benchmark experiments showed good agreement between experiments and simulation for both single and coincidence spectra.

The most important contribution of CEARCPG is a new algorithm is developed to sample the neutron-produced coincidence gamma-rays following nuclear structure. Once a nucleus is excited by either neutron capture or neutron inelastic scattering reaction, the decay scheme is strictly followed. Because this process is very fast, all gamma-rays emitted when the excited nucleus de-exited to the ground level are considered to be coincidence prompt gamma-rays. The ENDF/ENSDF data libraries are accessed to obtain the decay schemes. In the past, the commonly used method is the pre-calculated gamma-ray table for every photon-producing neutron interaction, such as MCNP. When generating prompt gamma rays in Monte Carlo simulation, the table is sampled to provide the gamma-ray information. In this way, the information of the origin of the gamma rays is lost even we know the energy and intensity of each prompt gamma ray. The algorithm limits the existing Monte Carlo code to be extended to coincidence simulation. The algorithm developed in CEARCPG makes it possible to simulate the coincidence spectrum by using the Monte Carlo method.

More details about CEARCPG can be found in figure 3-1. Some other features of CEARCPG are listed below:

1) It is a new Monte Carlo code and is written with Fortran 95. Dynamic memory allocation technique and public memory allocation make it easy to regulate and update.
2) It is modularized. It makes the users easy to write their own patch or implement the module of CEARCPG into the other code.
3) Most of the input decks used in CEARCPG are the same as those used in MCNP. The geometry part of CEARCPG is fully compatible with MCNP, except macrobodies and repeated structures in MCNP5. There is no difficulty for MCNP users to use this code. Also, VisED can be used to visualized the geometry.
4) There is no need to pre-process ENDF/ENSDF data libraries, like NJOY does for MCNP. CEARCPG can access the ENDF/ENSDF data library directly. It is convenient for users to update the nuclear data. The users only need to copy the newer nuclear data into the right directory

Also, there are a lot of variance reduction techniques used in CEARCPG to make the code more accuracy and efficiency, including:

1) Russian roulette. This technique is used in conjunction with the expected value technique to randomly terminate the neutron or gamma-ray history if its cumulative weight falls below a specified value.

2) Truncated exponential probability density function. This technique is used for those particles that reach the system boundary and could fly out of the system along their current flight direction. In this case, the flight distance to the next interaction is sampled from the truncated exponential probability density function to force the next interaction to occur before it escapes out of the system.

3) Direction biasing. The flight directions of the gamma rays are sampled in a transformed fictitious probability density functions that result in sampling more frequently along their last flight directions. For the initial flight direction of a gamma ray at the site of its emission, it is always biased toward the detector.

4) Discrete importance function. This technique is used to increase the neutron capture interaction sampling frequency for those elements whose capture interaction cross sections are less than 10% of the elastic interaction cross section.

5) Stratified sampling approach. It is employed to force all the important prompt gamma-rays of a given element from the radioactive capture interaction to be emitted and the resultant prompt gamma rays are tracked independently.

6) Expected value splitting approach. This approach is employed to make the gamma ray of interest to score at every interaction site by splitting it into two parts or two sub-particles. One of which is assumed to directly go to the detector without any interaction along its flight path with the expected weight assigned to that process, the other with remaining weight will have one or more interactions based on normally tracking process.

7) Correlated sampling. This technique is used to predict the change in the detector response due to the slight composition variation of the sample. It is implemented during the normal process of particle tracking.

8) Detector response function. By this technique, the process of tracking any gamma ray stops once it reaches the detector and the score of the gamma ray incident on detector is tallied and is converted to detector pulse height responses after all the simulation histories finish. The detector response functions are usually more accurate as discussed in previous chapter.

3.2 Parallel Implement of CEARCPG

Although CEARCPG is a very powerful Monte Carlo code with many variance reduction techniques, it has been written for serial computation only. This means that even though modern computer usually has multi-core processor, it could only utilize one of those cores. The very time-consuming simulation on single CPU core highly limited the usage of the code. Thus, parallel computation feature should be added to the code.

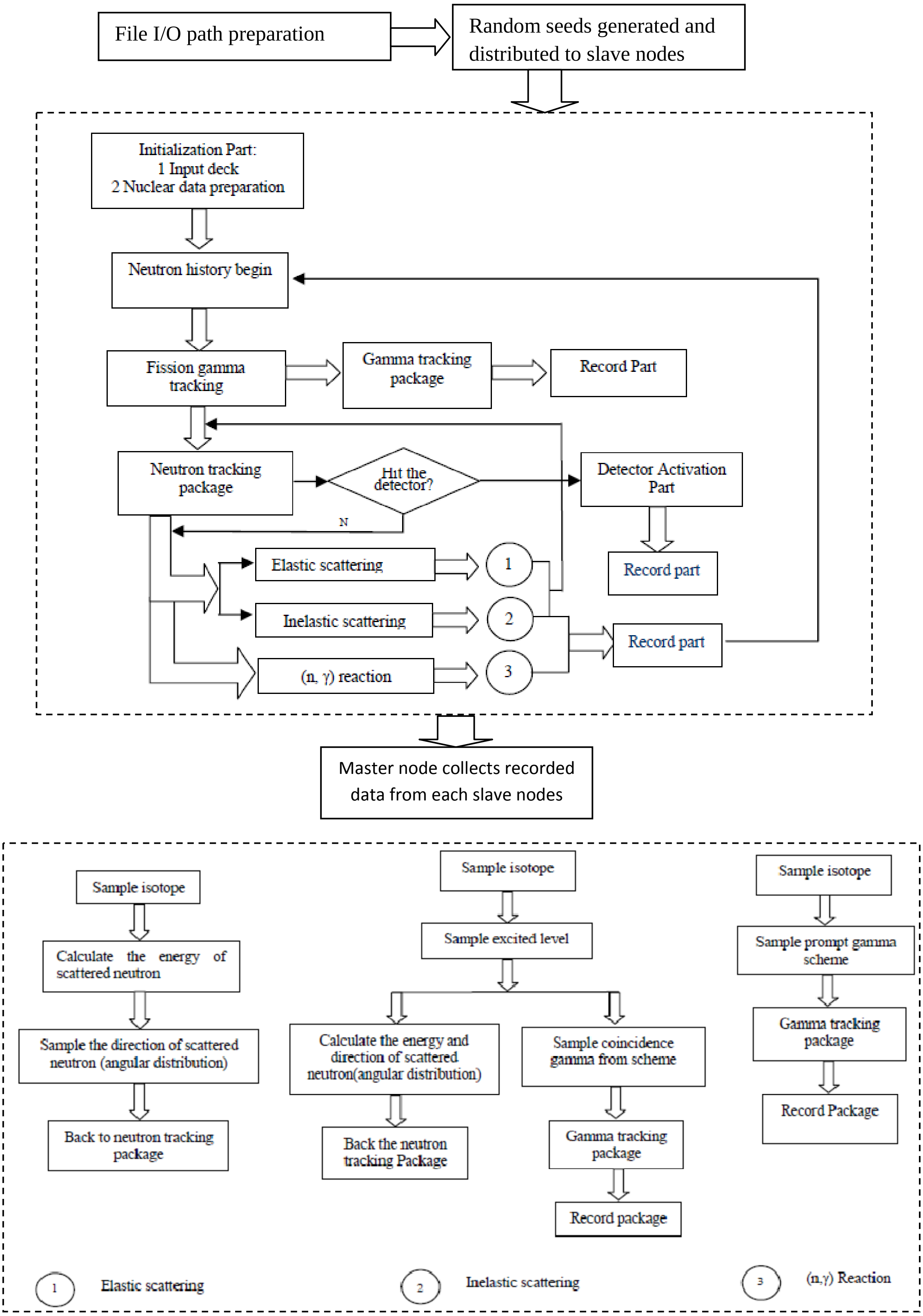

Figure 3-1 The flow chart of CEARCPG and its parallel implement

Message Passing Interface (MPI) is a communications protocol that allows processes to communicate with one another by sending and receiving messages. Message Passing Interface Chameleon (MPICH) is a freely available, portable implementation of MPI, which is available for most flavors of operation systems, including Slackware, the Linux distribution on CEAR cluster “Spectral”. MPICH is also a developed program library that could be coded in program directly.

The parallel computation environments on CEAR cluster “Spectral” were accomplished through MPICH2, which is a high-performance and widely portable implementation of the Message Passing Interface (MPI) standard (both MPI-1 and MPI-2). Generally speaking, parallelize a program means to rewrite a large part of the code. As discussed in previous section, CEARCPG is a relatively complicated code involving neutron and photon transport based on ENDF/ENSDF nuclear data libraries. Implementing parallel computation feature with MPICH2 inside the code will be too expensive, as the data structure, the algorithms, and a lot of more things need to be changed. Instead of that, the outside approach has been applied to parallelize CEARCPG.

The flow chart of parallel CEARCPG is shown in figure 3-1. Clearly, the major parts of CEARCPG (in dashed boxes in figure 3-1) remain unchanged. MPI is only used to initialize all slave nodes at the beginning of execution and collect recorded data after all simulations have been done. At the beginning, the master node assigns certain history number and different random seeds to different slave nodes. Different file input/output (I/O) path also assigned to different slave nodes. After all the simulations have been done, the master node collects the recorded data from all the slave nodes and formalizes those as the final simulation results. Several scripts in bash/perl/python have been used to do these jobs outside the original CEARCPG.

Monte Carlo problem is a perfect fit to this simple approach. All different histories are totally independent with each other and there is no communication needed between nodes in the simulation process. There are several advantages to use this simple outside approach with CEARCPG,

1) It is dramatically simplified the job to parallelize the code. There is no need to touch the inside of CEARCPG. All the features can be naturally inherited.

2) The ideally linear speed-up feature of parallelization could be nearly reached. Optimally, the speed-up from parallelization would be linear—doubling the number of processing elements should halve the runtime. However, duo the communication between nodes, which obviously cannot be parallelized, internal parallelization approach has a near-linear speed-up for small numbers of processing elements, which flattens out into a constant value for large numbers of processing elements as shown in figure 3-2 (Amdahl, 1967).

The disadvantage of this approach is load balance problem between different slave nodes. On some nodes, the particles might run into complicated situation that need more time to finish while on some others, the particles could be terminated quickly. Thus, the total runtime is determined by the node that takes the longest time.

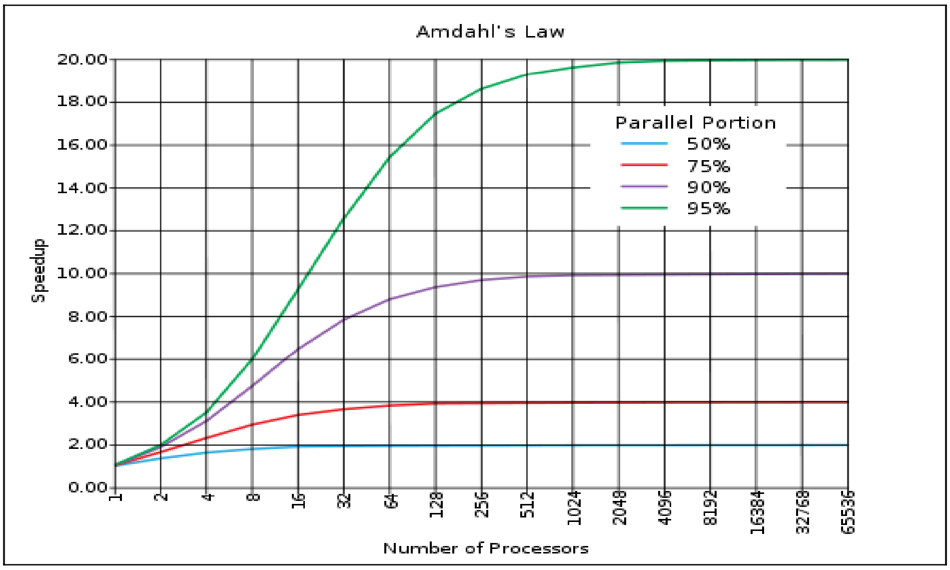

Figure 3-2 A graphical representation of Amdahl's law

3.3 Differential Operator (DO) Implement of CEARCPG

The Differential Operator method was discussed in literatures (Hall 1982; Rief 1984; Rief 1994). It is very powerful tool for measurement sensitivity study and system optimization. The basic idea of the differential operator technique is, if the magnitude of perturbation is very small, the ratio of changed response can be found by using Taylor series expansion.

The Monte Carlo – Differential Operator method has been implemented in CEARCPG for simulating differential responses of sample and elemental library spectra. Instead of re-run the code CEARCPG again, according to new estimated values of elemental weight fractions, library spectra can be re-adjusted with Taylor series expansion. This Taylor series re-adjustment process can be repeated until accurate estimation is reached. Since the DO method is purely mathematical and deterministic, the run time of Taylor series re-adjustment (several seconds) is trivial compared to the run time of the Monte Carlo simulation code (several hours).

In combination with library least square approach, the differential operators approach is a very important addition in that it allows one to use the Monte Carlo simulation code only once for each separate class of samples, for example, a series of different coal with similar composition.

Detailed derivation about differential operator and an example of its application can be found in later chapter.

3.4 Other Improvements of CEARCPG

The code CEARCPG was originally developed under Windows platform. To execute it on the cluster, which is a different platform, Slackware Linux, certain modifications have been made to the code to take care of the platform change.

Also, a lot of exception treatments have been added in the code to make it more robust. The neutron libraries used in CEARCPG includes 97 isotopes of practical interest. Each isotope has three separate data libraries. Two of them are for neutron capture reaction and neutron inelastic scattering reaction from ENSDF to access the structure information; and one is for neutron cross sections and angular distributions of neutron after reaction from ENDF. It is very hard to have one code to handle all of them, especially when some of them might have errors or different format. For example, the neutron capture ENSDF data library of ^{41}K uses a different level index from others. Another example is the neutron inelastic scattering ENSDF data libraries of ^{57}Fe, missing the second excited level. The missing level caused a dead loop as the excited nucleus cannot return to the ground level.

The overall comparison between MCNP and CEARCPG can be found in table 3-1.

Table 3-1 Comparison between CEARCPG and MCNP5

	CEARCPG	**MCNP5**
Nuclear data	ENDF/B-VII ENSDF EPDL	ENDF/B-VII ENSDF with NJOY format EPDL
Neutron interaction	Neutron capture reaction	Same
	Neutron elastic scattering reaction (Free gas thermal Treatment)	Same
	Neutron inelastic scattering reaction (n, n' γ)	All inelastic scattering reaction, such as (n.n') (n,2n) etc.
Generation of neutron-induced photons	Sampling from isotope scheme	The number is function of neutron weight, photon limit weigh, photon production cross section, etc. Expanded photon production method &30X20 photon production method
Photon interaction	Simple Physics Treatment	Simple Physics Treatment & Detailed Physics Treatment
Variance reduction technique	Stratified sampling	general
Parallel Computation	Yes	Yes
Perturbation	Differential operator with variance reduction technique considered. Applicable to pulse height spectra	Only to flux

4 PROMPT GAMMA-RAY MODELING

The optimization of coincidence PGNAA analyzer heavily relies on Monte Carlo simulation. As we know, the biggest disadvantage of coincidence measurement is its low counting rate. Even the new electronic device have been developed rapidly in the past ten years, the low counting rate of coincidence measurement is still the “bottle neck”. Thus, the objective is to improve the gamma-ray detector counting rate, both single and coincidence. The modeling could be classified to four parts: general optimization, geometry arrangement, detector and neutron source. Some of the results have been summarized by the author and published in Nuclear Instruments and Methods in Physics Research Section A (Wang et al., 2010).

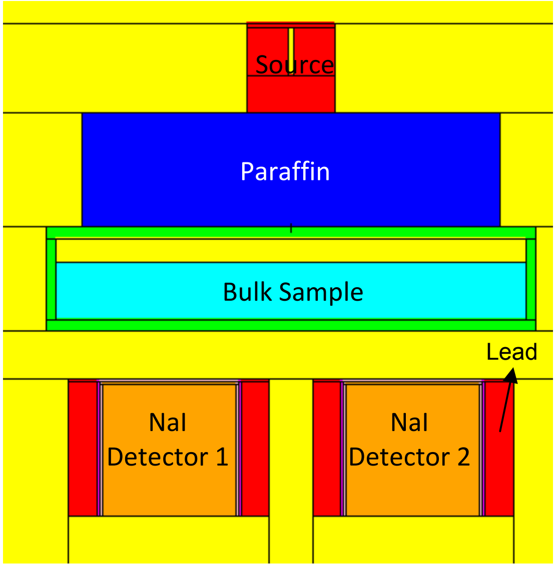

Figure 4-1 Preliminary coincidence PGNAA setup in CEAR laboratory

Figure 4-1 shows the preliminary coincidence PGNAA setup tested at CEAR (Gardner et al., 2000, Matwallet et al., 2004, Han et al., 2005). It has been used as the reference setup in the optimization process.

4.1 Monte Carlo Simulation Codes

The overall approach in accomplishing this project engages using Monte Carlo simulation. Both the specific purpose code CEARCPG (Han, 2005), developed at CEAR of North Carolina State University, and the general purpose codes MCNP5 (LANL, 2004), have been used to predict experimental results and investigate the optimized setup of PGNAA device. Some of the results are specifically related to bulk analyzer, while others can also be used in other application involving neutron and gamma-ray.

MCNP5 is a general-purpose, neutron, photon, and electron transport simulation code, which was developed at the Los Alamos National Lab. The simulation results of MCNP5 is well recognized and widely accepted. MCNP5 can be used to simulate prompt gamma rays. However, MCNP5 cannot simulate coincident prompt gamma rays, which are considered to be the most useful to improve the signal-to-noise ratio in neutron-related applications, where normally the gamma ray background would be very intense. The coincidence counting technique (Metwally, 2004; Gardner et al., 2000) has been investigated in CEAR and has been proved to be able to improve the signal-to-noise ratio. Therefore, MCNP is not considered the final simulation platform, but is still used in this project as a powerful tool for estimating multiple response and distribution of neutron and prompt gamma-rays.

As introduced in previous chapters, specific purpose Monte Carlo code for PGNAA has been developed by our CEAR group over decades, which gave birth to CEARCPG that is capable of simulating coincident prompt gamma rays (Han, 2005). After further improvements, including parallel computation and differential operator features, it is very useful to predict the detector response, both single and coincidence, in PGNAA application and use the simulated spectra in MCDOLLS quantitative analysis. Here, CEARCPG has been used to simulate detector spectrum to benchmark with experiments results in the future.

Generally speaking, MCNP5 can coarsely guide the optimization with its numerous tallies and features on most aspects; CEARCPG can simulate the coincidence spectra to fine tune the analyzer and prepare elemental libraries for MCDOLLS analysis. All of the simulations were run on the CEAR parallel computing cluster, named “Spectral”. The cluster consists of 41 nodes. Each equipped with an AMD Phenom X4 9950 quad-core processor, 2.6GHz, 1 GB RAM, and a 40 GB hard drive. Each node runs the Slackware Linux. The nodes are interconnected via 1000Mb/s Ethernet switches and share files through a NFS server.

One script shall be mentioned is MCNP_PSTUDY, which is written in perl to automate the setup, execution, and collection of results from a series of MCNP5 Monte Carlo calculations (Brown et al., 2004). The script has been modified to run on our “Spectral” cluster and performed really well.

4.2 General Optimization

4.2.1 Moderator

^{252}Cf spontaneous neutron source is one of the most commonly used thermal neutron sources in PGNAA analyzers. It has an average energy of 2.2MeV, and its neutron energy spectra could be described by Maxwellian distribution.

$$N(E) = Ce^{-E/1.42}E^{0.5} \tag{4-1}$$

Among all types of neutron interactions, the inelastic scattering interaction and radiative capture interaction are the most important reactions to produce prompt gamma rays. Most part of ^{252}Cf neutron energy is below the thresholds of neutron inelastic reaction for most isotopes (table 4-1) in the bulk sample that we are interested, and neutron capture cross section is about 2 magnitudes higher than neutron inelastic reaction and follows 1/v rules. Thus, thermalizing the Cf-252 might be needed in certain circumstance, especially for small laboratory size sample. The self moderation can be enough for large bulk sample as shown in later sections.

Two common moderator materials have been investigated, paraffin and water, in a simple setup. A rectangular shape moderator is placed with surface (50cm x 30cm) facing the neutron source. The neutron energy fluxes across the opposite surface are simulated with MCNP5 F2 tally for various moderator thicknesses.

The neutron energy flux spectra after going through moderator are shown in figure 4-2 to 4-5. For both moderators, thermal neutron increases first due to thermalization and then decrease due to attenuation in moderator. Through MCNP5 simulation, a 6 to 8 cm thick paraffin (figure 4-3) or 7 to 10 cm thick water (figure 4-5) has been found to be suitable for small size sample (For example, 9.7cm x 6.7 cm cross section in this work). For a 6cm thick paraffin or 7cm water, thermal neutron and fast neutron flux are about 50% VS 50% across the moderator surface facing sample, which could have a higher neutron capture (n, gamma) reaction rates and guarantee good penetration into the sample.

Table 4-1 Threshold energy of neutron inelastic scattering reaction for common elements in coal

Number	**Element**	**Threshold energy (MeV)***
1	Hydrogen	N/A
2	Carbon	4.812
3	Nitrogen	2.479
4	Oxygen	6.431
5	Sodium	4.493
6	Magnesium	1.426
7	Aluminum	8.753
8	Silicon	1.843
9	Phosphorous	1.310
10	Sulfur	2.305
11	Chlorine	1.255 (35),1.774(37)
12	Potassium	2.588
13	Calcium	3.437
14	Titanium	1.004
15	Manganese	0.128
16	Iron	0.862
17	Nickel	1.479(58) 1.355(60)
18	Mercury	0.159

* Listed threshold energy is for the most dominant isotope in natural abundance, if A is not listed in brackets.

The comparisons between the two moderators are plotted in figure 4-6. Water needs to be a little bit thicker to maximize the thermal neutron flux from ^{252}Cf. The self attenuation of neutron flux is greater for paraffin than water at the same thickness; however, the maximum thermal neutron flux is higher for paraffin than water. Due to carbon in the paraffin, the prompt gamma from paraffin can be possible interference to the analysis of bulk sample. Prompt gamma-rays from moderator will be less for water than paraffin as oxygen has smaller cross section for thermal neutron interaction and higher threshold energy for inelastic scattering interaction.

Following the MCNP5 simulation results, the paraffin moderator thickness is modified to be 7.3cm instead of the originally used 13cm in reference setup (figure 4-1). The amount of neutron hits the sample can be increased by a factor of two. As a result of that, the prompt gamma-rays emitted from the sample also double the reference value. CEARCPG has been used to simulate the coincidence prompt gamma-ray events. The simulated history number is 4×10^7 in both cases. 1,463,449 coincidence events were detected in the original setup while 3,754,878 coincidence events detected with thinner paraffin moderator. The simulation results show a factor of 2.56 improvements for total detected coincidence events.

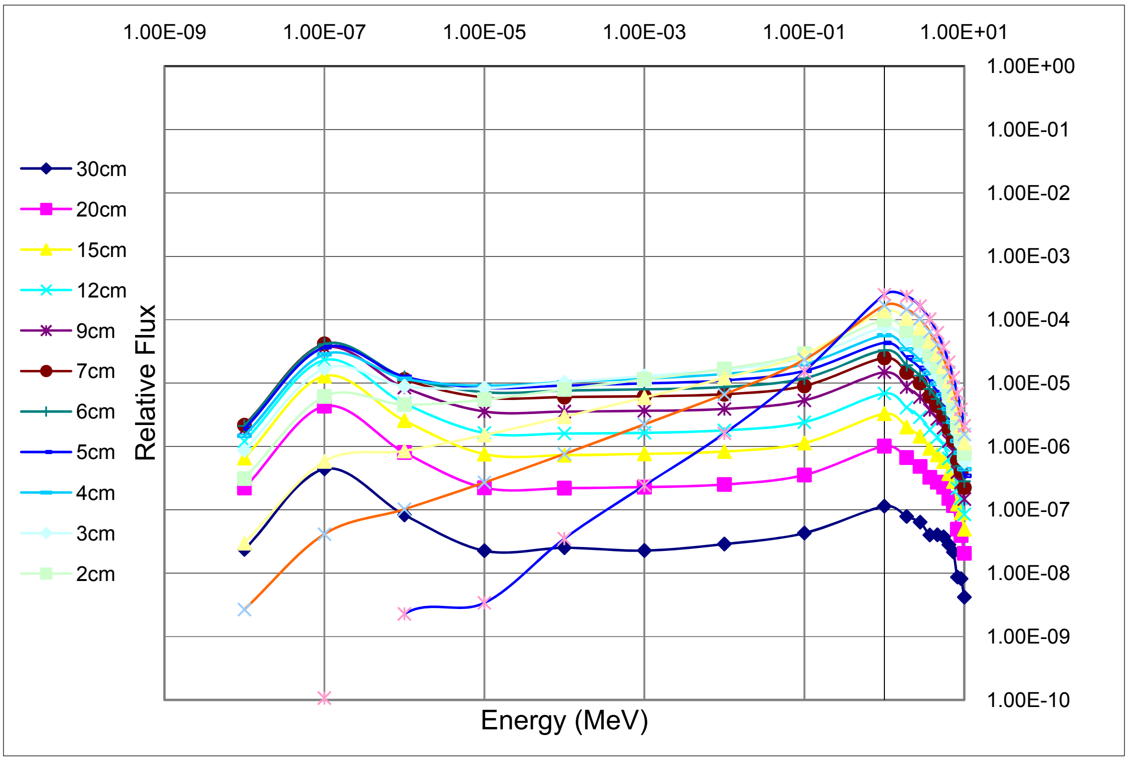

Figure 4-2 Energy spectra of 252Cf neutron flux after moderation of different thickness of paraffin

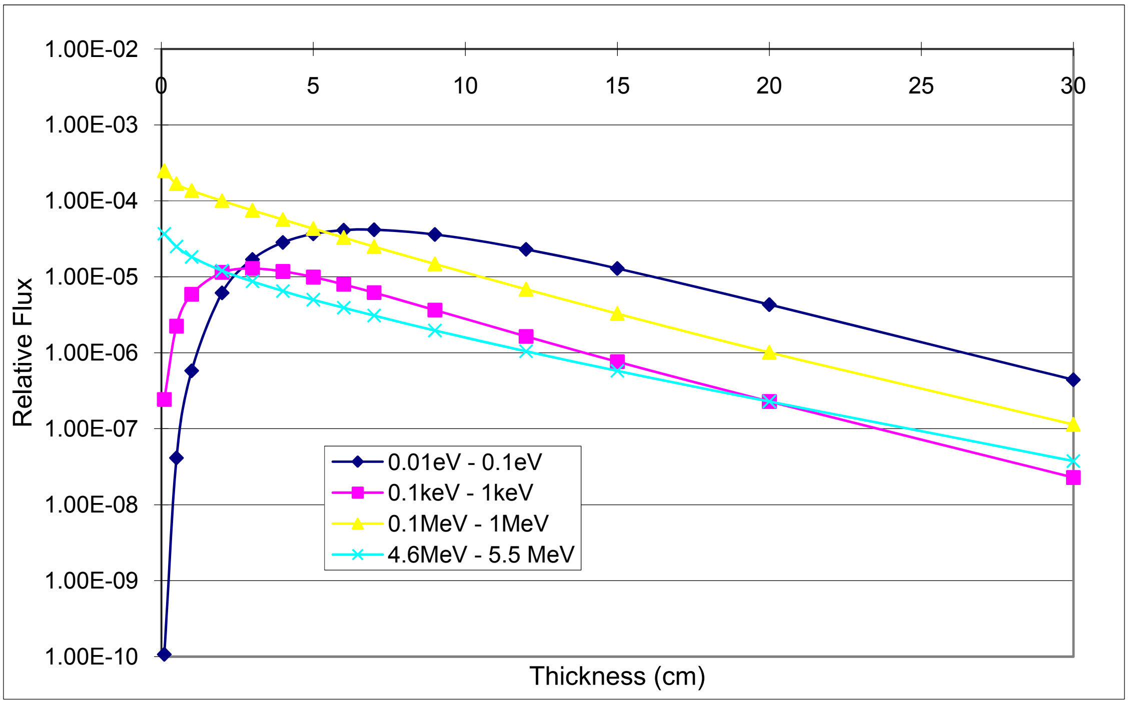

Figure 4-3 Amount of neutron after different thickness of paraffin in various energy ranges.

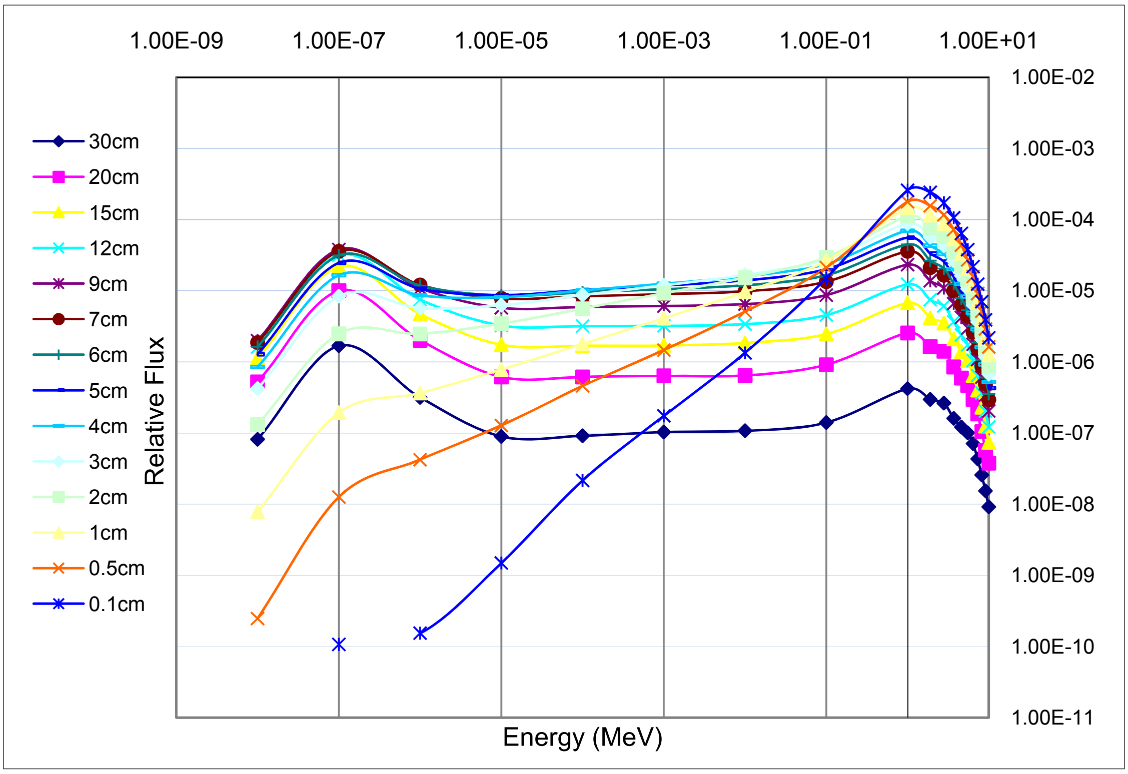

Figure 4-4 Energy spectra of 252Cf neutron flux after moderation of different thickness of water

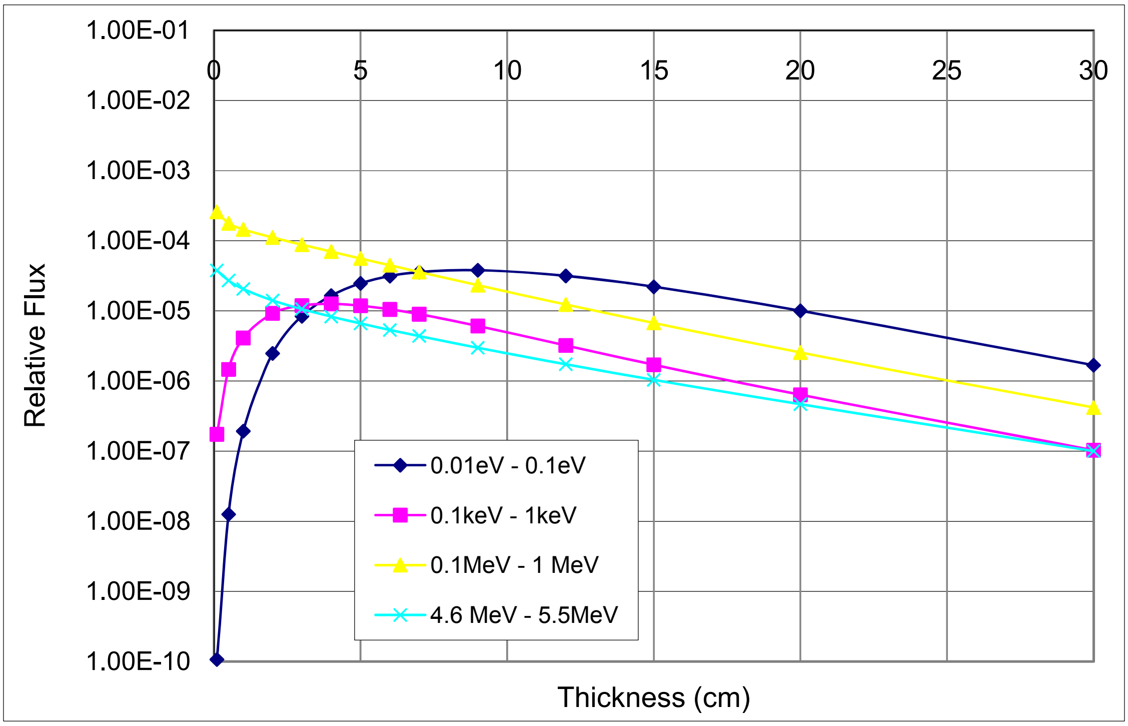

Figure 4-5 Amount of neutron after different thickness of water in various energy ranges

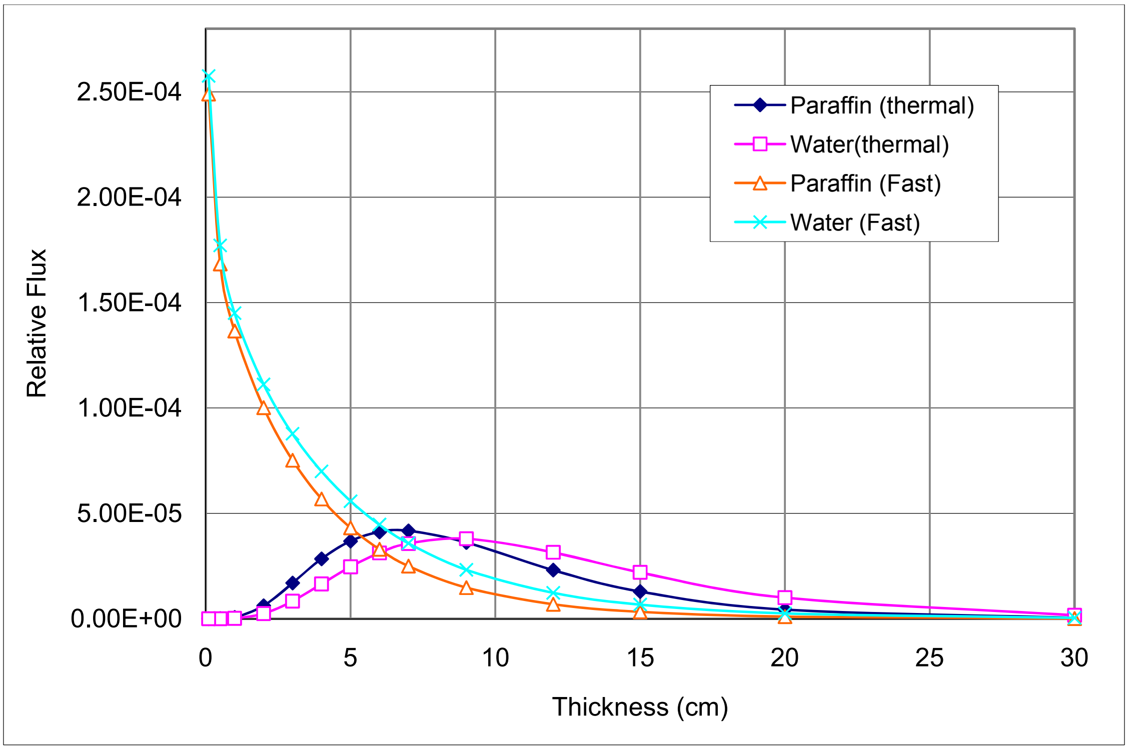

Figure 4-6 Comparison between paraffin and water for various thickness

4.2.2 Neutron Distribution

To reach the best coincidence detection, the placement of ^{252}Cf neutron source and two detectors needs to be optimized to detect as much prompt gamma-ray as possible. Thus, the neutron energy flux spatial distribution in the bulk sample has been simulated to indicate where the prompt gamma rays come from. The simulation has been done with MCNP5 mesh tally feature. Three shapes of bulk sample have been investigated, including two rectangular samples (70cm x 80cm x 20cm and 55cm x 9.7cm x 6.7 cm) and a conveyor belt shaped sample (45 degree troughing angle, 60cm bottom width, 80cm margin width). The bulk material simulated is coal as bulk coal analysis is where PGNAA widely used.

For small lab size sample (55cm x 9.7cm x 6.7 cm), the source placement is not that important. As long as the neutron source is placed facing the center of the sample with moderator of proper thickness, thermal neutron could distribute all over the sample.

No moderator is used for large rectangular sample and conveyor belt shape sample, and there are two places for the neutron source. (1) The neutron source is placed under the sample and 30cm away from the center of bottom surface (left parts in figure 4-7 and 4-8); (2) it is placed one side of the sample and 30cm away from the center of edge (right parts in figure 4-7 and 4-8). In figure 4-7 and 4-8, the top plot is neutron radioactive capture rate which is the origin of most prompt gamma-rays; the middle plot is thermal neutron (0-0.026ev) which is highly correlated with neutron radioactive capture reaction; and the bottom plot is fast neutron (1-10MeV).

The neutron radiative capture reaction rate maps show where the prompt gamma-rays come from, which agree with the thermal neutron (0-0.026ev) maps as shown in figure 4-7 and 4-8. These figures also indicate that radiative capture reactions happen all through the coal sample with highest production in the center area, if the source is placed under the sample; and the reaction is biased to the side near the source with highest production at 8cm and 15cm distance away from the edge for rectangular and conveyor belt shape sample separately, if the source is placed at one side of the sample. The fast neutron (1-10MeV) maps show the self moderation of coal sample, which has a higher concentration close to source and very few could go through the large size coal sample without thermalization. Besides the biased reaction center, the side source position has reaction rates less than 50% of that of the center source position due to smaller solid angle of source facing sample.

Thus, it is better to place the source under the large size bulk sample. No moderator is needed as the self moderation of sample is enough for ^{252}Cf neutron source. The prompt gamma-rays production is all through sample with a concentration in the center of sample. So the PGNAA can provide average results of the entire bulk sample which is better than chemical sampling analysis. A more direct indication of the detector placement is the photon flux maps in next chapter.

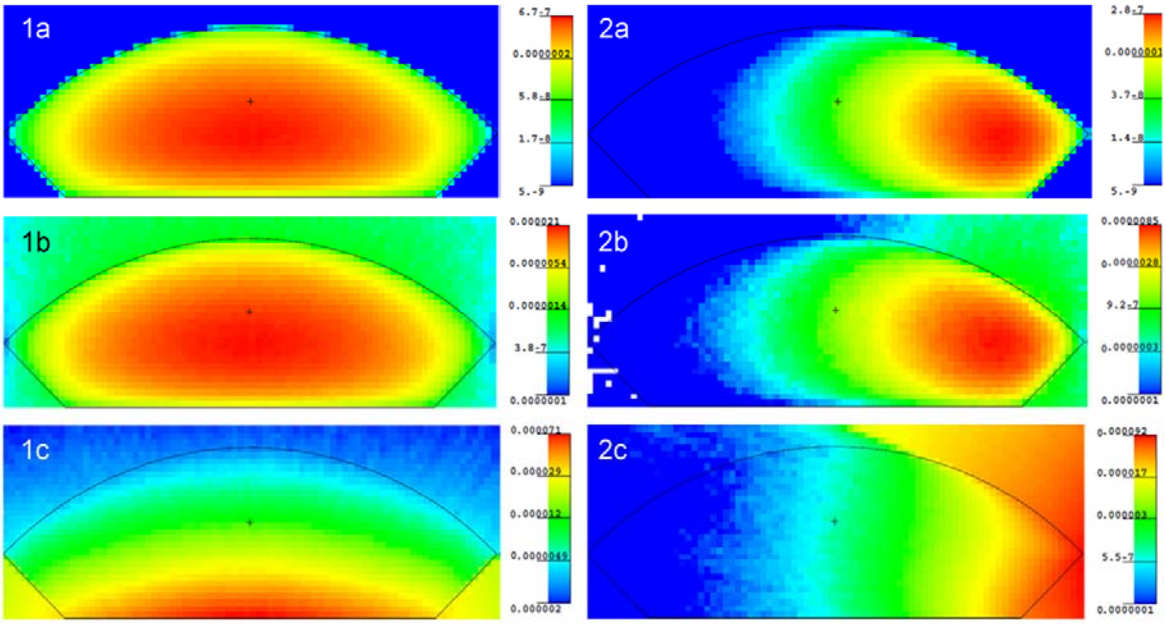

Figure 4-7 Neutron flux spatial distribution in the conveyor belt shape coal sample

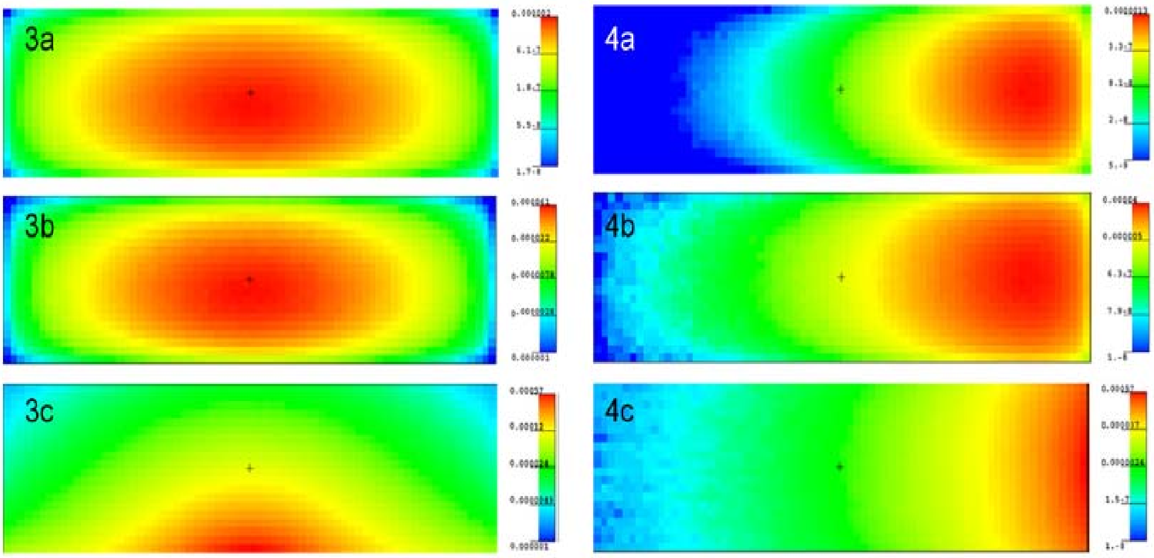

Figure 4-8 Neutron flux spatial distribution maps in the large rectangular shape coal sample

4.2.3 Prompt Gamma-ray Distribution

The gamma-ray flux spatial distribution around the bulk sample has also been simulated with MCNP5 mesh tally feature to show where the prompt gamma-rays go. It also provides additional information about prompt gamma ray production in the sample and the transport of the gamma-rays.

For the small sample, it is intuitive to place the source facing the center of the biggest surface of sample. Here, the neutron source is facing the center of bottom face and 10cm away. Figure 4-9 is the photon flux distribution around the small coal sample. It shows that photon emitted from the sample is nearly isotropic in azimuthal angle and it is better to place the detector as close to the sample as possible to get a higher counting rate.

In coincidence detection, we can find that gamma-rays emitted from left-right surfaces are close to those from top-bottom surfaces, which are both suitable for detecting. However, since the best bottom position is occupied by the source and its accessories, two detectors facing the left and right surfaces might be the best choice.

For large rectangular sample and conveyor belt shape sample, figure 4-10 shows the prompt gamma-ray spatial distributions. The neutron source arrangement is the same as figure 4-7 and figure 4-8. It indicate that prompt gamma-rays emitted from the sample is nearly isotropic in azimuthal angle with a higher value as close to sample center, if the source is placed under the sample; and the highest prompt gamma-ray flux is biased to the side near the source with highest production at 8cm and 15cm distance away from the edge for rectangular and conveyor belt shape sample separately, if the source is placed at one side of the sample. These results agree with the neutron distribution well as described in the previous section.

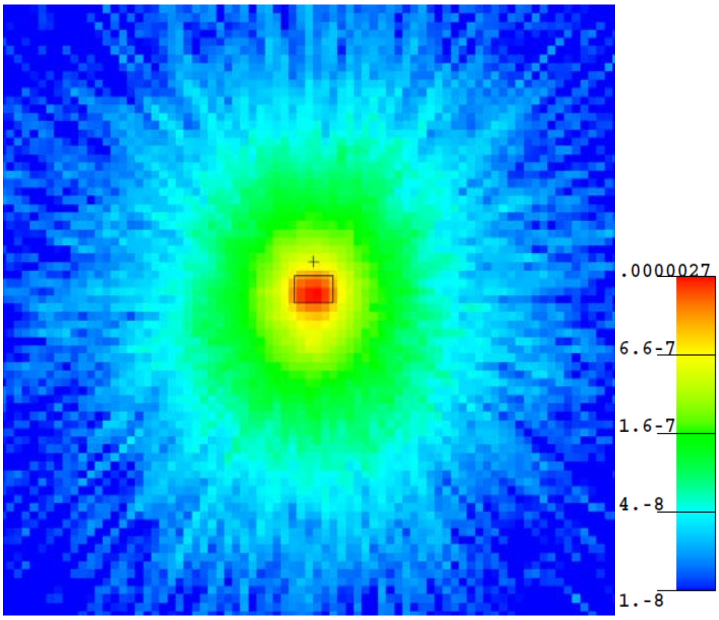

Figure 4-9 Gamma-ray flux distribution around the small coal sample

So, in coincidence detection, it is better to place the detectors facing the top and bottom surfaces separately if possible. Otherwise, placing the two detectors together on the opposite side of neutron source is also a good arrangement.

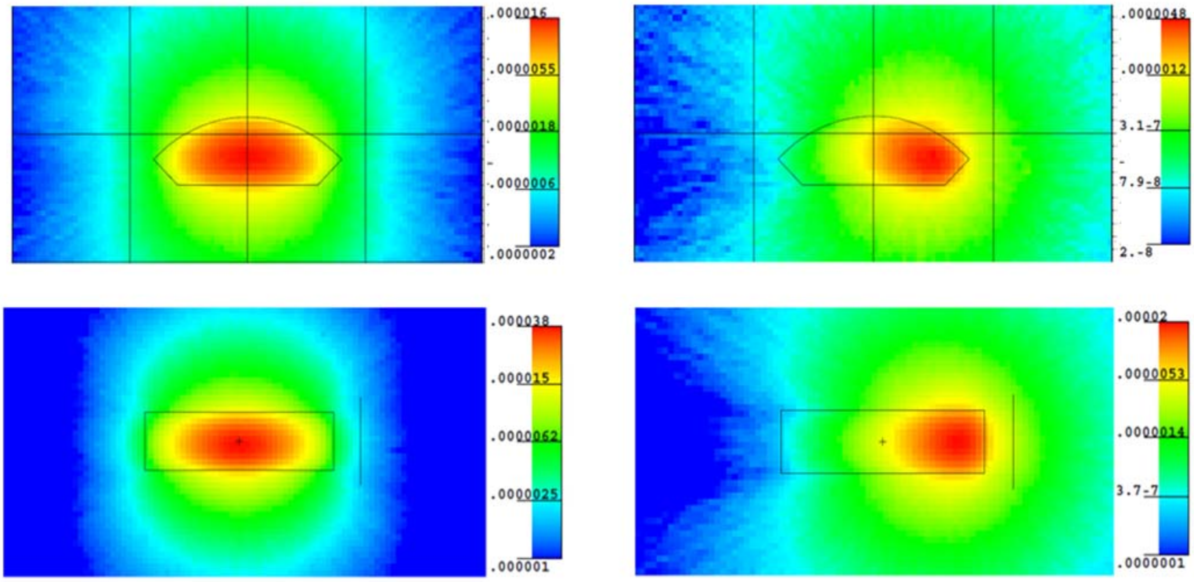

Figure 4-10 Gamma-ray flux spatial distribution maps
They are around the large rectangular shape coal sample and the conveyor belt shape coal sample. Source placements are the same as described in figure 5.

4.3 Geometry Arrangements

According to the simulation results of previous sections, certain geometry arrangements of neutron source and detectors have been chosen for different sizes of bulk samples: lab size sample and large size sample that similar to bulk sample on conveyor belt.

4.3.1 Lab Sample

The lab sample that investigated here is 55cm x 9.7cm x 6.7 cm, which is a representative of the small size sample commonly used in lab. A paraffin moderator of optimized thickness 7.3cm is used to thermalize neutron. As shown in the previous simulation of neutron and prompt gamma-rays distribution in and around the bulk sample, the ^{252}Cf neutron source is placed on top side of the sample and facing the center. The source is placed in a 5cmX5cmX5cm lead shielding box to shield the spontaneous fission gamma. The detectors are on left and right sides of the sample and shielded with 1” lead ring to eliminate other background gamma-rays and cross-talk between detectors as much as possible. Also, a can of 3mm thick boron carbide is used outside the detector to alleviate the detector activation by neutron source. The setup with two 6”x6” NaI detectors is plotted in figure 4-11.

Another arrangement of interest is to replace the two 6”x6” cylindrical NaI detectors with two slab NaI detectors, which could cover bigger solid angle facing the sample with similar or less detector volume. Figure 4-12 shows such a setup that replaces the cylindrical NaI detectors with two slab (16”x4”x2”) NaI detectors with the largest surfaces facing the sample to cover the biggest solid angle. The slab detector of this size has also been chosen for portal monitoring application.

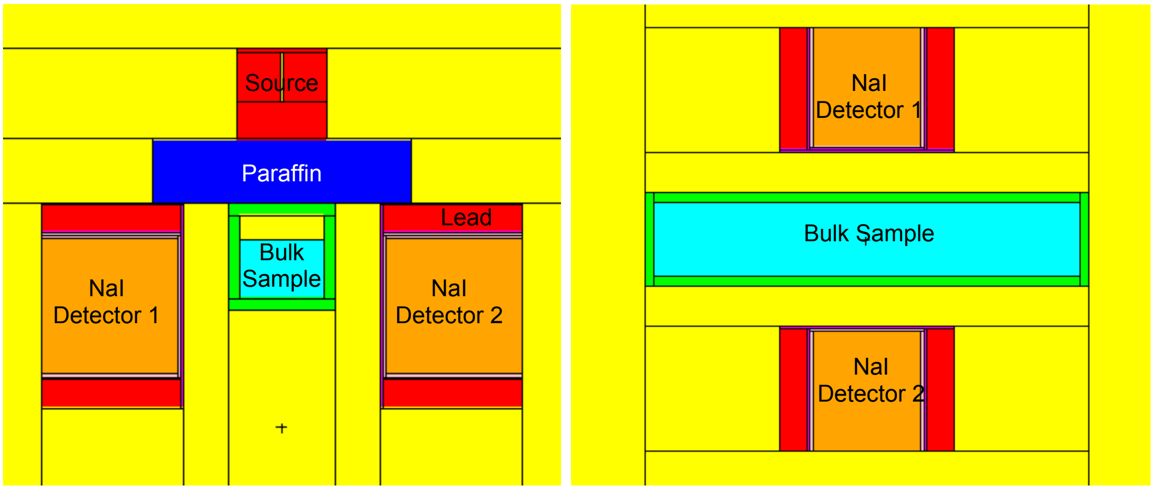

Figure 4-11 6”x6” cylindrical NaI detectors arrangement for lab sample

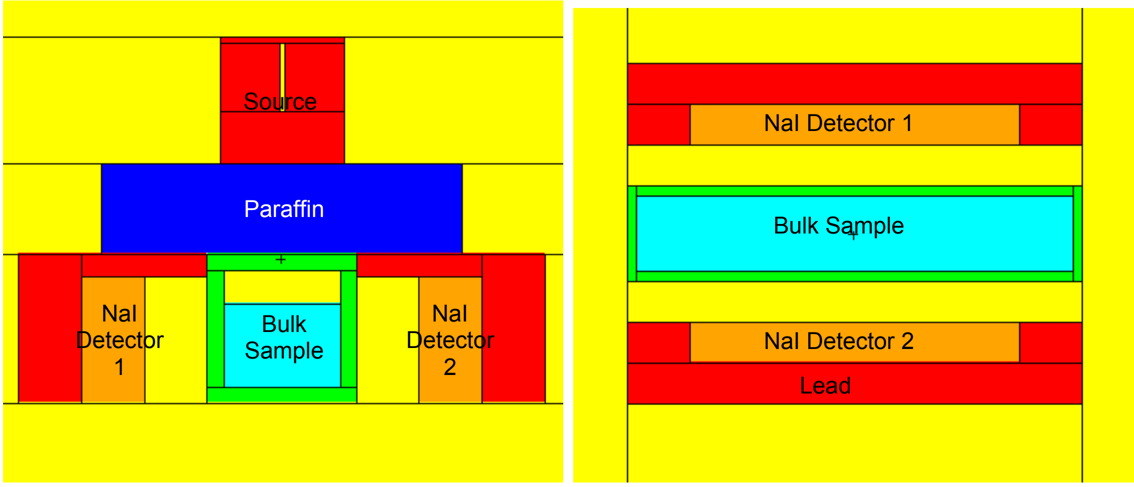

Figure 4-12 Slab NaI detectors arrangement for lab sample

According to the simulation of CEARCPG, it is easy to compare these setups with the reference setup in figure 4-1. Both the single detected events and coincidence events show a great improvement with the new geometry arrangement and new slab detectors.

For single detection, the detector response from Sulfur and Mercury, the two elements of high interests, is plotted in figure 4-13 and 4-15. Comparing with the reference setup, replacing the paraffin moderator with an optimized thickness will increase the overall detector response about a factor of 4.3 (blue versus black in the two figures). Changing the 6”x6” detectors position from bottom to left-right sides can further increase the overall detector response another factor around 1.6. Finally, using the 16”x4”x2” slab detectors at the left-right sides position to replace the 6”x6” cylindrical NaI detectors can gain another increase of a factor around 9.5 in the overall detector response. In sum, the slab detector left-right arrangement can detect around 65 times more single gamma-ray events than the reference setup.

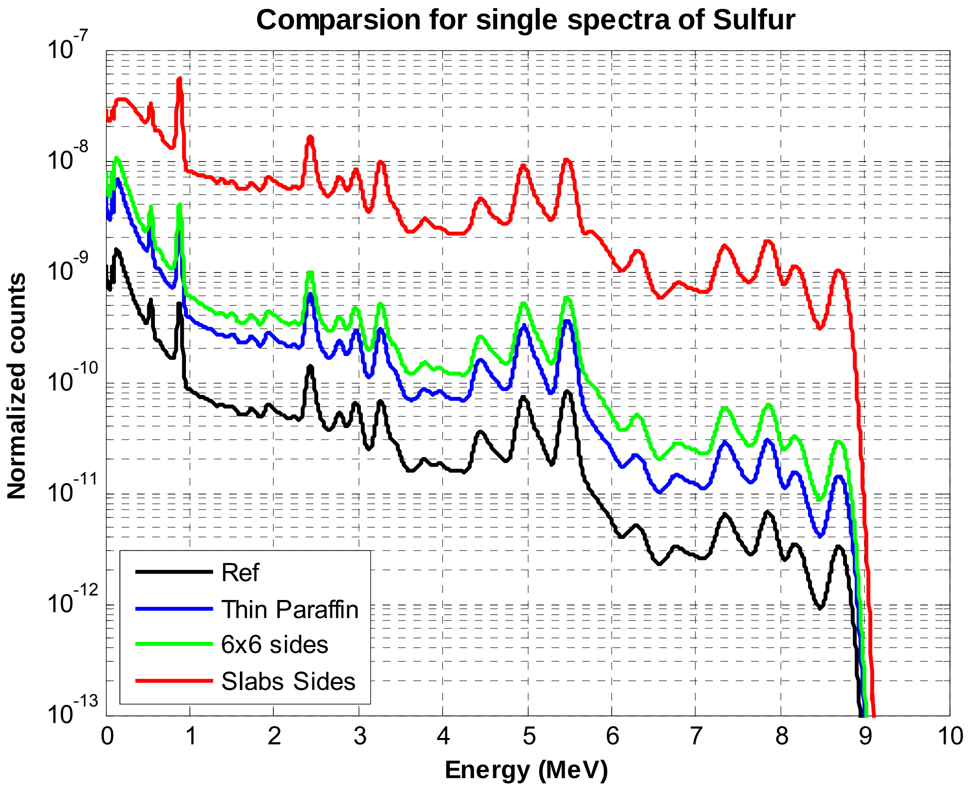

Figure 4-13 Comparison of single spectra of Sulfur for lab sample

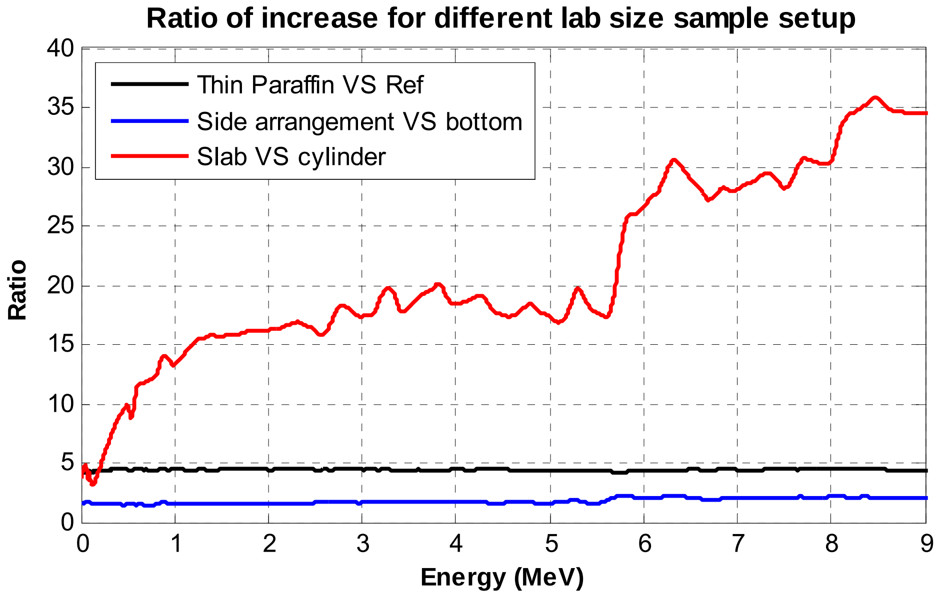

Figure 4-14 Ratio of increase in single response of Sulfur for lab sample

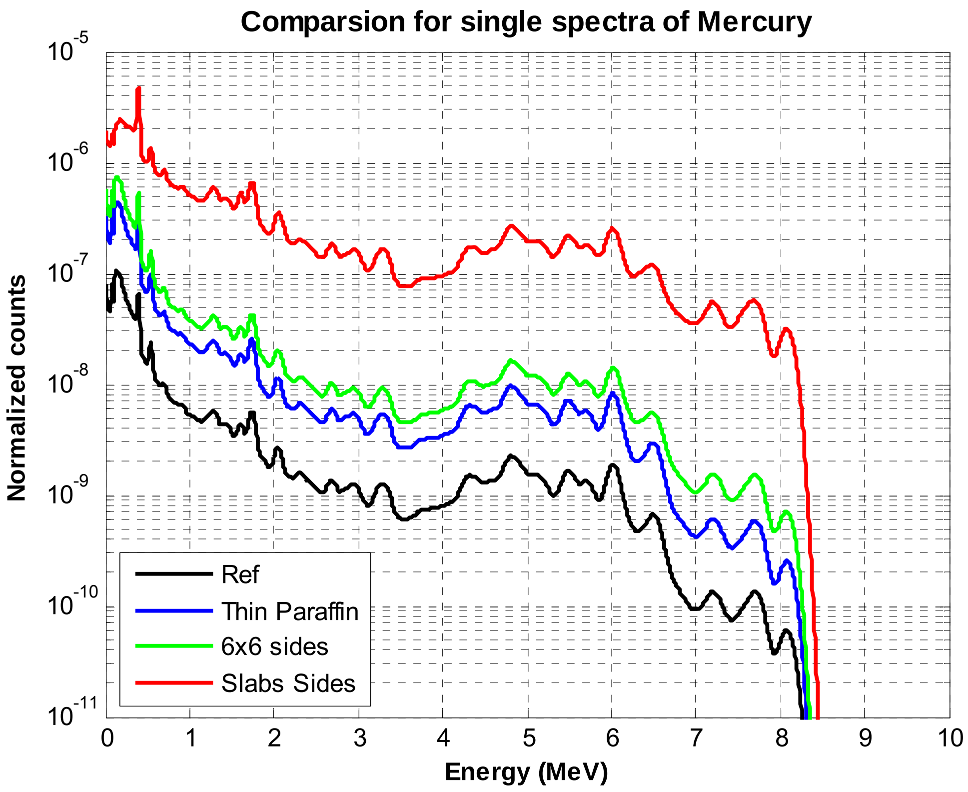

Figure 4-15 Comparison of single spectra of Mercury for lab sample

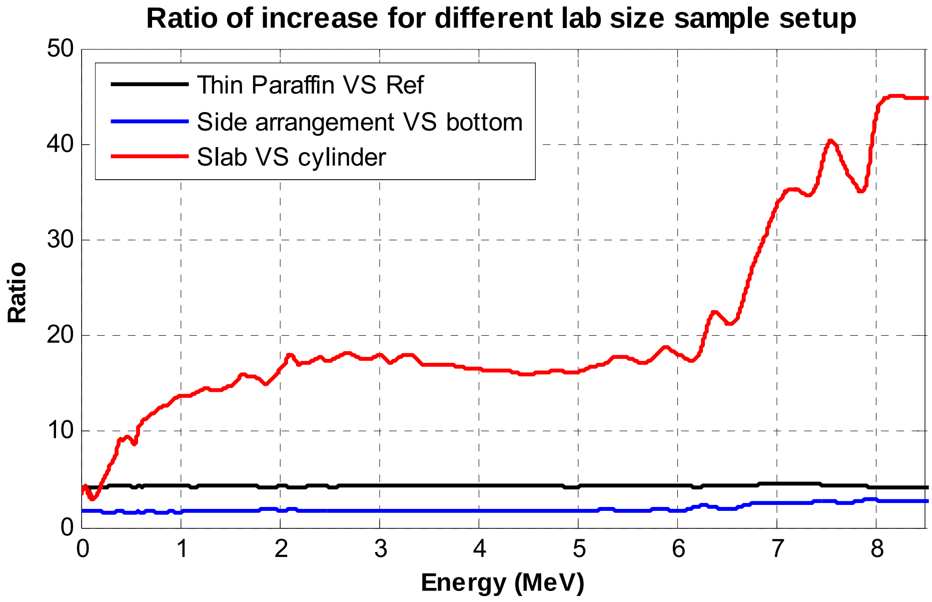

Figure 4-16 Ratio of increase in single response of Mercury for lab sample

It is also very interesting to look at the ratio of increase (ROI) for different setups as a function of energy. As examples, Figure 4-14 and 4-16 show the relationship between ROI and energy for sulfur and mercury, respectively. The black one represents the ratio of thin paraffin setup/reference setup, while the blue one represents left-right side arrangement/bottom arrangement for 6”x6” NaI detectors. As we expected, changing the paraffin moderator thickness or placing the same detectors at different locations should be energy independent, so the relationships are almost constant and agree well with the increase factor of overall single detector response. The most interesting one is the red curve, which represents the ROI between slab detectors and cylindrical detectors, both at left-right arrangement. Less than 2 MeV, the ratio has a positive relationship with energy; between 2 MeV and 6 MeV, the ratio is kind of constant value; between than 6 MeV and 8 MeV, the ratio continue to increase quickly as energy goes higher; higher than 8 MeV, the ratio stays at a constant value again. It is very promising to have an even higher improvement on high energy, as there are a lot of prompt gamma-rays in that region while fewer background can reach that high energy.

The possible explanation of this phenomenon is as follows. Two factors affect the ROI: the amount of particles that incident on the detector and the detector efficiency. As the geometry plot shown in figure 4-11 and 4-12, the cylindrical detector facing the sample with its front circle surface while the slab detector use the largest surface. Due to the bigger solid angle covering the sample, there are always more particles incident on the slab detector. The efficiency of both kinds of detector starts at similar value and decreases as the energy goes higher, and the efficiency of slab detector drops faster due to smaller thickness and volume. In lower energy region, both cylindrical and slab detector have good efficiency on gamma-rays. The increased detection of the slab detector mainly benefits from the larger covered solid angle which means more particles could incident on the detector. Also, the higher the energy, the possibility is higher that the particle could travel to the detector surface. The constant ROI in the middle energy range is the results of compromise between detector efficiency and amount of incident particle. The slab detector has a higher amount of incident particles while the cylindrical detector has a higher efficiency. In higher energy region, the slab detector could have a better efficiency when high energy particle incident on detector with certain angle because of the longer length of detector. Then the ROI continues to rise. In even higher energy range, the efficiency of both kinds of detector is at a low level and the solid angle effect dominates the ROI, which reaches a constant value again.

As for the coincidence detection, the simulation results of CEARCPG have also been compared for different setups. The total coincidence detector response is plotted in figure 4-17. Comparing with the reference setup, replacing the paraffin moderator with an optimized thickness will increase the coincidence detector response about a factor of 3.4 (blue versus black in the two figures). Changing the 6”x6” detectors position from bottom to left-right sides can further increase the overall detector response another factor around 3.8. Finally, using the 16”x4”x2” slab detectors at the left-right sides position to replace the 6”x6” cylindrical NaI detectors can gain another increase of a factor around 17.2 in the overall detector response. In sum, the slab detector left-right arrangement can detect around 223 times more coincidence gamma-ray detector response than the reference setup. That's a huge improvement in detecting coincidence signal.

Table 4-2 Ratio of increase for both single and coincidence detection of lab sample

	ROI* in Single response	ROI in Coincidence response	Relative ROI
Thin wax	4.3	3.4	0.79
Side Cylinder	6.9	13.0	1.88
Side Slab	66.5	223.7	3.36

* All ROI values are calculated based on reference setup in figure 4-1

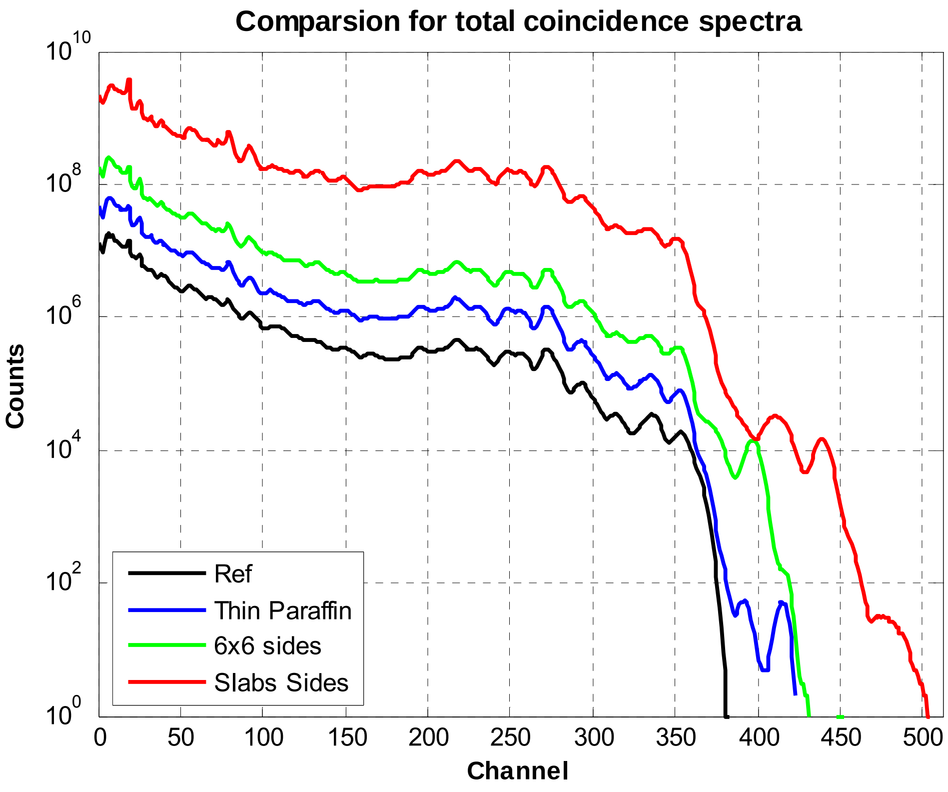

Figure 4-17 Comparison for total coincidence spectra of lab sample setups

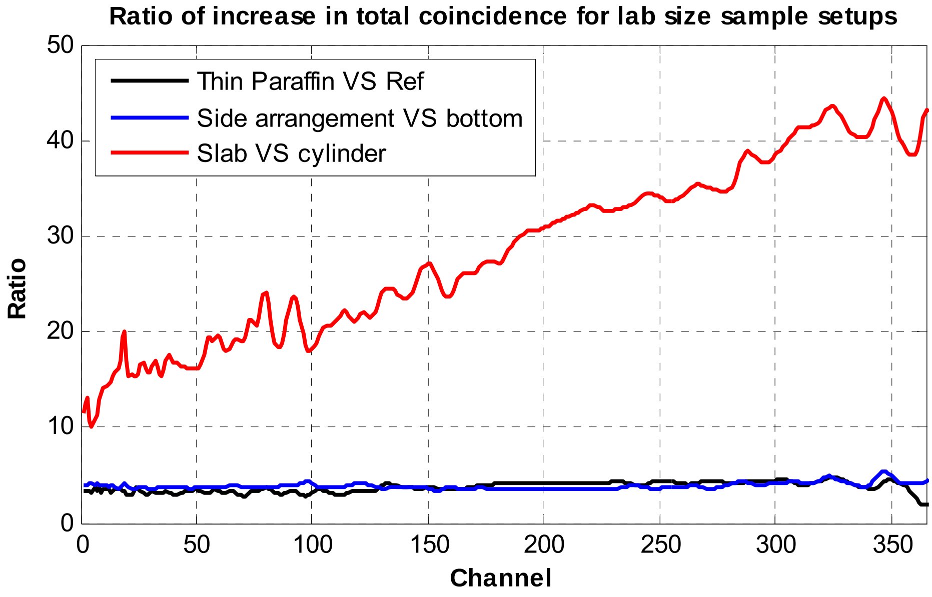

Figure 4-18 Ratio of increase in total coincidence for different lab size sample setup

The ROI plot as a function of energy (represents by channels in figure 4-18) shows the simiar trend as it on single detector response. Changing the paraffin moderator thickness and moving the 6”x6” detectors positions from bottom to left-right sides are energy independent, while changing the detectors from cylindrical to rectangular has a higher ROI at higher energy. That is a good feature as there are a lot of prompt gamma-rays in high energy region while fewer backgrounds can reach that high energy. The more improvements in coincidence response can help in elemental analysis.

Table 4-2 summarizes the ROI comparing to the reference setup. The relative ROI in the table is to show the improvement of coincidence response over single response of the same setup. It equals the ROI in coincidence response divided by the ROI in single response. Generally, the coincidence signal is two orders of magnitude lower than the single signal. With the slab detectors left-right arrangements, the coincidence response could be further improved by a factor of 3.36 over the increased single response.

4.3.2 Large Sample

The large sample that investigated here is 100 cm x 100 cm x 25 cm, which is a representative of the bulk coal sample on conveyor belt. No moderator is used to thermalize neutron as the self moderation is enough as shown in previous section. Also, as shown in the previous simulation of neutron and prompt gamma-rays distribution in and around the bulk sample, the ^{252}Cf neutron source is placed on top side of the sample and facing the center. The source is still placed in 5cmX5cmX5cm lead shielding box to shield the spontaneous fission gamma. As for the detectors, left-right sides of the sample are not suitable for placements according to the prompt gamma-ray distribution map, neither top-bottom placement due to space limit. Thus, both detectors are side by side placed in the opposite side of the neutron source. The same as for lab size sample, two kinds of NaI detector (6”x6” cylinder and 16”x4”x2” slab) are investigated. The setup with two 6”x6” NaI detectors is plotted in figure 4-19. It is very similar to the reference setup in figure 4-1. Figure 4-20 shows the setup for two slab NaI detectors.

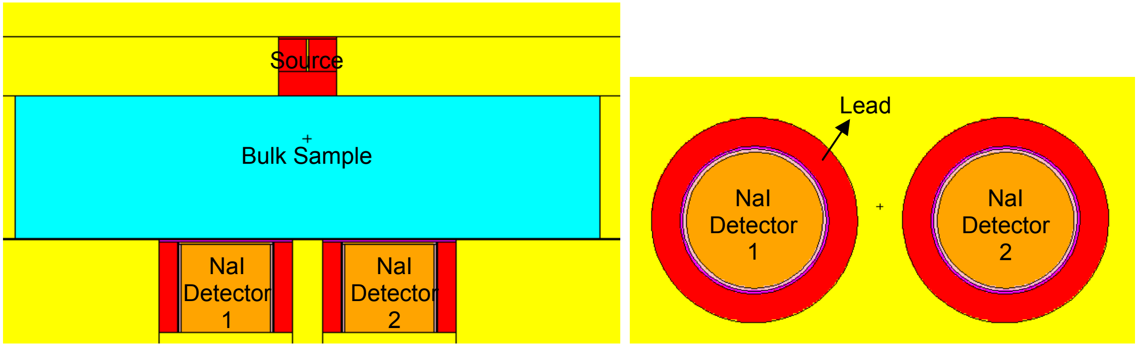

Figure 4-19 6”x6” cylindrical NaI detectors arrangement for large sample

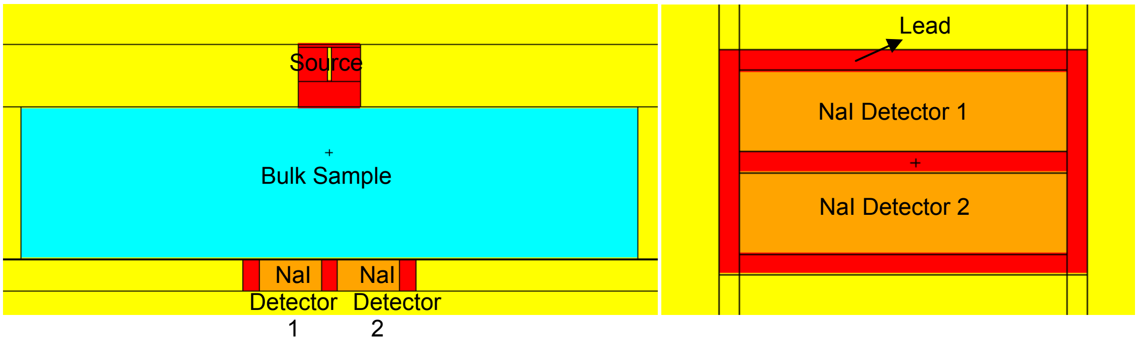

Figure 4-20 Slab NaI detectors arrangement for large sample

The 6”x6” cylinder detector setup is naturally chosen as the reference setup here. The two setups are compared according to the simulation of CEARCPG, for both the single detector response and coincidence detector response. The results are shown in table 4-3 and figure 4-21 to 4-26. Changing the detectors from 6”x6” cylindrical NaI to 16”x4”x2” slab could increase the single detector response by a factor of 1.6 and increase the coincidence detector response by a factor of 6.2. From the ROI plots, it could be found that the ROI in single response is basically insensitive to energy. It is slightly higher when energy above 6 MeV. The ROI in coincidence response is more sensitive to energy with higher value in higher energy region, which could benefit the coincidence PGNAA detection.

The sample size influence is also investigated. The arrangements of 6”x6” cylinder detectors under the sample are compared as they have almost the same source and detectors. The only difference is the sample size and a 7.3cm paraffin moderator used for lab size sample to thermalize ^{252}Cf neutron source. It turns out that the single response is 2.58 times higher for large sample while the coincidence response is about 2.39 times higher.

Another setup with plastic detector will be discussed in next section.

Table 4-3 Ratio of increase for both single and coincidence detection of large sample

	ROI* in Single response	ROI in Coincidence response	Relative ROI	ROI in Coincidence Events
Side Slab	1.6	6.2	3.8	9.7
Plastic with NaI arrangement	2.5	1.7	0.68	8.0

* All ROI values are calculated based on setup in figure 4-19

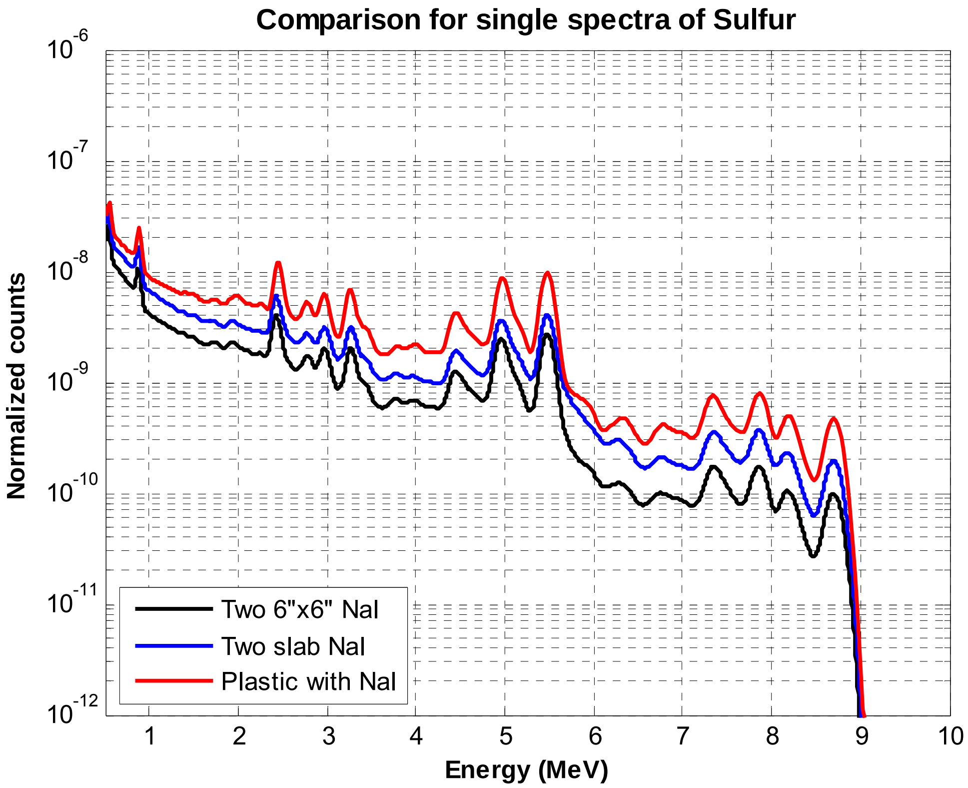

Figure 4-21 Comparison for single spectra of Sulfur for large sample

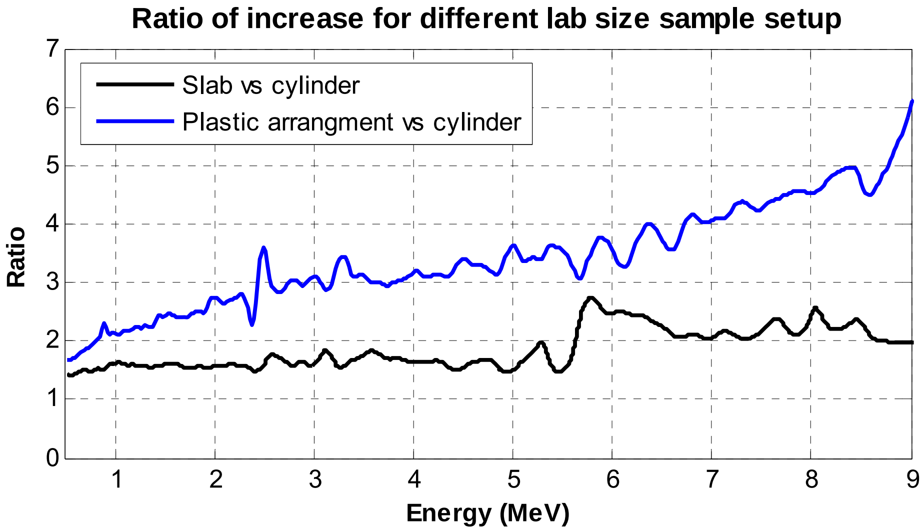

Figure 4-22 Ratio of increase in single response of Sulfur for large sample

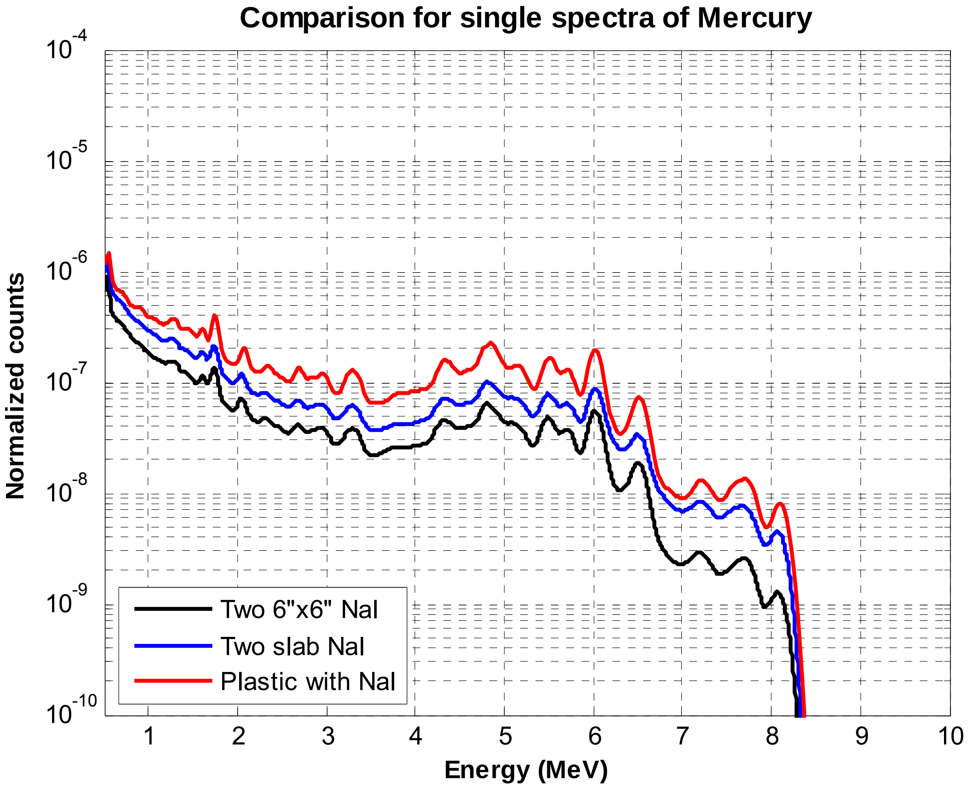

Figure 4-23 Comparison for single spectra of Mercury for large sample

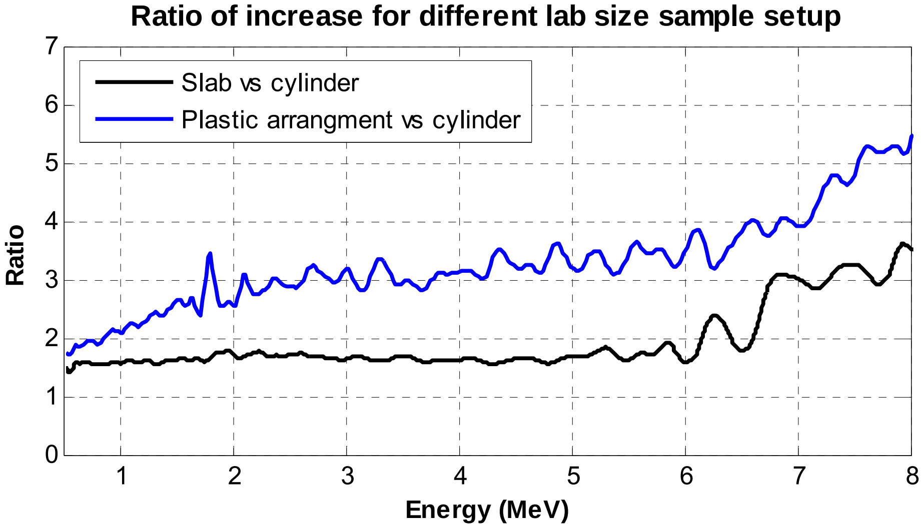

Figure 4-24 Ratio of increase in single response of Mercury for large sample

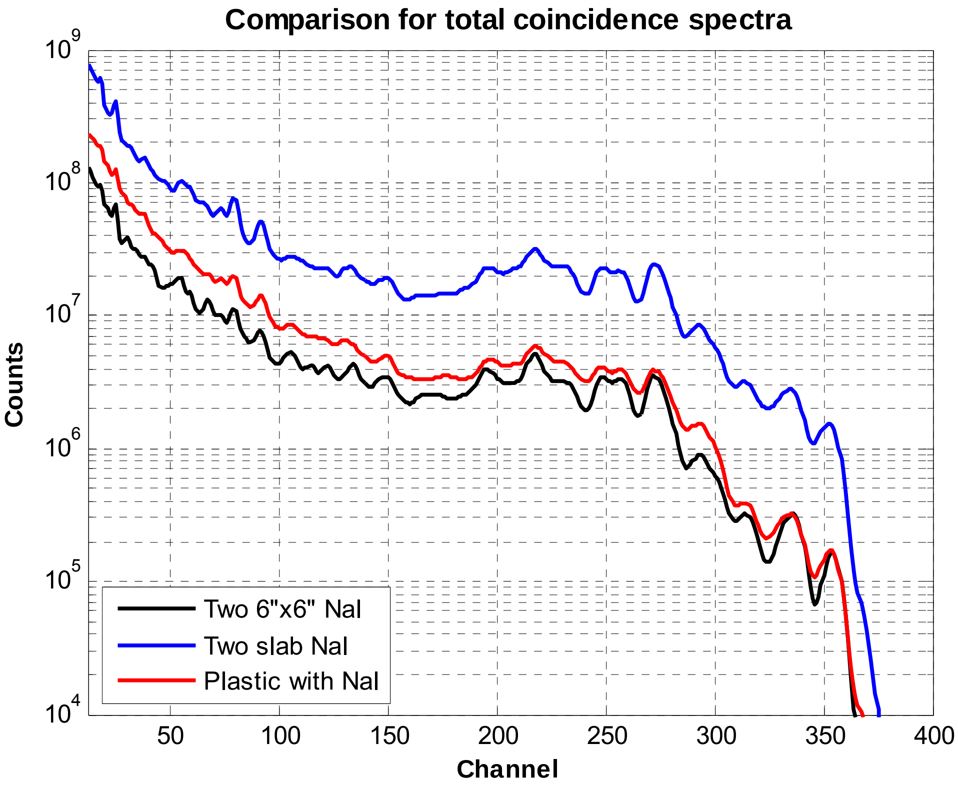

Figure 4-25 Comparison for total coincidence spectra for large sample

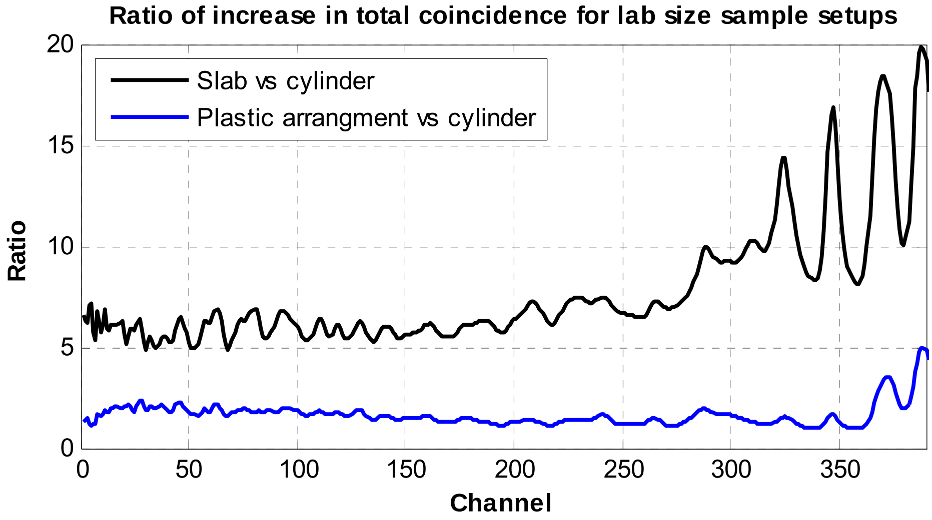

Figure 4-26 Ratio of increase in total coincidence for large sample

4.4 Detector

NaI(Tl) scintillation detector, which was demonstrated by Robert Hofstadter in 1948 (Hofstadter, 1948), is the commonly used detector not only in commercial PGNAA analyzer, but also as the standard scintillation material for routine gamma-ray spectroscopy. It has good energy resolution (~7% at 0.662MeV) and time resolution. The most notable property of NaI is its excellent light yield. In those previous sections, we investigated the optimization of coincidence PGNAA using NaI detector only.

Bismuth germanate (BGO, $Bi_4Ge_3O_{12}$) detector is another popular scintillator that used in gamma-ray spectroscopy. The major advantage over NaI is its higher density ($7.13 g/cm^3$) and the large atomic number (83). However, the light yield from BGO is relatively low, being variously reported at 10-20% of that of NaI. Also, the time resolution is about a factor of two worse than that for NaI (Knoll, 2000). Thus, BGO is not very suitable to the coincidence PGNAA application.

Although plastic organic scintillation detector has a very bad energy resolution (figure 4-27), its superior time resolution (0.9ns rising time and 2.1ns decay time) and relatively inexpensive price make it a potential good choice. It can also be tailored to a wide variety of sizes and shapes easily. Some simulation works with MCNP5 have been done to better understand plastic detector in PGNAA application, as shown in later sections. There is also a detailed comparison between NaI and plastic detector for vehicle portal monitoring in Siciliano's work (Siciliano et al., 2005).

NaI(Tl) scintillation detector and plastic detector are the two major detectors investigated in this work. For NaI versus NaI detectors arrangements, the principle has been validated in previous works (Han, 2005, Metwally, 2004; Gardner, 2000). For NaI versus plastic detectors arrangements, it is to use the plastic detector as a "trigger" of coincidence event. The plastic detector will cover as big solid angle as possible to increase the possibility of coincidence detection.

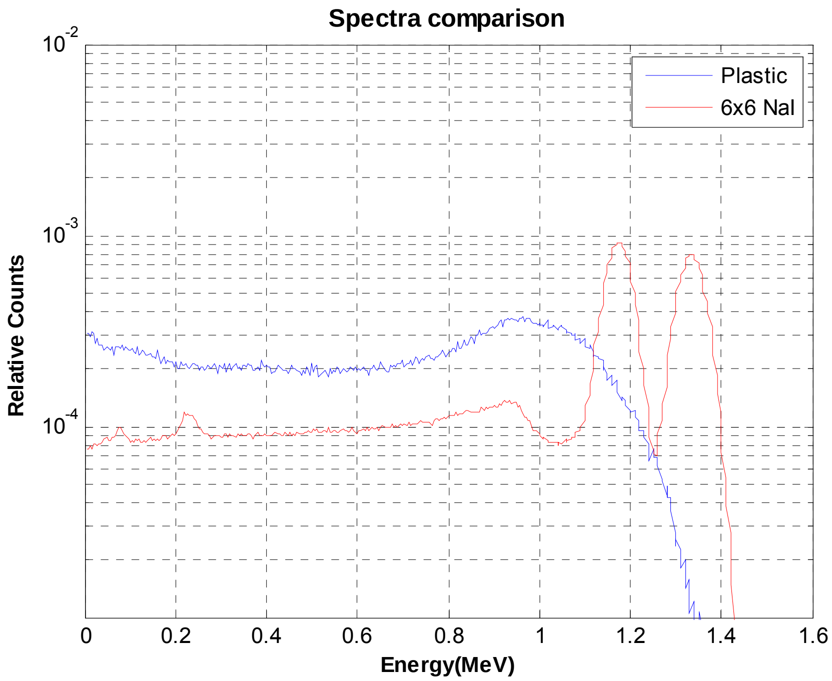

Figure 4-27 Co60 spectra of NaI detector and Plastic detector

4.4.1 Cross Section

The drawback of plastic scintillation detector is that the main component of its spectrum is Compton continuum only. And it is generally used as a counter, not for spectroscopy. The reason is that Compton scattering dominates photon reaction from 20 KeV, which is 250 KeV for NaI detector as shown in figure 4-28. However, since we are using in coincidence application, we could project the 2D coincidence spectrum to the NaI axis to overcome this drawback and utilize its advantages.

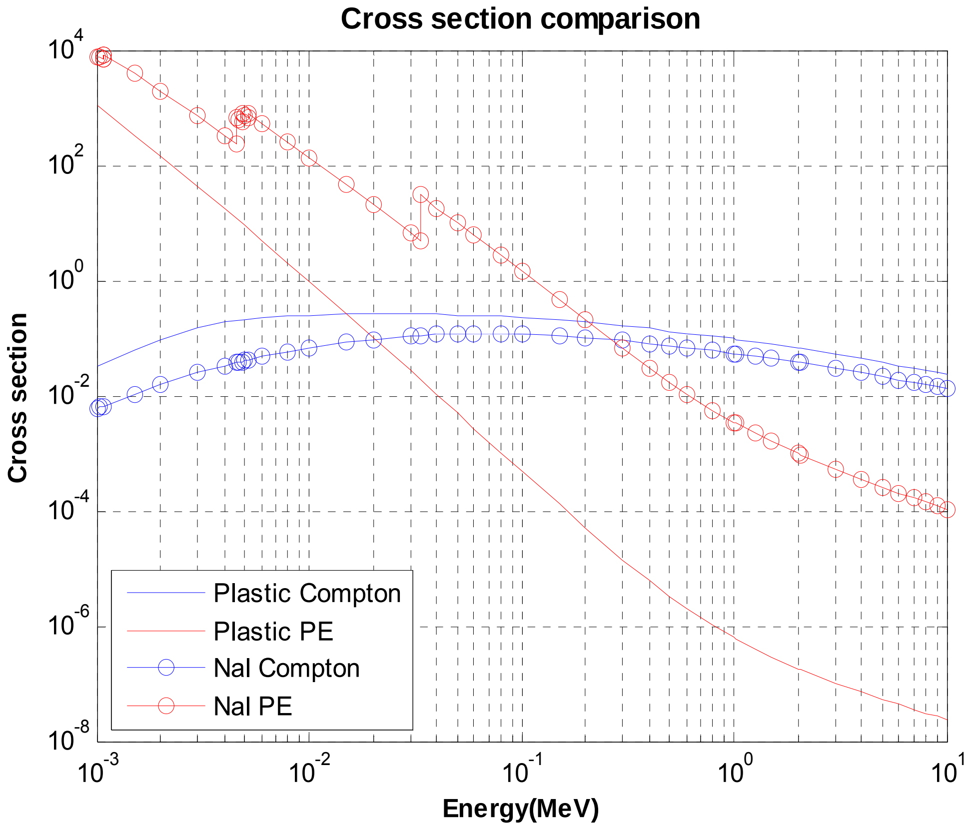

Figure 4-28 Cross section comparison between NaI and Plastic detector

4.4.2 Detector Efficiency

MCNP5 has been used to investigate the absolute efficiency. A source is placed 10 cm away from the front surface for 6”x6” cylindrical NaI detector and the center of largest surface of rectangular plastic detector. According to simulation results, a 70x50x10cm plastic scintillation detector could provide about 3 times better absolute efficiency than a 6x6in NaI detector in the energy range of 0 to

10MeV (figure 4-29). Due to its low density and small atomic number, the efficiency for higher energy drops. Increase the plastic detector thickness will improve the efficiency of high energy as shown in the bottom plot of figure 4-29

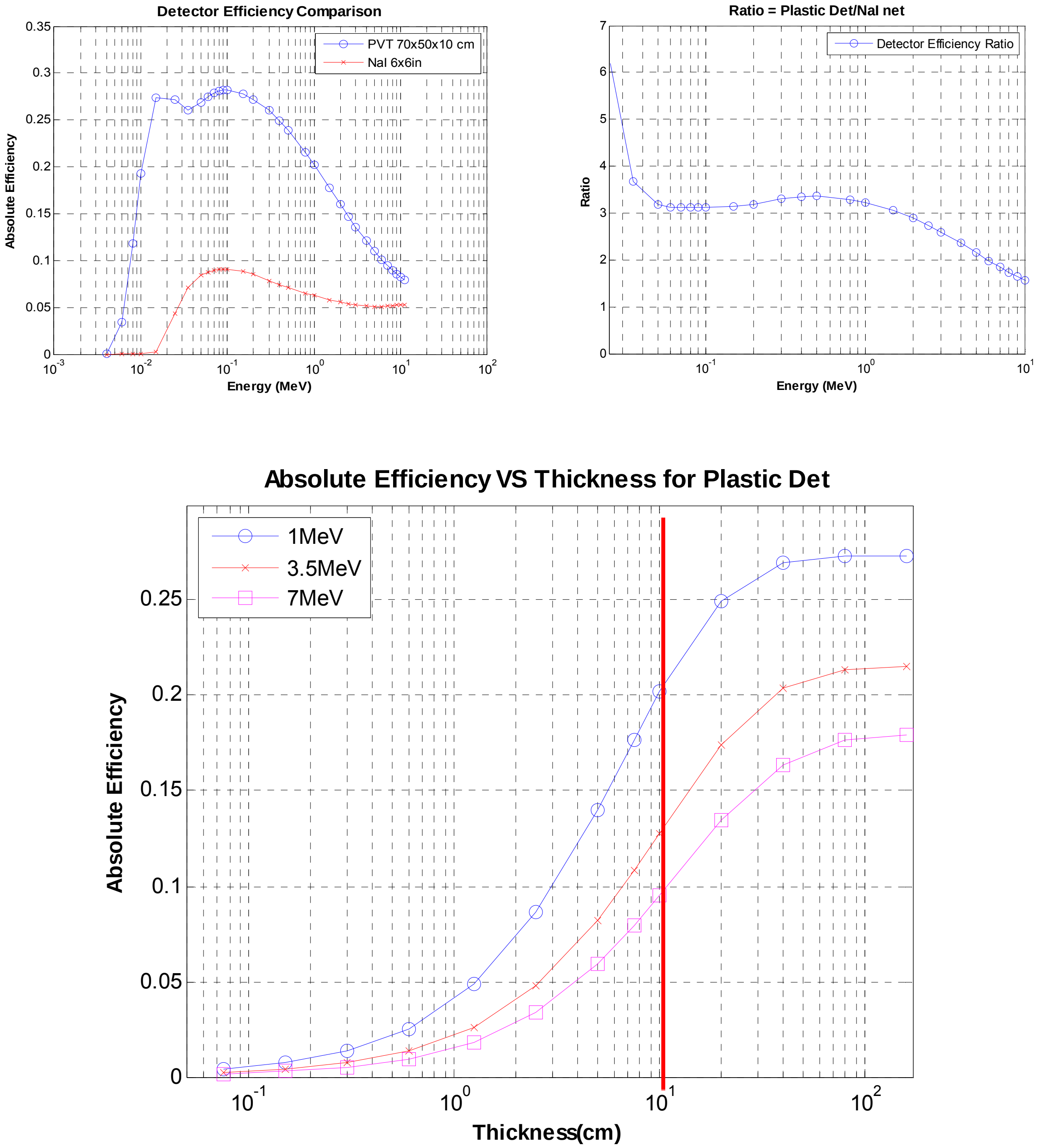

Figure 4-29 Detector efficiency of 6"x6" NaI detector and Plastic detector

4.4.3 Neutron Response

As an organic detector, the main compositions of plastic scintillation detector are hydrogen and carbon. Thus there is a concern about the plastic detector's neutron response. The major interaction contributing to neutron detection of plastic detector is neutron elastic scattering reaction of light nuclei, hydrogen and carbon.

In this interaction, the neutron is scattering to a different direction and transfer a portion of its energy to the recoil nucleus, which is Hydrogen (proton) nucleus and carbon nucleus in this case. The range of recoil nucleus is usually very small (millimeters) comparing to detector size, so it will deposit its energy locally. The Q value of elastic scattering is zero because the total kinetic energy of the reaction products (recoil nucleus and the scattered neutron) is the same as the kinetic energy before. For single scattering in hydrogen, the fraction of the incoming neutron energy that is transferred to the recoil proton can range from zero to the full neutron energy, while it can range from zero to 78% of the full neutron energy for scattering in carbon (Knoll, 1999). Thus, the plastic detector will have certain response to fast neutron.

Some simulations using MCNP5 have been done to investigate the neutron flux and prompt gamma-ray flux in the 70cm x 50cm x 10cm plastic detector after various thickness of coal sample. The results are shown in figure 4-30 and 4-31. Because the light output of organic scintillators for electrons is always higher per unit energy than for charged particles (Knoll, 1999). Therefore, the neutron discrimination is easier because it may require a neutron with energy of 200 or 300 KeV to give the same light output as a 100 KeV gamma rays. Thus, a curve represents neutron with energy higher than 100 KeV is also plotted in these figures. It could be found that after 25 cm thick coal, which is the normal thickness of coal on conveyor belt, the gamma-rays flux inside the detector is 5 times higher than fast neutron flux. Other steps could also be done to decrease the neutron amount arrives the detector. For example, placing a paraffin or other moderator between the plastic detector and the coal sample, which could dramatically further thermalize the neutron without affecting the prompt gamma-rays much. A thin layer of Boron, or Lithium, or Gadolinium enriched material will further alleviate the need of discrimination. The most important, in coincidence application, the resolving time is around 20ns. Therefore, there is no true coincidence between neutron response and prompt gamma rays due to the speed difference of neutron (1.4×10^7 m/s at energy of 1MeV) and photon (3×10^8 m/s). Also, the coincidence due to neutron multiplicity could also be ignored according to Han's calculation (Han, 2005).

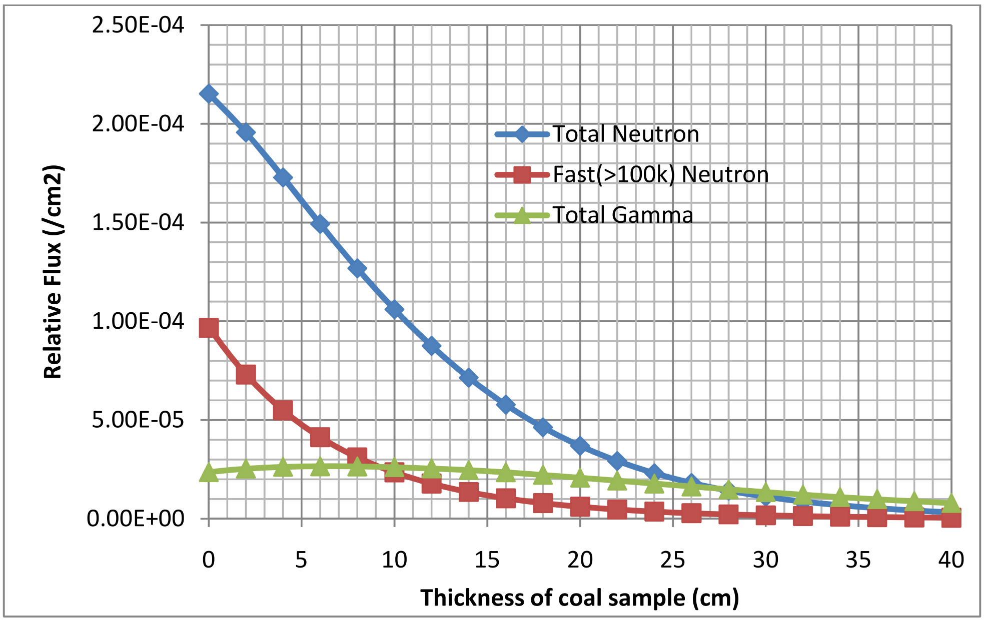

Figure 4-30 Neutron and prompt gamma flux inside detector as a function of coal thickness

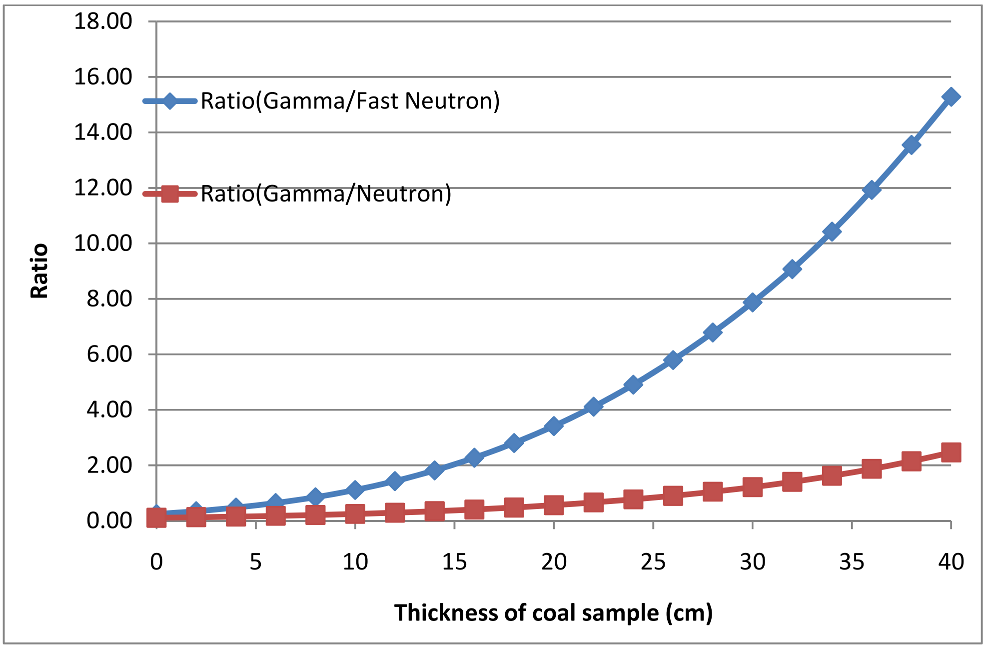

Figure 4-31 Gamma/Neutron ratio inside detector as a function of coal thickness

Thus, the effect of plastic detector neutron response is not a severe problem and can be eliminated with proper shielding and setup. It could also be found that a 10cm thick coal can give the maximum prompt gamma-rays output.

4.4.4 Plastic Detector Setup

According to the above investigation, the plastic detector might be suitable in prompt gamma-ray detection, especially as a trigger detector of the other NaI detector. Only the large sample that similar to conveyor belt size is investigated here to utilize the plastic detector's larger size. The proposed coincidence PGNAA setup for slab plastic detector and 6"x6" cylindrical NaI detector is shown in figure 4-32. The plastic detector is placed under the large coal sample. The ^{252}Cf neutron source is moved 10cm away from the center to give some space to the NaI detector on the same side. The NaI detector is surrounded with a 20cm thick paraffin ring, following be a 2.54cm thick lead ring and then a 0.5cm thick boron carbide. So both the neutron and photon directly from the ^{252}Cf are proper shielded.

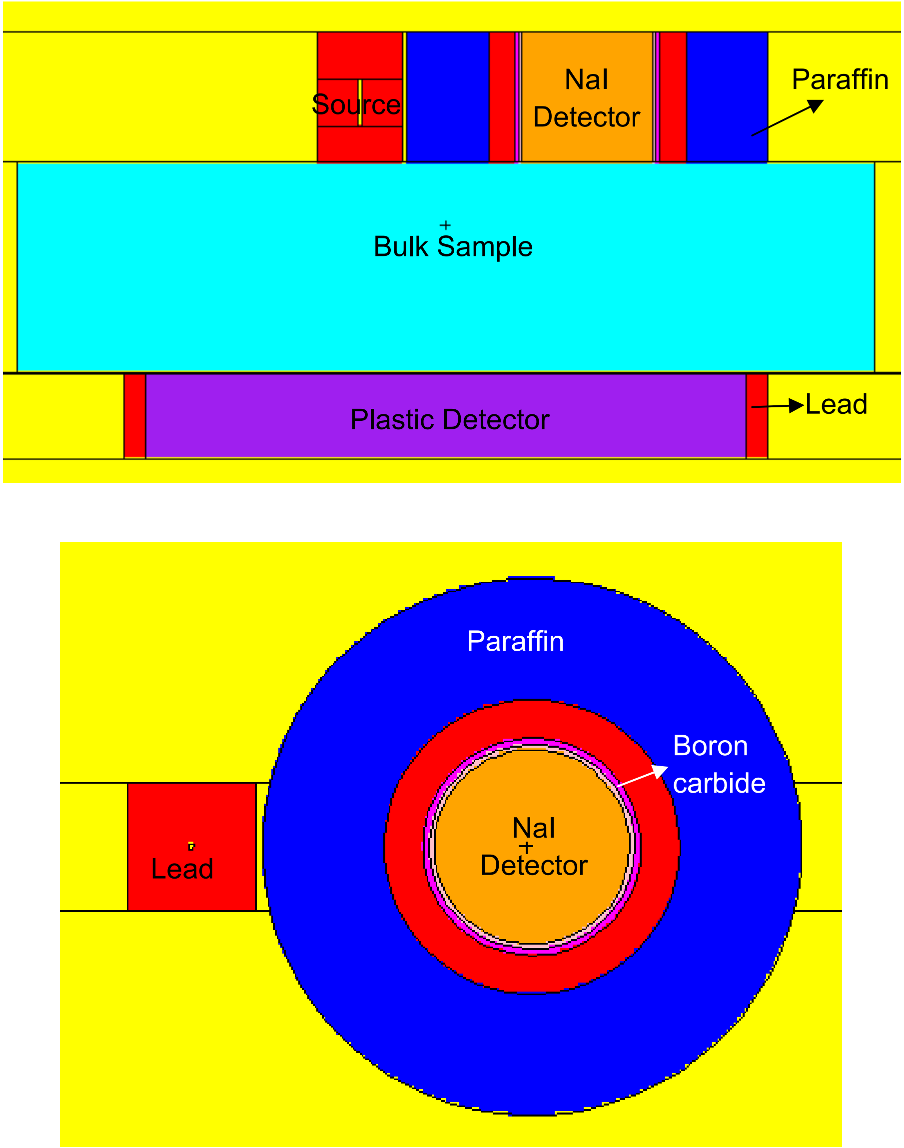

Figure 4-32 Slab plastic detector versus cylindrical NaI detector arrangement for large sample

The simulation results of the plastic/NaI detectors setup has already been shown in table 4-3 and figure 4-21 to 4-26 to compare with other two large sample setups. The single detector response is of the 6”x6” NaI detector as the plastic detector has been used as a trigger to coincidence events only. The plastic/NaI setup could increase the single detector response by a factor of 2.5 and increase the coincidence detector response by a factor of 1.7. The total coincidence spectrum plotted there is generated by projecting 2D spectrum to the axis representing NaI detector. From the ROI plots, it could be found that the ROI in single response is sensitive to energy with higher value in higher energy region. It is slightly higher when energy above 6 MeV. The ROI in coincidence response is basically insensitive to energy. There is also a slight drop of ROI in high energy region. The reason of that is the low efficiency of the slab plastic detector for high energy gamma due to low density and low atomic number. The different behavior of ROI as a function of energy explains why the ROI in coincidence response is lower than single response.

Comparing the slab NaI/NaI detectors setup and plastic/NaI setup, the first one has a higher coincidence response while the other one has a higher single response. So, it is a trade-off when choosing one of them. But the ROI in coincidence events shows this setup has the potential to achieve the similar coincidence response by increasing the detector thickness to improve efficiency. Another phenomenon should be mentioned is the higher response from the NaI detector that at the same side of neutron source. The difference is the results of more prompt gamma-rays generated from the top part of the coal, as more neutron interactions happen there.

5 MONTE CARLO SIMULATION RESULTS

In the previous chapter, a lot of details related to the PGNAA analyzer have been discussed. Here in this chapter, the simulation results of CEARCPG of picked preliminary setups will be shown and discussed.

5.1 Preliminary Setups and Results

For the lab size small sample, the setup of two slab NaI detectors lying left-right with neutron source on top (figure 4-12) has the best response for both single detection and coincidence detection, so the results of this setup is shown here. For the large size sample similar to conveyor belt case, the setups of figure 4-20 and 4-32 are both examined here. One utilizes the same two slab NaI detectors lying side by side under the coal sample with neutron source on top. The other comes with a large plastic detector lying under the sample with neutron source on top. The cylindrical NaI detector is placed besides the neutron source with proper shielding.

Through CEARCPG, the 2D coincidence spectrum of these setups has been simulated with a coal sample (H-2.892%, C-5.28%, N-%1.4, O-5.487%, Na-1.121%, Al-2.38%, Si-1.943%, S-5.6%, Cl-1.729, Hg-2.168%). Figure 5-1 and 5-2 show the simulated 2D total coincidence spectra of the three setups for the above coal sample. The lower and upper limits of display range (from light to dark) are noted in brackets.

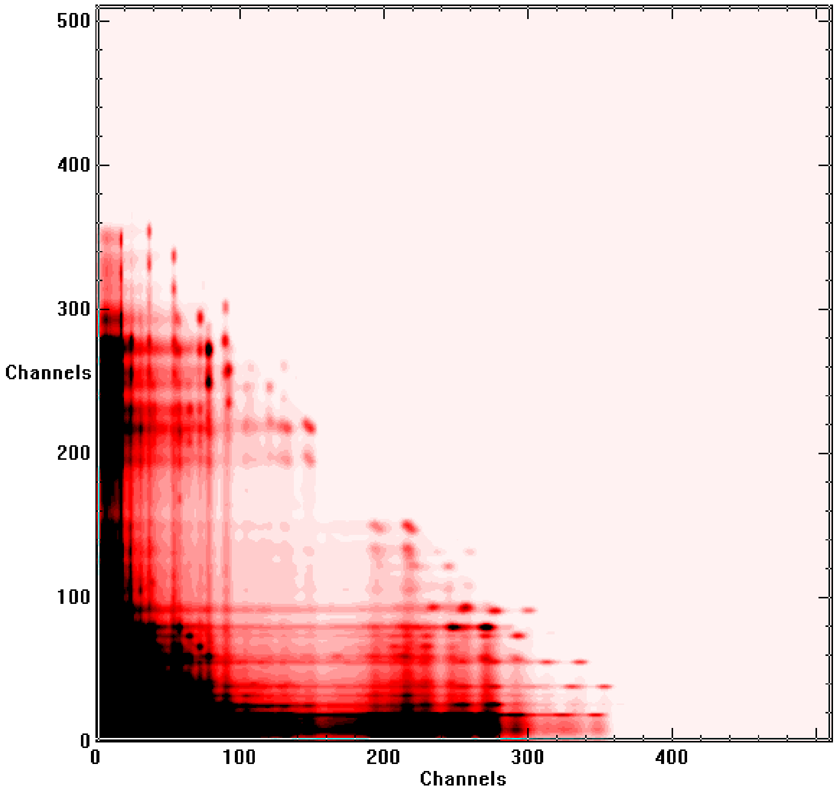

Figure 5-1 2D total coincidence spectrum of slab NaI/ NaI setup for lab sample (0-2000000 counts)

The most obvious feature in the 2D coincidence spectra is the symmetric structure along the diagonal line from bottom-left to top-right. The dots in the 2D spectra are the coincidence peaks and the stripes are coincidence between peaks and Compton continuum. Due to the peak standard deviation difference between low and higher energy peaks, the dots shapes are close to ellipse when deviates from the diagonal line. If there is any cross talk between detectors, which means one particle deposits partial energy in one detector and then escapes to the other detector and deposits energy there, the feature would be strips that parallel to the diagonal line from bottom-right to top-left. Apparently, the cross talk could be ignored here due to the lead shielding between detectors.

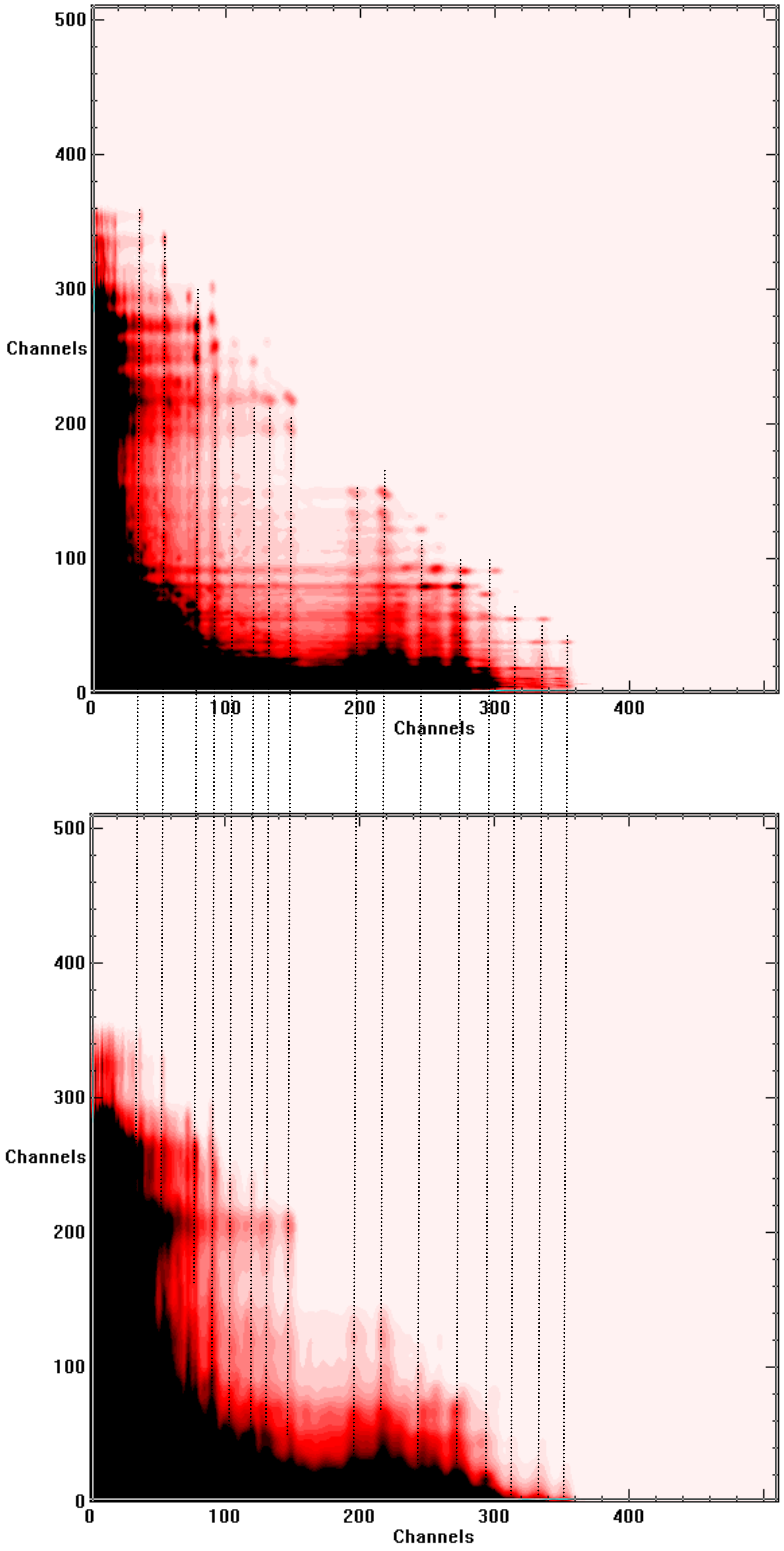

Figure 5-2 2D total coincidence spectrum for lab coal sample
Slab NaI/NaI setup (top, 0-200000 counts) and plastic/NaI(bottom, 0-30000 counts)

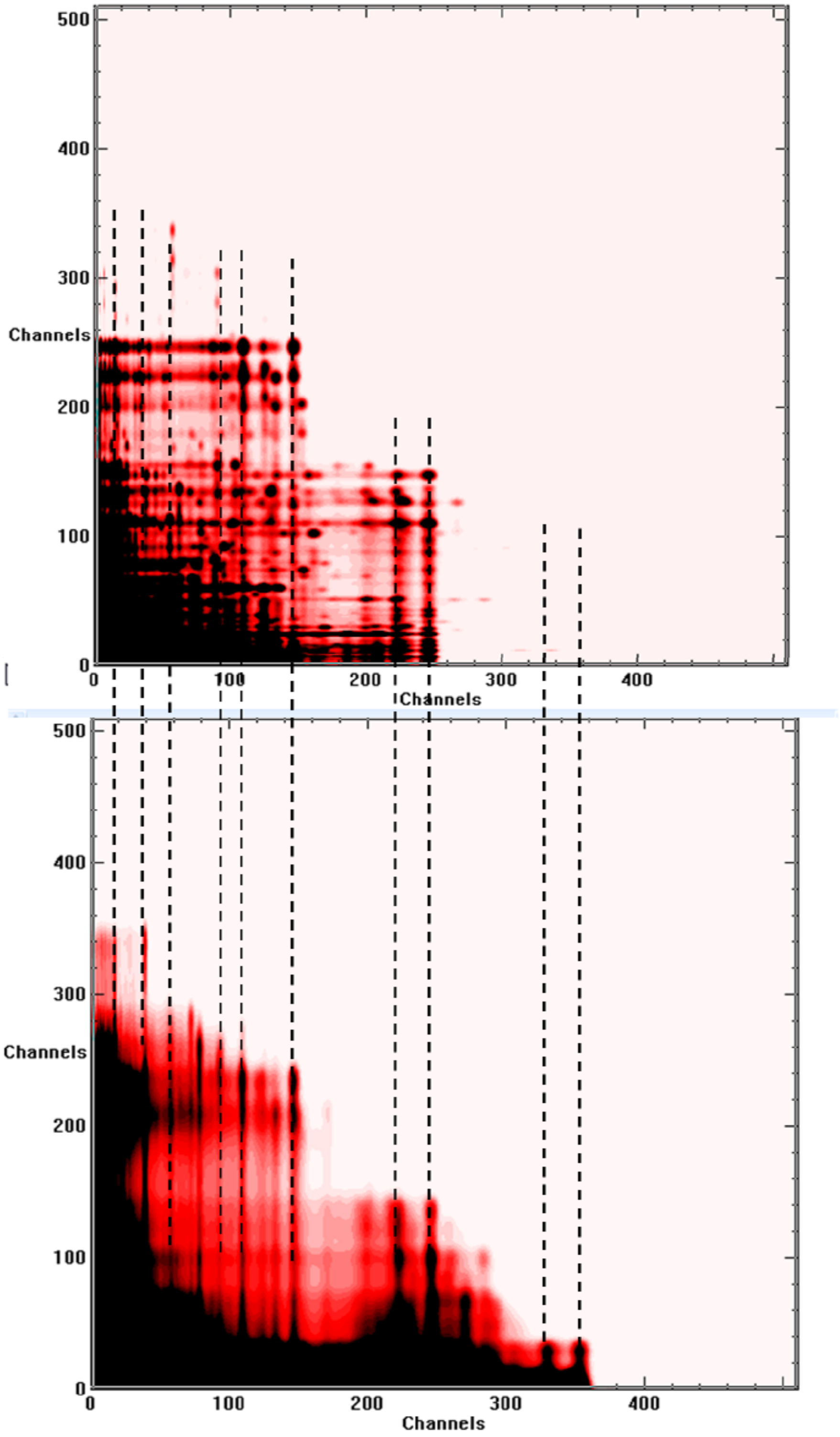

Figure 5-3 2D total coincidence spectrum for lab sulfur/mercury sample

Figure 5-2 shows the simulated 2D coincidence spectra of slab NaI to NaI coincidence setup (top) and the plastic to NaI coincidence setup (bottom) for large coal sample. The new coincidence spectrum is not symmetric as the old one due to poor detector resolution and the no-peak property of plastic scintillation detector. On the axis representing plastic detector, the features are not clear. However, the axis representing NaI detector still keeps the good energy resolution. After projecting the 2D spectrum to the axis representing NaI, we could get the traditional total coincidence spectrum as the red curve in figure 4-25.

It is not easy to identify the peaks by naked eyes for the coal sample that simulated, because there are too many prompt gamma-rays and some of them are at close channels. A sample contains sulfur and very little mercury was also simulated (2D coincidence spectra shown in figure 5-3). After projected to NaI axis, the peaks (table 5-1) are very clear in figure 5-4.

Table 5-1 Peaks in the total coincidence spectrum of Sulfur sample (little mercury inside)

Peak	Energy(MeV)	Source
1	0.511	Pair Production
2	0.841	Sulfur
3	2.379	Sulfur
4	2.931	Sulfur
5	3.22	Sulfur
6	4.4308	Sulfur
7	4.869	Sulfur
8	5.4205	Sulfur
9	7.31	Hg
10	7.8	Sulfur
11	0.367	Hg
12	6.457	Hg

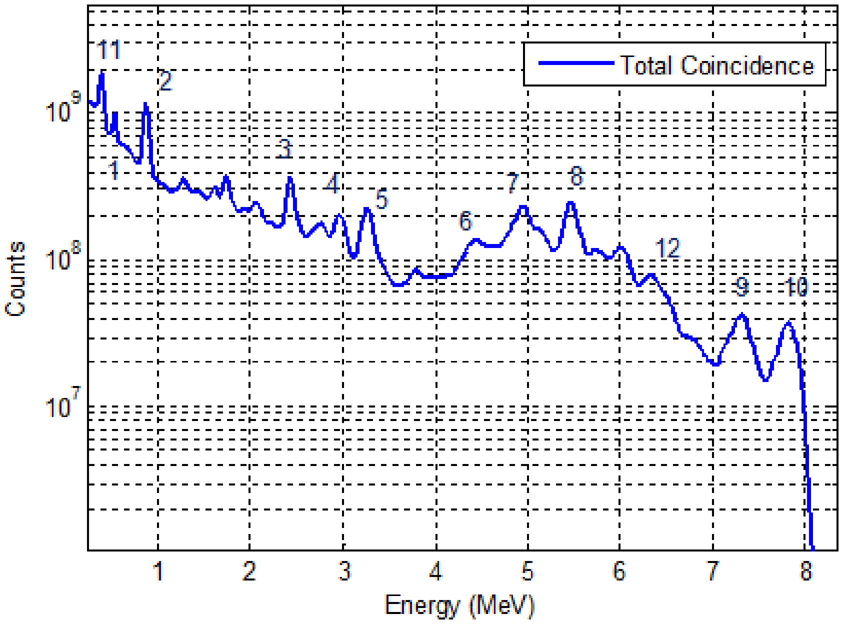

Figure 5-4 2D spectrum's projection on NaI detector axis for sulfur sample (little murcury)

CEARCPG can also generate the library coincidence spectra. These 2D coincidence spectra from each element in a typical coal sample with all common elements in coal could be found in Appendix D.

5.2 Interferences Analysis

PGNAA has relatively complicated gamma spectra, including the interference from the neutron source, the structure materials, and interferences from the natural background and pulse summing effect (Metwally, 2004). The common interferences are listed as follows:

1. Fission gamma rays emitted from the neutron source(for example: ^{252}Cf spontaneous neutron source)

2. Gamma rays produced by neutron interaction with the materials of detector. (Gardner, 2000). For NaI detector, it includes the prompt gamma rays of NaI and the decay gamma rays of radioisotopes ^{128}I and ^{24}Na.
3. Gamma rays produced by the construction materials of PGNAA analyzer
4. Natural backgrounds, including Potassium-40 which emits the gamma rays with energy 1.461 MeV, Uranium and Thorium decay chain which emits gamma rays with energy 1.764 MeV, 2.204 MeV, 2.614 MeV etc.
5. Cosmic radiation which will generate high-energy continuous distribution gamma rays.

It is well known that the gamma-gamma coincidence technique can reduce the interference from background, pulse-pile effect, the summing effect, and improve the signal-to-noise ratio. However, there are still some true coincidence exist that will interfere the coincidence PGNAA. Plus, the chance coincidence problem arises when the counting rate is high.

5.2.1 Fission Gamma

According to the evaluation by Timothy E. Valentine (2001), the average number of prompt fission gamma rays from spontaneous fission ^{252}Cf estimate to be 7.99±0.63 per spontaneous fission and the multiplicity distribution of gamma rays from fission is plotted in figure 5-5. The gamma-ray energy spectrum are plotted in the following figure 5-6 measured by V.V. Verbinski(1973).

Due to multiplicity of the prompt fission gamma rays for spontaneous fission ^{252}Cf source, there are usually more than one fission gamma-rays emitted from the source. If both detectors detect more than one of these fission gamma-rays, they will contribute to the true coincidence response.

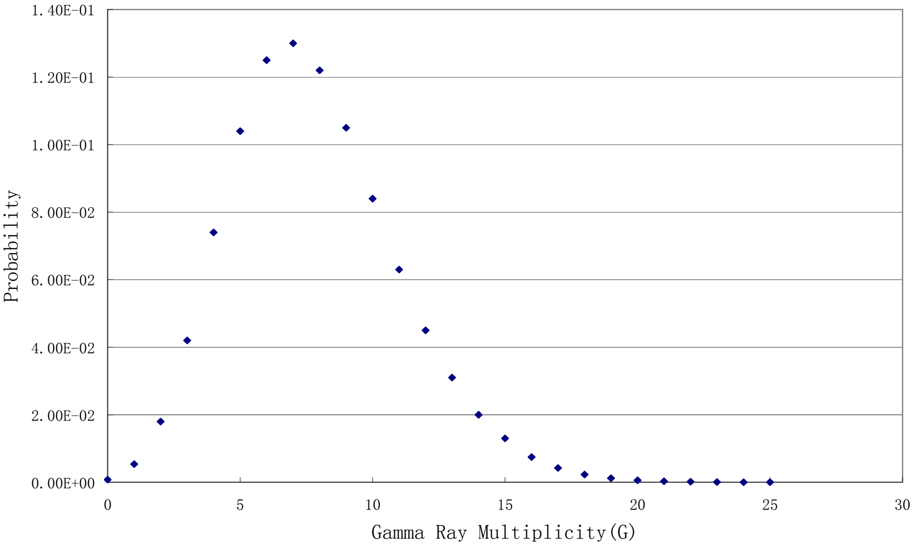

Figure 5-5 The gamma ray multiplicity of ^{252}Cf neutron source

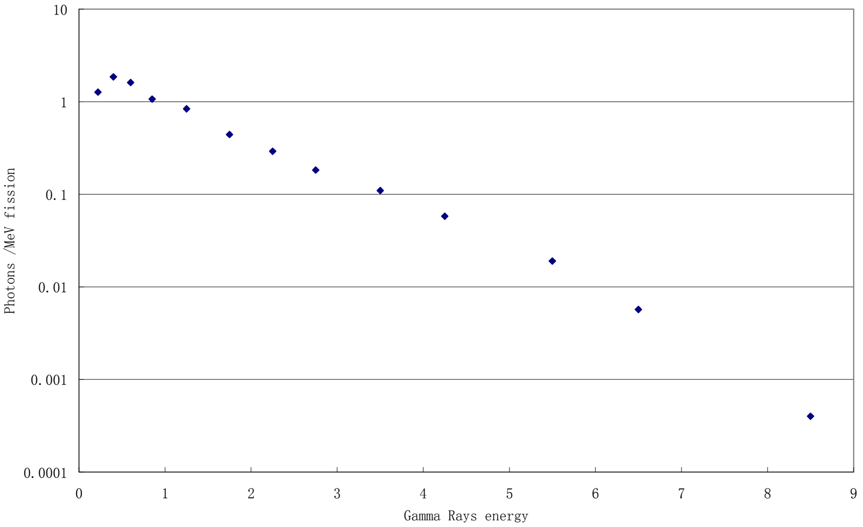

Figure 5-6 The energy distribution of fission gamma-rays of ^{252}Cf neutron source

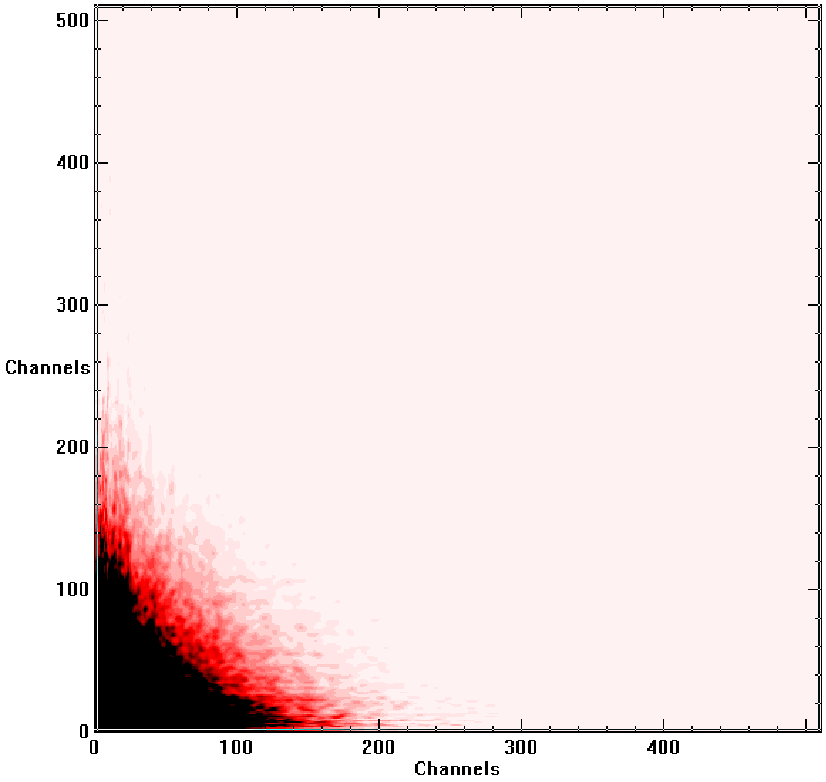

Figure 5-7 Simulated 2D coincidence spectra of fission gamma-rays (0-300000 counts)

CEARCPG has the capability to simulate the single and coincidence response of fission gamma from spontaneous fission ^{252}Cf following the multiplicity distribution and energy distribution of fission gamma-rays. Figure 5-3 shows an example of CEARCPG simulated 2D coincidence spectrum of fission gamma-rays from spontaneous fission ^{252}Cf for setup in figure 4-12 (two slab NaI detector for lab sample). There are not many features on the 2D coincidence spectra of fission gamma. Similar to the energy distribution, the bottom-left corner has the most counts, which means low energy fission gamma to low energy fission gamma coincidence has the highest possibility. Although there are a 5cm x 5cm x5 cm lead block, there is still a fairly large amount of fission gamma-rays incident on both detectors for the lab sample setup. For the large sample setup, it is harder for the fission gamma-rays to travel through the sample and incident on the detectors. Overall speaking, the fission gamma is the most important interference in coincidence PGNAA.

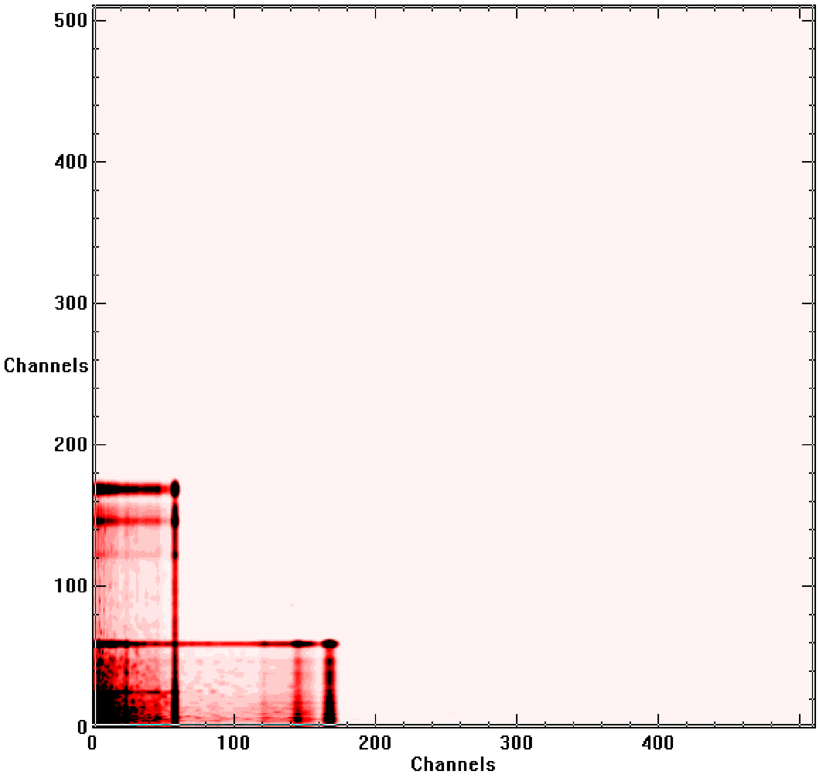

Figure 5-8 Simulated 2D coincidence spectra of gammas from structural materials (0-30000 counts)

5.2.2 Structure Materiel

The composition of structure materials in PGNAA setup could be complicated. Most possible elements in the structure materials are hydrogen, carbon and some metals. Coincidence prompt gamma-rays could be from carbon or metals. In our simulation, only carbon and lead in the surrounding structure materiel could contribute to true coincidence response. The CEARCPG simulated 2D coincidence spectrum of prompt gamma-rays from structure materials is plotted in figure 5-8. The features in that figure mainly come from carbon in the moderator and plastic box holding the sample.

Both the fission gamma coincidence and structure materials coincidence are true coincidence. However, in coincidence application, the amounts of them are low comparing to the prompt gamma-rays from the sample. Also, with MCLLS application, both of them could serve as libraries to include their effects in consideration.

5.2.3 Chance Coincidence

Another important factor to be considered is the chance coincidence. Everything source of gamma-rays could be included in the total coincidence response through chance coincidence. The chance coincidence cannot be simulated by CEARCPG directly at present. However, the chance coincidence spectrum can be easily estimated with the experimental spectra by using the following equation,

$$R_c = R_1 \cdot R_2 \cdot \tau \qquad (5\text{-}1)$$

where R_1 is the counting rate of detector 1 and R_2 is the counting rate of detector 2. τ is the resolving time of coincidence measurement. Figure 5-9 shows the calculated two-dimensional chance coincidence.

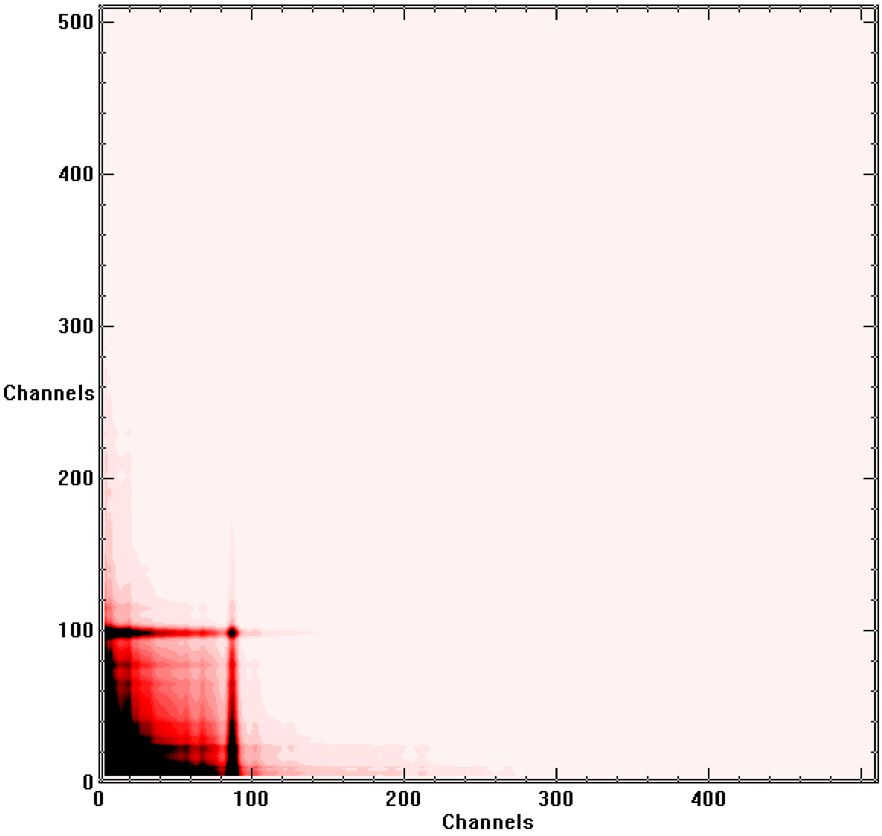

Figure 5-9 The Calculated chance coincidence spectrum

From the equation, it could be found that the chance coincidence is highly related with the single detector counting rate. For example, the resolving time of our current coincidence is around 20ns. When the $R_1 = R_2 = 10^4 / s$, we have $R_c = 10^4 / s \times 10^4 / s \times 20 \times 10^{-8} s = 2 / s$. The normal estimation of true coincidence rate is two order of magnitude lower than single counting rate, which is 10^2/s. The chance coincidence counting rate is only 2% of the true coincidence rate. However, when the single detector counting rate increases to 10^5/s the chance coincidence counting rate is 20% of the true coincidence rate, which cannot be ignored then. If the single counting rate continues to increase to 10^6/s, the chance coincidence counting rate doubles the true coincidence counting rate.

Fortunately, in PGNAA application, the counting rate is normally not that high and the chance coincidence could be totally ignored. Also, if we consider the more improved coincidence response (relative ROI=3.8) over single response for the slab NaI/NaI setup for large coal sample, the acceptable counting rate could be almost doubled.

5.3 Dose Rate analysis

To evaluate the PGNAA application, the dose rates distribution around the device caused by neutrons and gamma-rays are of great concern and need to be investigated. The common method to calculate the dose rate for the human body is to use the flux-to-dose conversion factor (Bozkurt, 2000; Knoll, 1999) with the Monte Carlo simulation.

Three methods in MCNP5 can be used to calculate dose related issues. 1) F4 tally and FM card, which should be the flux-to-dose conversion factor for human. 2) F6 tally. 3) F8 tally. Only the first method is used here to evaluate the dose rates around PGNAA setup. Instead of the preliminary setups, a prototype of commercial PGNAA analyzer has been used for this evaluation (figure 5-10). For easier explanation, the conveyor belt moving direction is defined as X direction, the height is Z direction and crossing the belt is Y direction. The ^{252}Cf source is placed at the origin in the red block in figure 5-10. The blue part is hydrogen and Carbon enriched materiel to shield neutron and hold device. The detector assembly is on top.

The dose rate calculation is divided into two parts. One part is neutron dose rate and the other is photon dose rate. They are calculated with flux to dose rate conversion factors of NCRP-38 (Rossi et al., 1971) and 1977 ANSI/ANS, respectively, which are listed in Appendix B and Appendix C. The unit of the calculated dose rate (the same unit in figures 5-11 to 5-14) is (rem/hr)/(particles/s). The neutron dose rate maps for up to 3 meters around the PGNAA device are shown in figure 5-11 and 5-12 for Y-Z plane at x=0 cm and X-Y plane at z=0 cm, respectively. The X-Y plane is chosen at the neutron source level to represent the highest level neutron dose rate. The photon dose rate maps up to 3 meters around the PGNAA device are shown in figure 5-13 and 5-14 for Y-Z plane at x=0 cm and X-Y pane at z=35 cm, respectively. The X-Y plane shown here is chosen at the level of middle of coal sample.

Only the dose rate outside the device is of concern. It is obviously that the hydrogen and Carbon enriched materials are very effective in shielding neutron as expected. Behind these shielding, the neutron dose rate is in the magnitude of 10^{-11} near the device. The photon dose rate is kind of homogeneous distributed around the device and in the magnitude of 10^{-12} near the device, which is only 10% of the neutron induced dose rate. When the distance to the neutron source in the PGNAA analyzer is further than 3 meters, there is at least another magnitude drop in both neutron and photon dose rate.

As shown in the neutron source section, the ^{252}Cf neutron source could yield 2.3×10^{6} neutrons/ (μg.s). If a 10 microgram (μg) source is used, the neutron yield would be 2.3×10^{7} neutrons/s which could produce around 2.5×10^{-4} rem/hr dose equivalent rate from both neutron and photons. It equals to 0.25mrem/hr or 2.5 μSv/hr (Sv=sievert). According to the U.S. Nuclear Regulatory Commission (NRC) regulation, the annual limit of the total effective dose equivalent for radiation worker is 5 rems (0.05 Sv), while the annual limit for individual members of the public is 0.5 rem (5 mSv). So, the person who operates or maintains the PGNAA analyzer is allowed to stay close the device behind the shielding material for 2000 hours annually, even under the public limits. This shows a high potential to use larger amounts of the ^{252}Cf neutron source to increase the coincidence counting rate without going over the radiation limits even under the extreme conditions.

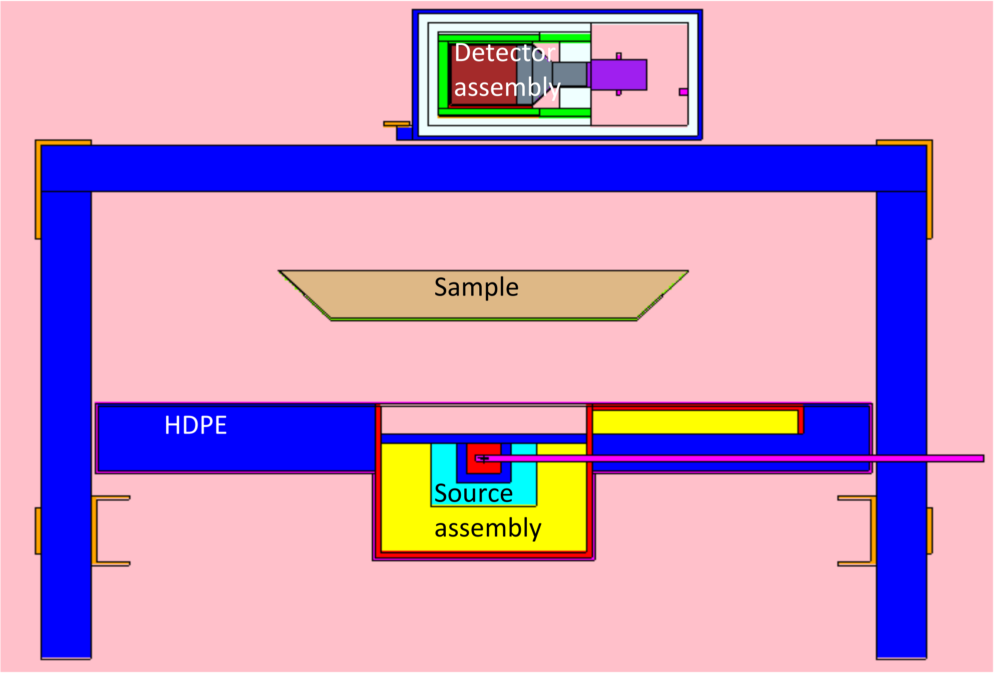

Figure 5-10 Prototype cross-belt online PGNAA analyzer

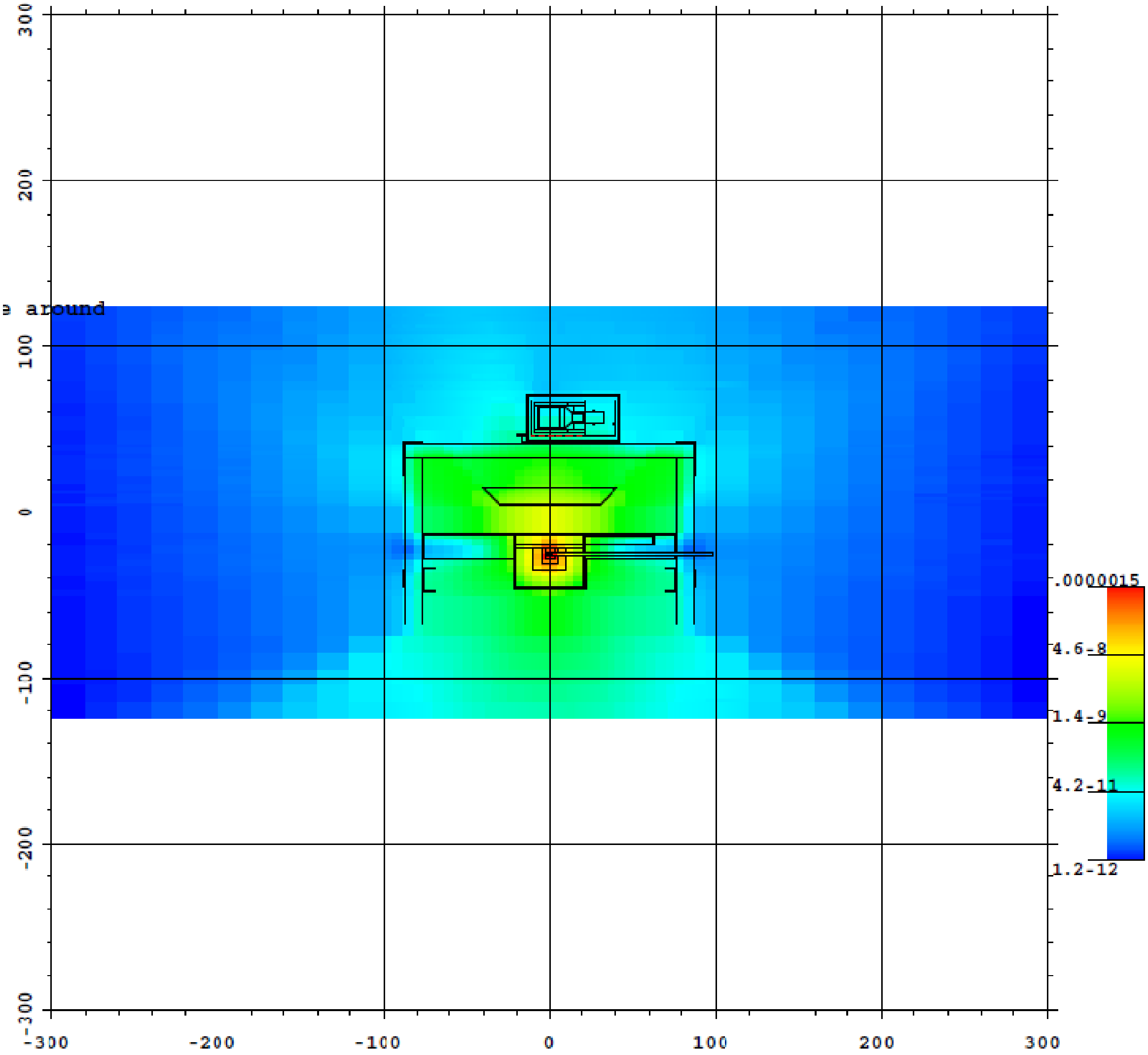

Figure 5-11 Neutron dose rate map for slice x= 0 (Y-Z plane)

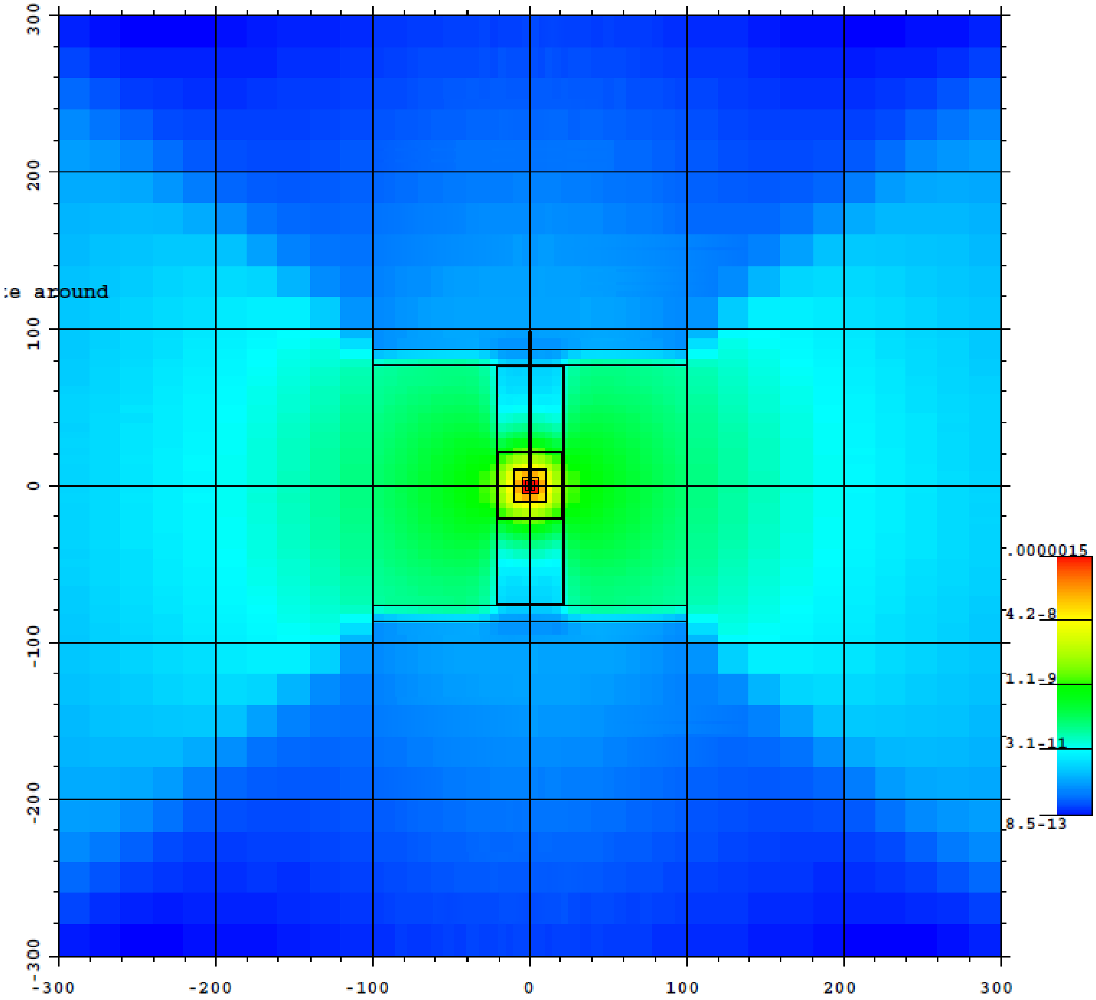

Figure 5-12 Neutron dose rate map for slice z = 0 (X-Y plane)

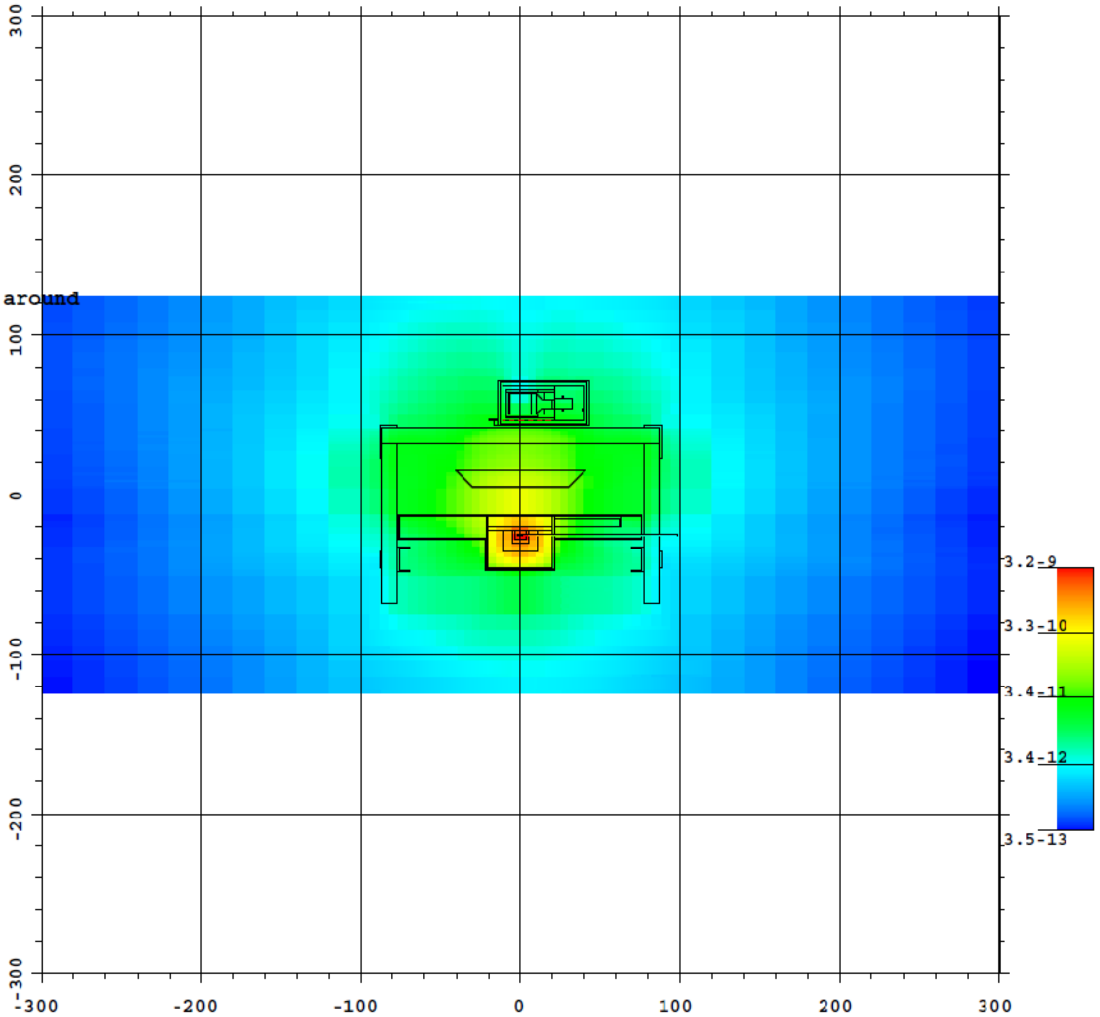

Figure 5-13 Photon dose rate map for slice x= 0 (Y-Z plane)

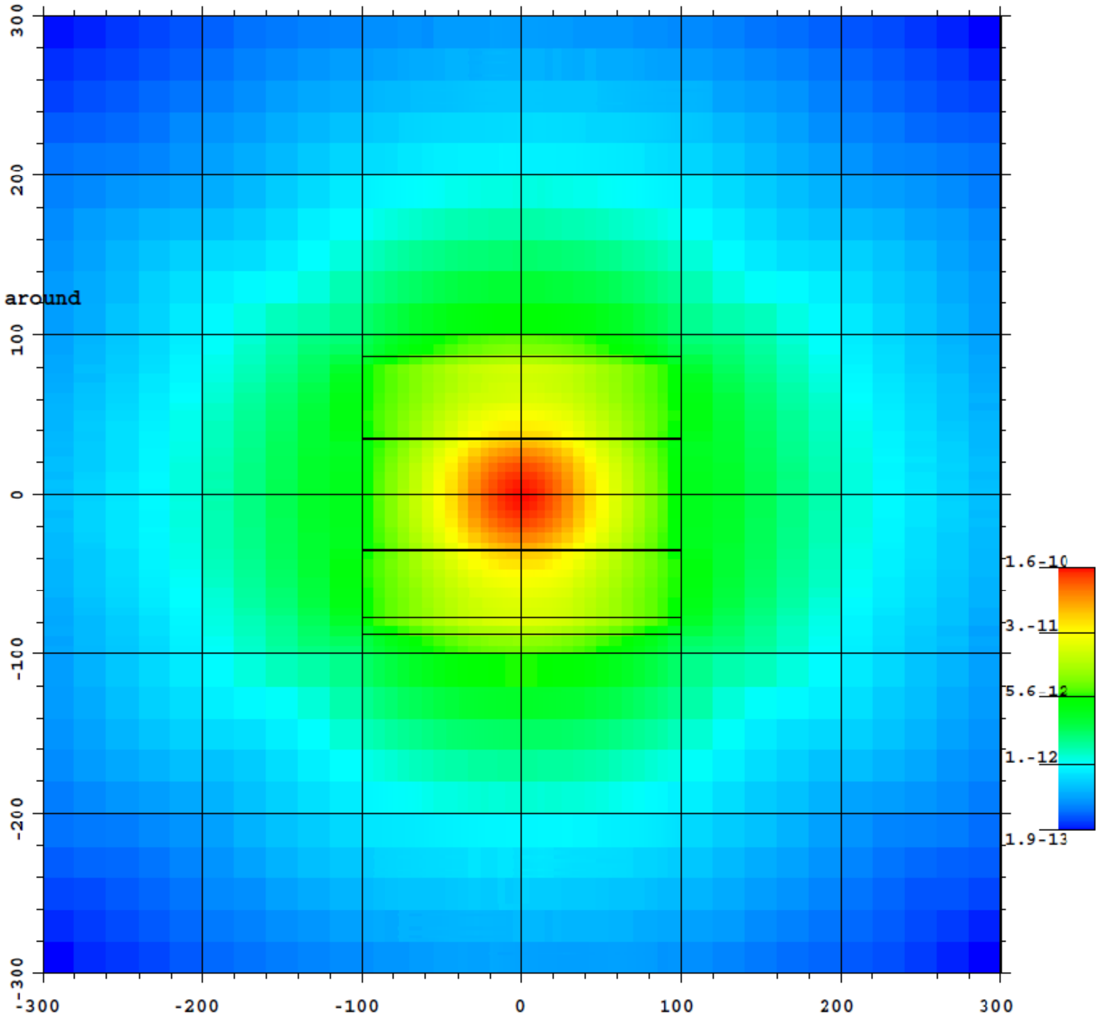

Figure 5-14 Neutron dose rate map for slice z = 35 (X-Y plane)

6 MC(DO)LLS QUANTITATIVE ANALYSIS

6.1 Overview

PGNAA has been used to analyze the large sized sample because the neutron and prompt gamma-rays are easier to penetrate through the sample. The first attempt on the non-linear problem for PGNAA has been done by Shyu at CEAR (Shyu et al., 1988, 1993). The method is called the Monte Carlo Library Least-Squares (MCLLS) approach. It requires having a very accurate forward model which enables the capability to calculate the pulse-height spectrum obtained with a PGNAA system when the geometrical and sample composition variables are known. This approach has been developed and successfully tested for the PGNAA analysis of bulk coal on simulated conveyor belts. The MCLLS method has been further tested with CEARCPG generated library spectra with experimental single total spectrum (Han et al., 2005). The results are promising.

The big disadvantage is the MCLLS is the need of iteratively simulating library spectra according to the fitting results with Monte Carlo simulation, which is very time consuming. Thus, differential operator approach has been combined with MCLLS to rapidly update the library spectra without running Monte Carlo simulation again. Also, with the advantage of coincidence measurement, the accuracy of MCLLS could be improved by utilizing Q-value summing (Gardner et al., 2004).

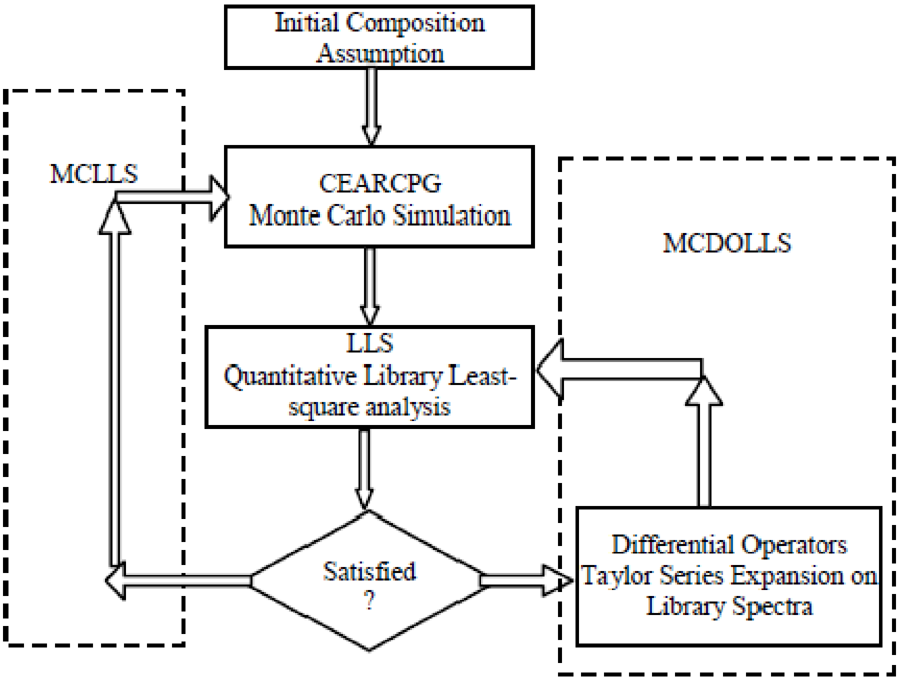

Figure 6-1 Flow chart of MC(DO)LLS quantitative analysis

6.2 Monte Carlo Library Least-Square

6.2.1 Theory and Procedure

The LLS approach assumes that the measurement process is linear. It means that any unknown sample spectrum is the sum of the products of the elemental amount and the library spectrum of each element for every channel. For each channel i (or energy bin) this is mathematically stated as:

$$y_i = \Sigma_{j=1}^{m} a_j x_{ij} + \varepsilon_i, i = 1, \ldots, n \tag{6-1}$$

where y_i is the counts of the unknown sample mixture in channel i, x_{ij} are the library spectra or counts in channel i of element j in the unknown sample mixture, and ε_i is the random error in counts in channel i. The a_js are found by minimizing the reduced chi-square value, which is expressed as,

$$\chi_v^2 = \frac{1}{n-m} \Sigma_{i=1}^{n} \frac{\varepsilon_i^2}{\sigma_i^2} \tag{6-2}$$

where σ_i is the variance of y_i which is usually taken as Poisson distributed and, therefore, equal to y_i. The minimization is done in the usual way by setting the derivatives of the reduced chi-square value with respect to each a_j equal to zero to obtain a system of m equations. These equations can be solved simultaneously by matrix inversion to find the a_j (Arinc et al., 1975).

The LLS code developed at CEAR provides the calculated elemental amounts and their standard deviations, the linear correlation coefficients between each element, the reduced chi-square value, and the residuals of the experimental minus the calculated sample spectra. The residuals are important in that elements that have been missed in the analysis can be easily identified.

The MCLLS approach consists of the following steps (figure 6-1).

1. Assume a sample composition as close to the actual one as possible.

2. The pulse-height spectra for the sample and each element are generated and separately recorded by Monte Carlo code using assumed values of the sample composition.

3. A linear library least-squares (LLS) analysis is performed and the elemental analysis so obtained is compared with the initially assumed values.

4. If the LLS elemental composition is close enough to the assumed values that the linearity assumption is valid, then they are taken as the final measured values. Otherwise, 1) the LLS values are taken as the next iteration of assumed values and steps 1 to 3 are repeated until the linearity assumption is valid. Or 2) updating library spectra with DO when available and repeat step 3 only.

6.2.2 Application in Coincidence PGNAA

The MCLLS method has been studied in coincidence PGNAA bulk coal measurement to quantitatively determine the elemental compositions based on the spectrum of the CEARCPG simulations. Two mixture samples have been assumed and listed in table 6-1. Sample 1 contains almost all common elements in coal at reasonable levels. Sample 2 only contain the major elements in coal and high concentrations of sulfur and mercury. Mercury and sulfur are of great interests since mercury is a toxic chemical element in the coal and sulfur can produce acid rain.

The coincidence library spectra and the total coincidence spectrum are simulated by CEARCPG. Poisson noise is added in the total coincidence spectrum to make up an unknown experimental spectrum for LLS analysis. The coincidence spectrum not only contains the coincidence gamma-rays from the sample, but also contains the coincidence gamma-rays from the structure materials and fission gamma-rays as we discussed in the previous chapter. They could also be simulated and include in LLS analysis as two interference libraries.

Two analyses have been done for each sample. One is based on the total coincidence spectra and the other one is based on 8 to 9 MeV diagonal energy window (figure 6-2). The energy window is chosen to include the Q-values of Mercury and Sulfur. The area in this energy window is projected to one axis to form the conventional 1D spectrum to be used in LLS analysis. The simulated total library spectra and Q-value projected spectra for sample 2 are shown in figure 6-3 and 6-4. The complete simulated library spectra of sample 1 can be found in Appendix D.

Table 6-1 The assumed composition of coal samples

Number	Element	Sample 1(weight%)	Sample 2(weight%)
1	Hydrogen	5.00	2.892
2	Carbon	61.80	75.280
3	Nitrogen	1.50	1.400
4	Oxygen	15.0	5.487
5	Sodium	0.10	1.121
6	Magnesium	0.10	N/A
7	Aluminum	2.00	2.380
8	Silicon	11.85	1.943
9	Phosphorous	0.10	N/A
10	Sulfur	0.50	5.6
11	Chlorine	0.50	1.729
12	Potassium	0.05	N/A
13	Calcium	0.20	N/A
14	Titanium	0.20	N/A
15	Manganese	0.04	N/A
16	Iron	1.00	N/A
17	Nickel	0.01	N/A
18	Mercury	0.05	2.168

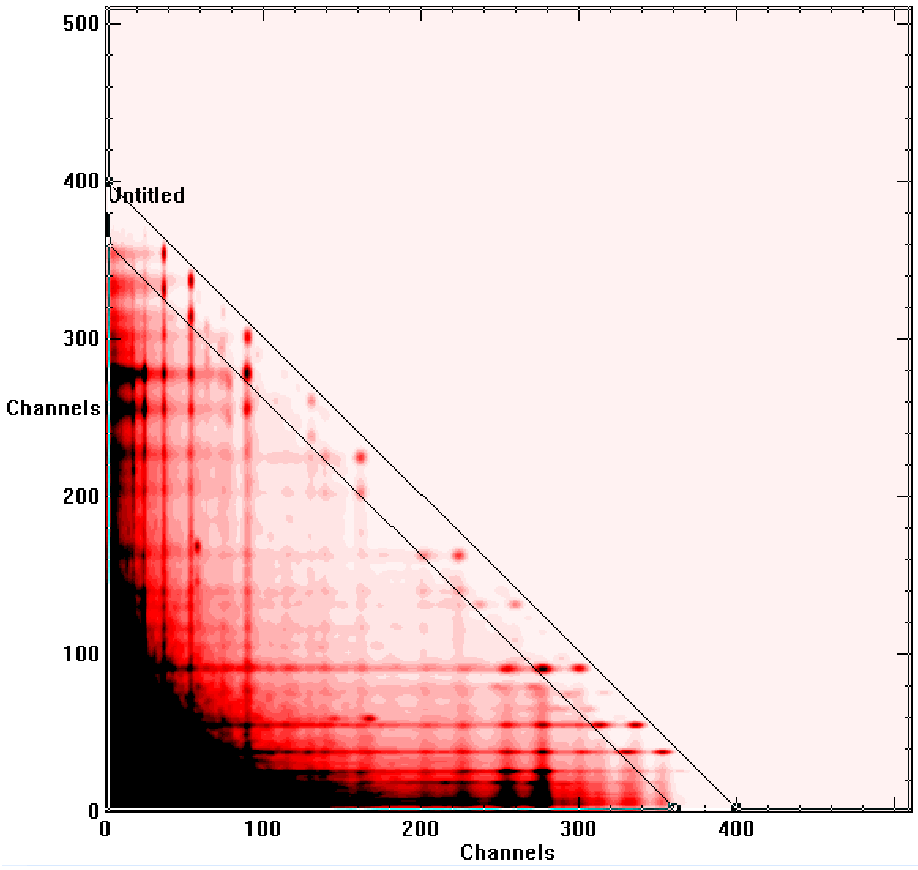

Figure 6-2 The Q-Value energy window for 8-9 MeV in 2D total coincidence spectra of sample 1

Hydrogen doesn't generate any coincidence prompt gamma-rays. From table 6-1, we could find that certain elements/isotopes have Q-values lower than 8 MeV. They do not contribute to the 8-9 MeV Q-value projection. They are carbon, oxygen and sodium. Although the Q values of some, like Al, is less than 8 MeV, there are still some counts from them in the energy window due to detector resolution.

One thing should be pointed out is the suppression of the fission gamma in Q-value projection. For sample 1, the percentage of coincidence fission gamma in total coincidence is reduced from 39% to 1.7%, while these values are 9.5% and 0.4%.

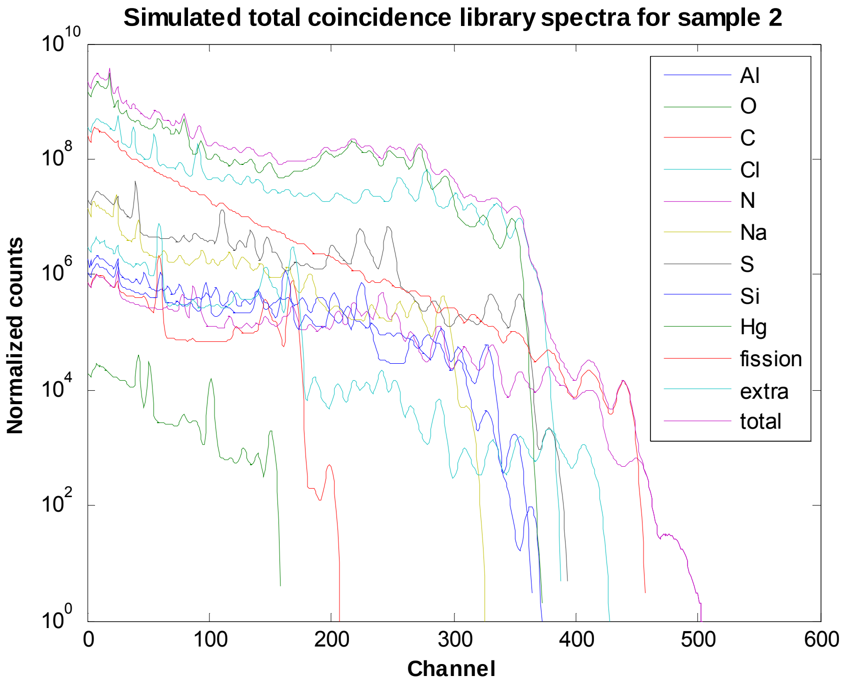

Figure 6-3 The simulated total coincidence spectra of sample 2

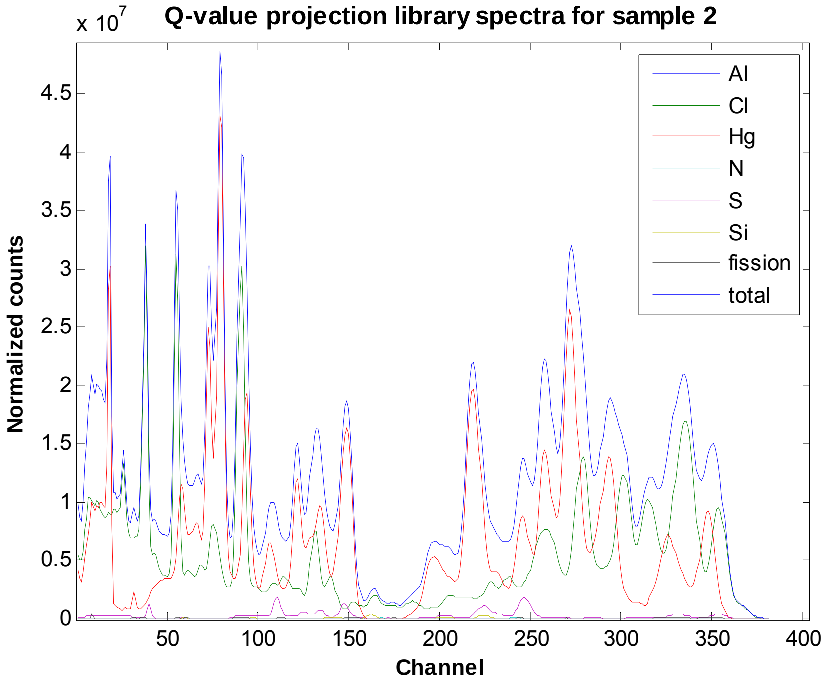

Figure 6-4 Q-value projection library spectra for sample 2

Table 6-2 The LLS fitting results of coal sample 1

Number	Element	Total coincidence Fitting results		Q-value projection Fitting results	
		Multiplier	Sigma%	Multiplier	Sigma%
1	Hydrogen	N/A	N/A	N/A	N/A
2	Carbon	5.8578	84.47	N/A	N/A
3	Nitrogen	0.76070	25.85	0.8786	69.90
4	Oxygen	-1.2642	378.78	N/A	N/A
5	Sodium	0.5827	114.19	N/A	N/A
6	Magnesium	-1.0038	426.52	-12.354	107.02
7	Aluminum	1.0406	33.08	0.8035	57.53
8	Silicon	1.0019	2.38	1.0093	1.93
9	Phosphorous	13.910	50.77	-0.3029	4124.59
10	Sulfur	1.2479	11.24	1.1066	17.58
11	Chlorine	1.0058	0.47	1.0072	0.63
12	Potassium	0.5774	107.45	2.9620	52.86
13	Calcium	1.0754	72.01	1.2119	87.58
14	Titanium	0.9724	5.18	1.0005	4.52
15	Manganese	0.7838	46.91	1.9195	110.89
16	Iron	0.8519	15.34	0.5551	29.10
17	Nickel	0.6988	149.90	1.2659	137.11
18	Mercury	0.9876	2.01	0.9095	5.07
Chi-square		0.842		0.913	

The MCLLS fitting results are listed in table 6-2 and 6-3. Because the 'experimental' unknown spectrum is made up from simulation, the fitting result '1' is the right answer for all elements. Based on the Reduced Chi-Square and the fitting results, the best fitting results are from the 8-9 MeV Q-value projection. For sample 2, the results of both sulfur and mercury are improved through Q-value projection. For sample 1, the result of sulfur is improved while the result of mercury has certain degradation. This result is reasonable since there is little interference in the high-energy window. For gamma-rays measurement, most of interferences concentrate in the low-energy region as the dark area in figure 6-2. The reason of mercury result in sample 1 is that the 8-9 MeV windows is too close to Mercury Q-value to include the whole peaks. When the concentration of Mercury is low as in sample 1, the benefited of less interference might be canceled out by the drop of signal due to energy window projection.

Table 6-3 The LLS fitting results of coal sample 2

Number	Element	Total coincidence Fitting results		Q-value projection Fitting results	
		Multiplier	Sigma%	Multiplier	Sigma%
1	Hydrogen	N/A	N/A	N/A	N/A
2	Carbon	-5.2954	398.58	N/A	N/A
3	Nitrogen	0.15586	302.80	-0.40777	313.56
4	Oxygen	-41.22	137.41	N/A	N/A
5	Sodium	1.0374	25.50	N/A	N/A
6	Aluminum	1.3045	65.34	0.63684	119.62
7	Silicon	0.9424	47.34	0.9178	20.92
8	Sulfur	1.0483	4.99	1.0278	5.00
9	Chlorine	1.0023	0.38	1.0011	0.37
10	Mercury	0.9992	0.19	1.0005	0.34
Chi-square		0.623		0.813	

6.3 Differential Operator Method

6.3.1 Overview

In Monte Carlo simulation, the response of a specific tally is a function of several variables, such as the energy of the particles, the cross section and atomic density of elements, etc. The basic idea of the differential operator technique is, if the magnitude of perturbation is very small, the ratio of changed response can be found by using Taylor series expansion. The differential operator technique was introduced into Monte Carlo simulation by Olhoeft in the early 1960s (Olhoeft, 1962) and was generalized for perturbations in cross section data by Rief (Rief, 1984, 1994). In Rief's work, the response kernel was divided into two the parts, the collision and the transportation parts. The first order and the second order of Taylor series coefficients were derived according to each part. In his work, the derivatives for the collision and transportation kernel were based on pure analog simulation and no variance reduction techniques were considered. A rudimentary implementation into MCNP was done by McKinney (McKinney, 1984) and implemented as a standard feature in MCNP4B. In MCNP, Subroutine PERTUB, which is used to calculate the differential derivatives, is only called once after the particle flight distance is determined. The differential operator technique in MCNP only can be applied to the tallies which are related to particle flux, such as the F1, F2 and F4 tallies. It cannot be used to predict the change of pulse-height spectrum in MCNP.

At CEAR, this technique was first adopted in the code CEARXRF on pure analog simulation by Guo (Guo, 2003) with first order derivatives and then added second order derivatives by Li (Li, 2008). For code CEARCPG, several variance reduction techniques need to be derived at first and tested.

In general, the response of a small cross section or atomic density perturbation for Monte Carlo simulation can be expressed as a Taylor series expansion about the reference composition x_0,

$$\psi(\vec{r};x_0+\Delta x)=\psi(\vec{r};x)\Big|_{x0}+\sum_{j=1}^{m}\frac{\partial\psi(\vec{r};x_j)}{\partial x_j}\Bigg|_{x_{j0}}\Delta x_j$$
$$+\frac{1}{2}\sum_{j1=1}^{m}\sum_{j2=1}^{m}\frac{\partial^2\psi(\vec{r};x)}{\partial x_{j1}\partial x_{j2}}\Bigg|_{x_{j10},x_{j20}}\Delta x_{j1}\Delta x_{j2}+o(\Delta x^3) \tag{6-3}$$

Where $\psi(\vec{r};x_0+\Delta x)$ is the response for a small perturbation Δx ; $\psi(\vec{r},x)\big|_{x0}$ is the response at the reference composition x_0; $\vec{r}$ is the coordinate of the particle; $\frac{\partial\psi(\vec{r};x_j)}{\partial x_j}\Big|_{x_{j0}}$ and $\frac{\partial^2\psi(\vec{r};x)}{\partial x_{j1}\partial x_{j2}}\Big|_{x_{j10},x_{j20}}$ are Taylor derivatives at the reference point of *jth* element. x is the perturbation variable; *m* is the number of perturbed elements and $o(\Delta x^3)$ is the third-order expected error of Taylor series expansion.

In Monte Carlo, the final response is determined by two main factors, the particle numbers and the weight of each tallied particle. Scoring the derivatives requires that the derivatives are determined and summed up at each collision point and along each particle track. Eventually the summation has to be multiplied by the particle weight factor to obtain the response at the given collision point. Most variance reduction techniques need to change the numbers of particles or the weight of particles. If this adjusting is cross section related, the differential operator should be calculated.

Theoretically, the particle weight in the Monte Carlo game can be considered as a series of weight adjusting steps:

$$w_n(x)=w_0\cdot f(x)_1\cdot f_2(x)\cdots f_{n-1}(x)\cdot f_n(x)=w_{n-1}(x)\cdot f_n(x) \tag{6-4}$$

Where w_0 is the initial particle weight; w_n is the particle weight after n steps; $f_n(x)$ is the weight correction factor at step n and the weight correction factor is a function of cross section. The derivatives of particle weight can be calculated by the following equation:

$$\frac{\partial w_n(x)}{\partial x_j}\Big|_{x_0} = \frac{\partial w_{n-1}(x)}{\partial x_j}\Big|_{x_0} \cdot f(x_0) + w_{n-1}(x_0) \cdot \frac{\partial f_n(x)}{\partial x_j}\Big|_{x_0} \tag{6-5}$$

$$\begin{aligned}\frac{\partial^2 w_n(x)}{\partial x_j^2}\Big|_{x_0} &= \frac{\partial^2 w_{n-1}(x)}{\partial x_j^2}\Big|_{x_0} \cdot f_n(x_0) + 2\frac{\partial w_{n-1}(x)}{\partial x_j}\Big|_{x_0} \cdot \frac{\partial f_n(x)}{\partial x_j}\Big|_{x_0} \\ &\quad + w_{n-1}(x_0) \cdot \frac{\partial^2 f_n(x)}{\partial x_j^2}\Bigg|_{x_0}\end{aligned} \tag{6-6}$$

$$\begin{aligned}\frac{\partial^2 w_n(x)}{\partial x_{j_1} \partial x_{j2}}\Big|_{x_0} &= \frac{\partial^2 w_{n-1}(x)}{\partial x_{j_1} \partial x_{j2}}\Big|_{x_0} \cdot f_n(x_0) + \frac{\partial w_{n-1}(x)}{\partial x_{j_1}}\Big|_{x_0} \cdot \frac{\partial f_n(x)}{\partial x_{j_2}}\Big|_{x_0} \\ &\quad + \frac{\partial w_{n-1}(x)}{\partial x_{j_2}}\Big|_{x_0} \cdot \frac{\partial f_n(x)}{\partial x_{j_1}}\Big|_{x_0} + w_{n-1}(x_0) \cdot \frac{\partial^2 f_n(x)}{\partial x_{j_1} \partial x_{j_2}}\Bigg|_{x_0}\end{aligned} \tag{6-7}$$

The particle transport and collision kernels have been derived in previous work of CEAR (Li, 2008). To implant the differential operator into code CEARCPG or other Monte Carlo codes with variance reduction techniques, the following variance reduction techniques are also discussed besides the particle transport and collision. They are: (1) the truncated pdf and (2) stratified sampling.

6.3.2 Transport Kernel Derivatives

The transport kernel is related to the particle travel length which has two cases. (1) The particle starts in the perturbed cell and ends with boundary crossings and (2) the particle starts with a boundary crossing and ends with an interaction in the perturbed cell. The detailed derivation can be found Li's work and will be omitted here, and the first and second order derivatives are listed in table 6-3.

In table 6-3, x_j is the atomic density of perturbed isotope *j* (*j₁* and *j₂* are two perturbed isotopes in cross term), σ_j is the microscopic cross section of perturbed isotope *j*, *l* is the particle travel distance in the perturbed cell, Σ_0 is the macroscopic cross section of other isotopes except the perturbed isotope j.

Table 6-4 The derivatives at the given reference composition for transport kernel

	Case 1	**Case 2**
First order derivative	$\left.\frac{\partial f}{\partial x_j}\right\|_{x0} = -\sigma_j l$	$\left.\frac{\partial f}{\partial x_j}\right\|_{x_{0j}} = \sigma_j\left(\frac{1}{\Sigma_0 + x_{0j}\sigma_j} - l\right)$
Second order derivative	$\left.\frac{\partial^2 f}{\partial {x_j}^2}\right\|_{x0} = (\sigma_j l)^2$	$\left.\frac{\partial^2 f}{\partial {x_j}^2}\right\|_{x_{0j}} = {\sigma_j}^2 l\left(l - \frac{2}{\Sigma_0 + x_{0j}\sigma_j}\right)$
Cross term derivative	$\left.\frac{\partial^2 f}{\partial x_{j1}\partial x_{j2}}\right\|_{x0} = \sigma_{j1}\sigma_{j2}l^2$	$\left.\frac{\partial^2 f}{\partial x_{j_1}\partial x_{j_2}}\right\|_{x_{0j1}x_{0j2}} = \sigma_{j_1}\sigma_{j_2}l\left(l - \frac{2}{\Sigma_0 + x_{0j_1}\sigma_{j_1} + x_{0j_2}\sigma_{j_2}}\right)$

6.3.3 Particle Collision Derivatives

The particle collision kernel also has two cases. (1) The perturbed isotopes are sampled and (2) the isotopes other than perturbed isotope are sampled. Normally, the sampling of interacting isotope is based on its macroscopic cross section, so the probability of selecting isotope *j* and the corresponding weight correction factor for the selection are functions of the isotope atomic density of isotope *j*. The resulted derivatives are listed in table 6-4.

For case 2, when an isotope other than the perturbed isotope is selected, the pdf function *p* of selecting one isotope other than perturbed isotopes and the weight correction factor *f* can be described as:

$$p = \frac{x_{0k}\sigma_k}{\Sigma_0 + x_j\sigma_j} \tag{6-8}$$

$$f = \frac{x_{0k}\sigma_k}{\Sigma_0 + x_j\sigma_j}\frac{\Sigma_0 + x_{0j}\sigma_j}{x_{0k}\sigma_k} \tag{6-9}$$

where x_{0k} and σ_k are the atomic density and cross section of sampled isotope.

Table 6-5 The derivatives at the given reference composition for collision kernel

	Case 1	**Case 2**
First order derivative	$\frac{\partial f}{\partial x_j}\Big\|_{x_0} = \frac{\Sigma_0}{x_{0j}\left(\Sigma_0 + x_{0j}\sigma_j\right)}$	$\frac{\partial f}{\partial x_j}\Big\|_{x_0} = \frac{-\sigma_j}{\Sigma_0 + x_{0j}\sigma_j}$
Second order derivative	$\frac{\partial^2 f}{\partial {x_j}^2}\Big\|_{x_0} = \frac{-2\sigma_j\Sigma_0}{x_{0j}\left(\Sigma_0 + x_{0j}\sigma_j\right)^2}$	$\frac{\partial^2 f}{\partial {x_j}^2}\Big\|_{x_0} = \frac{2{\sigma_j}^2}{\left(\Sigma_0 + x_{0j}\sigma_j\right)^2}$
Cross term derivative	$\frac{\partial^2 f}{\partial x_{j_1}\partial x_{j_2}}\Big\|_{x_{0j_1}x_{0j_2}} = \frac{-\sigma_{j_2}\left(\Sigma_0 - x_{0j_1}\sigma_{j_1} + x_{0j_2}\sigma_{j_2}\right)}{x_{0j_1}\left(\Sigma_0 + x_{0j_1}\sigma_{j_1} + x_{0j_2}\sigma_{j_2}\right)^2}$	$\frac{\partial^2 f}{\partial x_{j_1}\partial x_{j_2}}\Big\|_{x_{0j_1}x_{0j_2}} = \frac{-2\sigma_{j_1}\sigma_{j_2}}{\left(\Sigma_0 + x_{0j_1}\sigma_{j_1} + x_{0j_2}\sigma_{j_2}\right)^2}$

6.3.4 Derivatives For Variance Reduction Techniques

Usually, the weight adjusting of most variance reduction techniques depend on the cross section which is a function of element atomic density, such as implicit capture, forcing interaction, truncated pdf and so on. In the perturbation problem, the derivatives should be calculated when the variance reduction techniques are used. Lots of credit on the derivatives should be given to Han (Han, 2009).

Stratified Sampling

Stratified sampling is a useful and inexpensive variance reduction that can be used in sampling the collision isotope and interaction type. The biggest advantage of the stratified sampling is it can dramatically increase the calculation efficiency. This technique is widely used in the specific-purpose Monte Carlo code CEARCPG.

Code CEARCPG is a specified purpose Monte Carlo code that was designed for normal PGNAA analysis and coincidence PGNAA analysis. Since most elements have higher neutron radiative capture cross section at thermal energy range, the high-energy neutron would be scattered with materials and slow down to thermal energy before they undergo the neutron radiative interaction. In the analog simulation, during the slowing down process, one neutron radiative capture reaction will kill this neutron history and reduce the computation efficiency. When the stratified sampling is used to sample the neutron interaction, the neutron interaction was split into two parts, the neutron scattering parts and neutron radiative capture reaction parts. For each neutron collision, the neutron is always survived from neutron scattering reaction and the weight of survived neutron is:

$$w = w_0 \frac{\Sigma_{el} + \Sigma_{inel}}{\Sigma_T} \tag{6-10}$$

where w_0 is the neutron's weight before collision and Σ_T is the total macroscopic cross section and Σ_{el} , Σ_{inel} are the macroscopic cross section for neutron elastic scattering and neutron inelastic scattering reaction. In CEARCPG, the survived neutron will only be terminated if Russian roulette is played or it escapes the system.

The weight of neutron which undergoes neutron radiative capture reaction is:

$$w = w_0 \frac{\Sigma_{cp}}{\Sigma_T} \tag{6-11}$$

where w_0, Σ_T are same as those in equation 31 and Σ_{cp} is the macroscopic neutron radiative capture reaction. In neutron radiative capture reaction, neutron will be killed by absorption.

Since both of equations are functions of macroscopic cross section, derivatives should be calculated if perturbation problem is carried on. For neutron scattering reaction, the weight adjusting factor *f* is:

$$f = \frac{\left(\Sigma_0 + x_j\sigma_j\right)_{el} + \left(\Sigma_0 + x_j\sigma_j\right)_{inel}}{\left(\Sigma_0 + x_j\sigma_j\right)_{Tot}} \frac{\left(\Sigma_0 + x_{0j}\sigma_j\right)_{Tot}}{\left(\Sigma_0 + x_{0j}\sigma_j\right)_{el} + \left(\Sigma_0 + x_{0j}\sigma_j\right)_{inel}} \tag{6-12}$$

And the first order and the second order derivatives at the reference composition are:

$$\left.\frac{\partial f}{\partial x_j}\right|_{x_{0j}} = \frac{\sigma_{jel} + \sigma_{jinel}}{\left(\Sigma_0 + x_j\sigma_j\right)_{el} + \left(\Sigma_0 + x_j\sigma_j\right)_{inel}} - \frac{\sigma_j}{\left(\Sigma_0 + x_j\sigma_j\right)} \tag{6-13}$$

$$\frac{\partial^2 f}{\partial {x_j}^2}\bigg|_{x_{0j}} = \frac{-2\sigma_j\left(\sigma_{jel}+\sigma_{jinel}\right)}{\left[\left(\Sigma_0+x_j\sigma_j\right)_{el}+\left(\Sigma_0+x_j\sigma_j\right)_{inel}\right]\left(\Sigma_0+x_j\sigma_j\right)}+\frac{2\sigma^2{}_j}{\left(\Sigma_0+x_j\sigma_j\right)^2} \qquad \text{(6-14)}$$

The cross term in the second derivative of the weight correction factor evaluated at the reference composition is:

$$\frac{\partial^2 f}{\partial x_{j_1}\partial x_{j_2}}\bigg|_{x_{0j_1}x_{0j_2}} = -\frac{\left[\sigma_{j_1}\left(\sigma_{j_{2inel}}+\sigma_{j_{2el}}\right)+\sigma_{j_2}\left(\sigma_{j_{1inel}}+\sigma_{j_{1el}}\right)\right]}{\left[\left(\Sigma_0+x_{0j_1}\sigma_{j_1}+x_{0j_2}\sigma_{j_2}\right)_{el}+\left(\Sigma_0+x_{0j_1}\sigma_{j_1}+x_{0j_2}\sigma_{j_2}\right)_{inel}\right]\left(\Sigma_0+x_{0j_1}\sigma_{j_1}+x_{0j_2}\sigma_{j_2}\right)}$$
$$+\frac{2\sigma_{j_1}\sigma_{j_2}}{\left(\Sigma_0+x_{0j_1}\sigma_{j_1}+x_{0j_2}\sigma_{j_2}\right)^2} \qquad (6-15)$$

For neutron radiative capture reaction, the weight adjusting factor *f* is:

$$f=\frac{\left(\Sigma_0+x_j\sigma_j\right)_{cp}}{\left(\Sigma_0+x_j\sigma_j\right)_{Tot}}\frac{\left(\Sigma_0+x_{0j}\sigma_j\right)_{Tot}}{\left(\Sigma_0+x_{0j}\sigma_j\right)_{cp}} \qquad \text{(6-16)}$$

The first order and the second order of datives at the reference composition are:

$$\frac{\partial f}{\partial x_j}\bigg|_{x_{0j}} = \frac{\left(\Sigma_0+x_{0j}\sigma_j\right)\sigma_{jcp}-\left(\Sigma_0+x_{0j}\sigma_j\right)_{cp}\sigma_j}{\left(\Sigma_0+x_{0j}\sigma_j\right)_{cp}\left(\Sigma_0+x_{0j}\sigma_j\right)} \qquad \text{(6-17)}$$

$$\frac{\partial^2 f}{\partial {x_j}^2}\bigg|_{x_{0j}} = \frac{\left(2\left(\Sigma_0+x_{0j}\sigma_j\right)_{cp}\sigma_j-\left(\Sigma_0+x_{0j}\sigma_j\right)\sigma_{jcp}\right)\sigma_j}{\left(\Sigma_0+x_{0j}\sigma_j\right)_{cp}\left(\Sigma_0+x_{0j}\sigma_j\right)^2} \qquad \text{(6-18)}$$

And the cross term in the second derivative of the weight correction factor evaluated at the reference composition is:

$$\left.\frac{\partial^2 f}{\partial x_{j_1}\partial x_{j_2}}\right|_{x_{0j_1}x_{0j_2}} = -\frac{\left(\Sigma_0 + x_{0j_1}\sigma_{j_1} + x_{0j_2}\sigma_{j_2}\right)\left(\sigma_{j_2cp}\sigma_{j_1} + \sigma_{j_1cp}\sigma_{j_2}\right) - 2\sigma_{j_1}\sigma_{j_2}\left(\Sigma_0 + x_{0j_1}\sigma_{j_1} + x_{0j_2}\sigma_{j_2}\right)_{cp}}{\left(\Sigma_0 + x_{0j_1}\sigma_{j_1} + x_{0j_2}\sigma_{j_2}\right)_{cp}\left(\Sigma_0 + x_{0j_1}\sigma_{j_1} + x_{0j_2}\sigma_{j_2}\right)^2} \tag{6-19}$$

When the stratified sampling is used to sample the collision isotopes, the sampling of isotopes can be divided into several parts. The number of parts divided is the same as the number of the isotopes presented in the sample. By using stratified sampling, each isotope is forced to be interacted with neutron. The weight of neutron should be adjusted based on the following equation:

$$w = w_0 \frac{\Sigma_i}{\Sigma_T} \tag{6-20}$$

Where Σ_i is the macroscopic cross section of *i-th* element which is interacted with neutron. It is similar to the particle collision kernel described previously. There are two cases. (1) The sampled isotopes are the perturbed isotopes and (2) the sampled isotopes are the isotopes other than the perturbed ones. For the case one, the first and the second order derivatives at the reference composition are:

$$\left.\frac{\partial f}{\partial x_j}\right|_{x_0} = \frac{\Sigma_0}{x_{0j}\left(\Sigma_0 + x_{0j}\sigma_j\right)} \tag{6-21}$$

$$\left.\frac{\partial^2 f}{\partial x_j{}^2}\right|_{x_0} = \frac{-2\sigma_j\Sigma_0}{x_{0j}\left(\Sigma_0 + x_{0j}\sigma_j\right)^2} \tag{6-22}$$

$$\left.\frac{\partial^2 f}{\partial x_{j_1}\partial x_{j_2}}\right|_{x_{0j_1}x_{0j_2}} = \frac{-\sigma_{j_2}\left(\Sigma_0 - x_{0j_1}\sigma_{j_1} + x_{0j_2}\sigma_{j_2}\right)}{x_{0j_1}\left(\Sigma_0 + x_{0j_1}\sigma_{j_1} + x_{0j_2}\sigma_{j_2}\right)^2} \tag{6-23}$$

For the case two, the first and the second order derivatives at the reference composition are:

$$\frac{\partial f}{\partial x_j}\Big|_{x_0} = \frac{-\sigma_j}{\Sigma_0 + x_{0j}\sigma_j} \qquad (6\text{-}24)$$

$$\frac{\partial^2 f}{\partial x_j^{\,2}}\Big|_{x_0} = \frac{2\sigma_j^{\,2}}{\left(\Sigma_0 + x_{0j}\sigma_j\right)^2} \qquad (6\text{-}25)$$

$$\frac{\partial^2 f}{\partial x_{j_1}\partial x_{j_2}}\Big|_{x_{0j_1}x_{0j_2}} = \frac{2\sigma_{j_1}\sigma_{j_2}}{\left(\Sigma_0 + x_{0j_1}\sigma_{j_1} + x_{0j_2}\sigma_{j_2}\right)^2} \qquad (6\text{-}26)$$

Truncated PDF

Truncated pdf will be used if the particle will escaped from the system. By using the truncated pdf, the particle will be forced to be interacted before it reaches the cell boundary. The truncated pdf is:

$$p(x) = \frac{\Sigma_{Tot}\exp(-\Sigma_{Tot}x)}{1-\exp(-\Sigma_{Tot}D)} \qquad (6\text{-}27)$$

And the weigh is needed to be adjusted by the factor:

$$w = w_0[1-\exp(-\Sigma_{Tot}D)] \qquad (6\text{-}28)$$

Where Σ_{Tot} is the total macroscopic cross section, *D* is distance from the position of the particle to the boundary surface and *x* is the particle travel distance. Both of equation 48 and 49 are the functions of cross section. If the truncated pdf is applied in the perturbed cell, a weight correction must be made to get the right differential calculation.

For the equation 48, the weight correction is:

$$f = \frac{(\Sigma_{Tot} + x_j\sigma_j)\exp[-(\Sigma_{Tot} + x_j\sigma_j)x]}{1-\exp[-(\Sigma_{Tot} + x_j\sigma_j)D]} \cdot \frac{1-\exp[-(\Sigma_{Tot} + x_{0j}\sigma_j)D]}{(\Sigma_{Tot} + x_{0j}\sigma_j)\exp[-(\Sigma_{Tot} + x_{0j}\sigma_j)x]} \tag{6-29}$$

The first and the second derivatives at the reference composition are:

$$\frac{\partial f}{\partial x_j}\Big|_{x_{0j}} = \frac{1}{\Sigma_T^0}\sigma_j\left(1-\Sigma_T^0 l\right) - \frac{\sigma_j D}{1-\exp(-\Sigma_T^0 D)}\exp(-\Sigma_T^0 D) \tag{6-30}$$

$$\begin{aligned} \frac{\partial^2 f}{\partial x^2{}_j}\Big|_{x_{0j}} &= \frac{1}{\Sigma_T^0}\sigma_j^2 l\left(\Sigma_T^0 l - 2\right) - \frac{1}{\Sigma_T^0}\frac{\sigma^2{}_j D}{1-\exp(-\Sigma_T^0 D)}\left(1-\Sigma_T^0 l\right)\exp(-\Sigma_T^0 D) \\ &- \frac{1}{\Sigma_T^0}\frac{\sigma^2{}_j D}{1-\exp(-\Sigma_T^0 D)}\exp(-\Sigma_T^0 D)\left[1-\left(l+D\right)\Sigma_T^0\right] \\ &+ \frac{2}{\left(1-\exp(-\Sigma_T^0 D)\right)^2}\sigma^2{}_j D^2 \exp(-2\Sigma_T^0 D) \end{aligned} \tag{6-31}$$

$$\frac{\partial^2 f}{\partial x_{j_1}\partial x_{j_2}}\Big|_{x_{0j}} = \frac{1}{\Sigma_T^0}\sigma_{j_1}\sigma_{j_2} l\left(\Sigma_T^0 l - 2\right) - \frac{1}{\Sigma_T^0}\frac{\sigma_{j_1}\sigma_{j_2} D}{1-\exp(-\Sigma_T^0 D)}\left(1-\Sigma_T^0 l\right)\exp(-\Sigma_T^0 D) \tag{6-32}$$

For the equation 49, the weight correction factor is:

$$f = \frac{1-\exp[-(\Sigma_0 + x_j\sigma_j)D]}{1-\exp[-(\Sigma_0 + x_{0j}\sigma_j)D]} \tag{6-33}$$

The first and the second derivatives are:

$$\frac{\partial f}{\partial x_j}\Big|_{x_{0j}} = \frac{\sigma_j D\exp[-\left(\Sigma_0 + x_{0j}\sigma_j\right)D]}{1-\exp[-\left(\Sigma_0 + x_{0j}\sigma_j\right)D]} \tag{6-34}$$

$$\frac{\partial^2 f}{\partial x_j^{\ 2}}\bigg|_{x_{0j}} = \frac{-(\sigma_j D)^2 \exp[-\left(\Sigma_0 + x_{0j}\sigma_j\right)D]}{1-\exp[-\left(\Sigma_0 + x_{0j}\sigma_j\right)D]} \tag{6-35}$$

$$\frac{\partial^2 f}{\partial x_{j_1}\partial x_{j_2}}\bigg|_{x_{0j_1}x_{0j_2}} = \frac{-\sigma_{j_1}\sigma_{j_2}D^2 \exp[-\left(\Sigma_0 + x_{0j_1}\sigma_{j1} + x_{0j_2}\sigma_{j2}\right)D]}{1-\exp[-\left(\Sigma_0 + x_{0j_1}\sigma_{j1} + x_{0j_2}\sigma_{j2}\right)D]} \tag{6-36}$$

6.3.5 Simulation Results

For code CEARCPG, since the simulation of PGNAA analysis not only involves neutron transportation, but also involves the photons transportation, both of them are needed to take into account if differential operator is applied. Mathematically, the equations for theses two particles are same. The derivatives of differential operator should be calculated if particles undergo any transportation, interaction or any variance reduction techniques which are involved within the perturbed elements. The derivatives are recorded according to each element. The corrected elemental library spectra can be calculated based on the differential spectra and the spectra at the reference composition for further MCLLS application.

To verify the implementation of the Monte Carlo - Differential Operator method in CEARCPG, one simulation case was carried out with the geometry in figure 6-x. The first sample is coal as listed in table 6-5. Only one perturbation element is investigated, corresponding to 5% increase of mercury. Figure 6-x to 6-x shows the calculated the differential spectra without convolution with detector response function. Each perturbed element has a set of differential spectra. It is clear that element mercury has positive response due to the perturbation of mercury. The responses of the other elements are mostly negative. Figure 6-x shows the library spectrum of mercury after the convolution with detector response function. It is clear that differential corrected mercury library spectrum agree with the Monte Carlo directly simulated spectrum well.

Table 6-6 Reference ample composition in CEARCPG test for DO

Elements	**H**	**C**	**B**	**N**	**O**
%weight	5.1925	75.1783	2.9337	1.418	6.2668
Elements	Na	Mg	Al	Si	Hg
%weight	0.04935	0.05941	0.58116	2.2579	6.0673

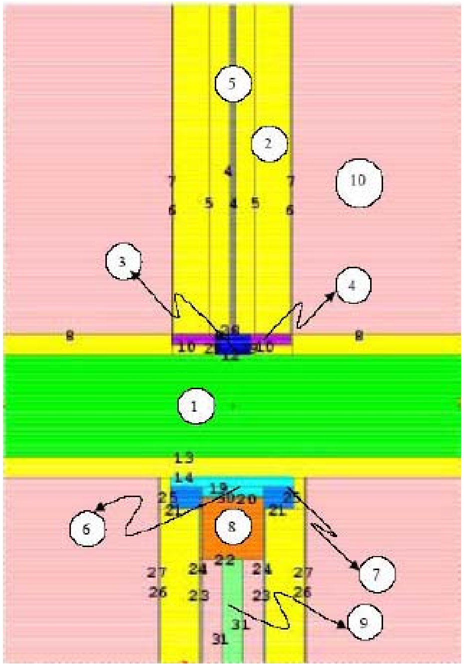

Figure 6-5 The geometry configuration in CEARCPG test for differential operator where 1 is coal sample, 2 the polyethylene, 3 bismuth with the neutron source, 4 air, 5 aluminum, 6 Lithium polyethylene, 7 lead, 8 NaI detector, 9 SiO2 (PMT) and 10 is paraffin

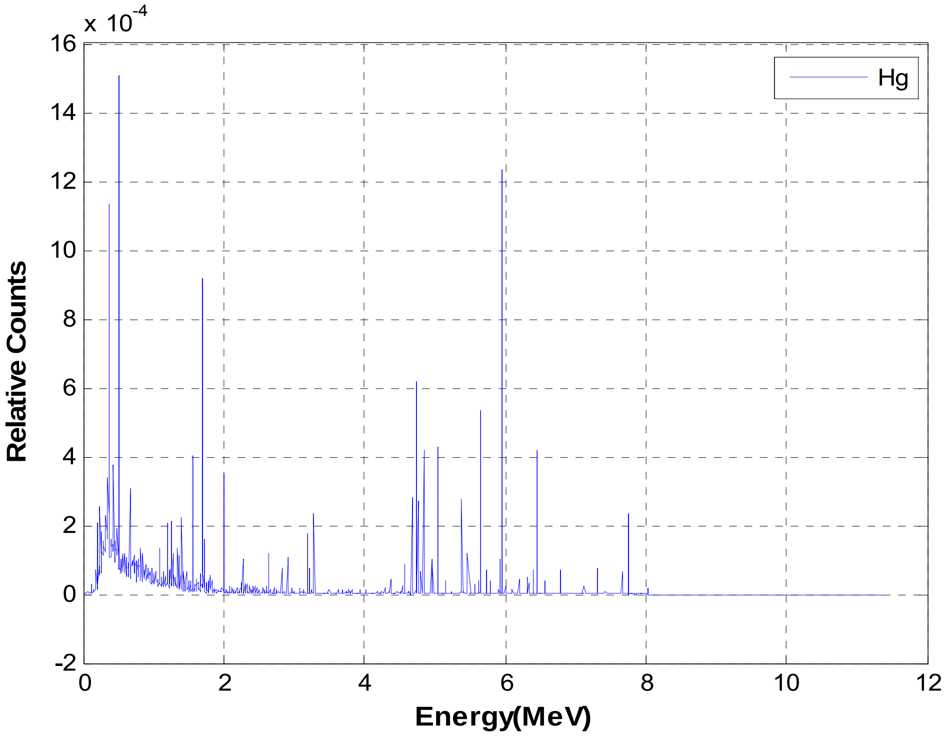

Figure 6-6 The CEARCPG calculated Hg differential spectrum with respect to Hg perturbation

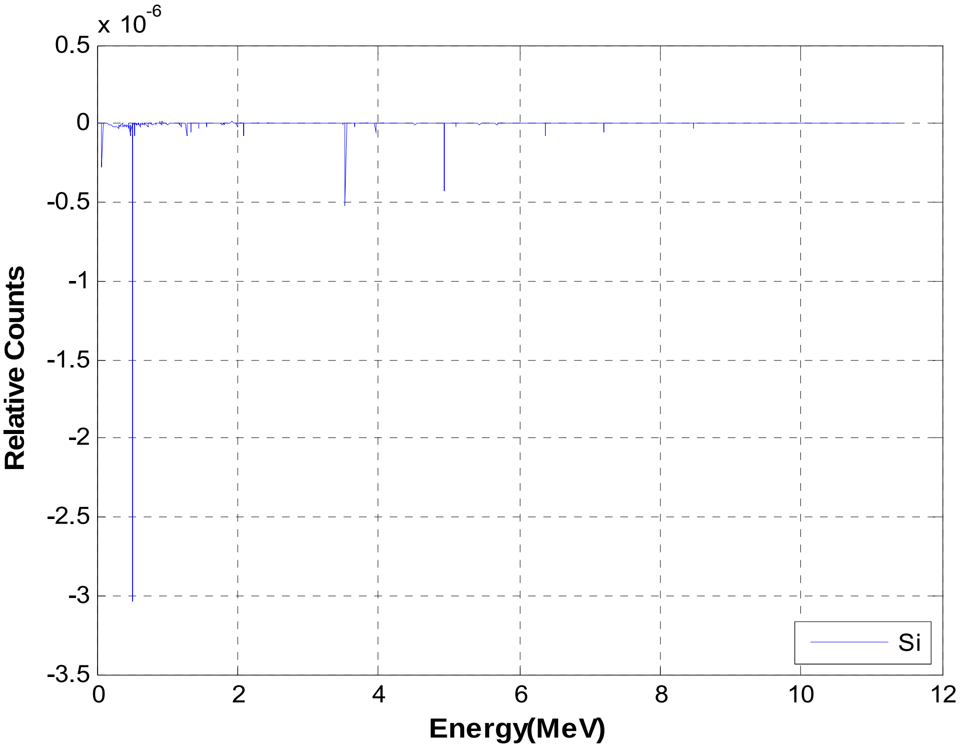

Figure 6-7 The CEARCPG calculated Si differential spectrum with respect to Hg perturbation

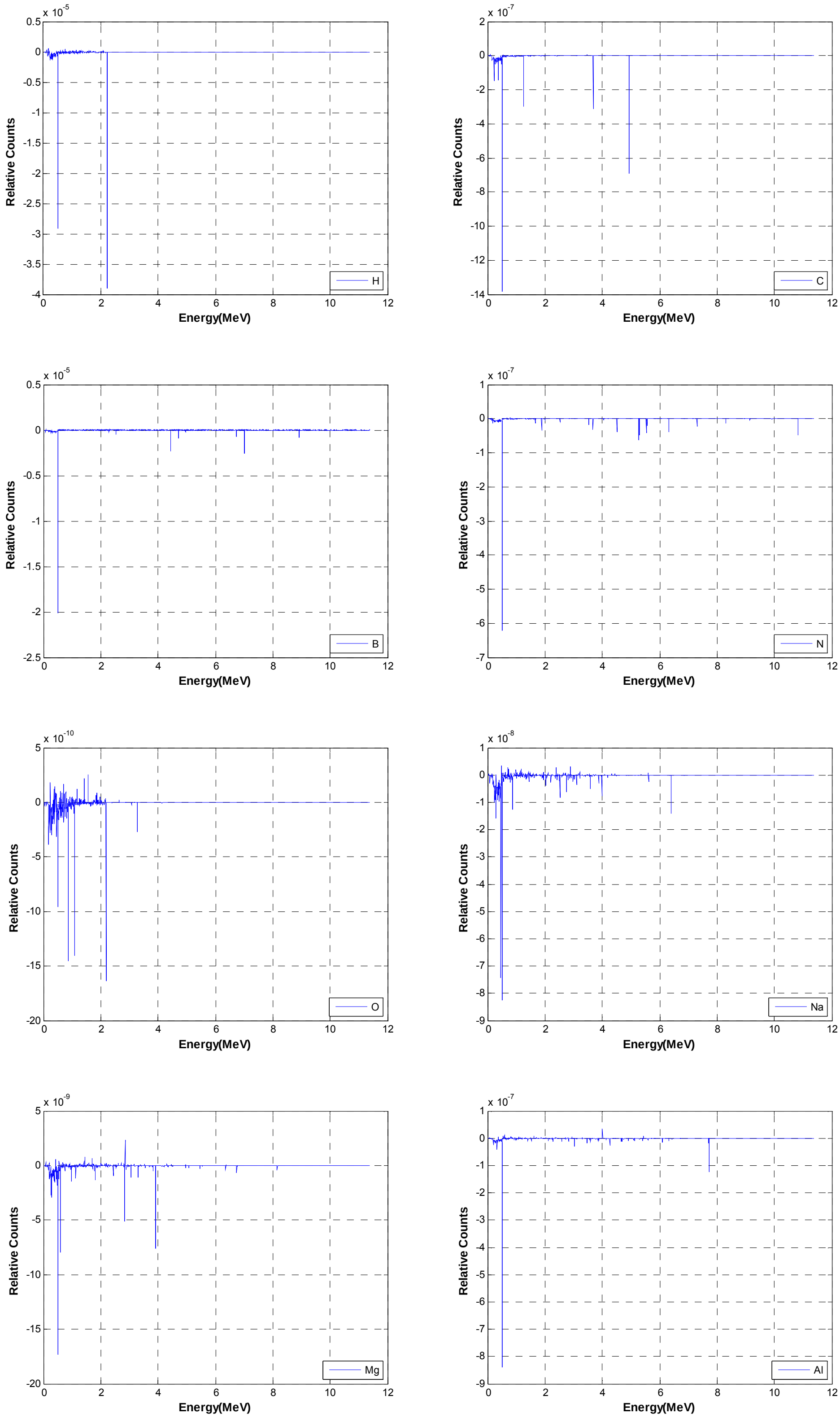

Figure 6-8 The other CEARCPG calculated differential spectrum with respect to Hg perturbation

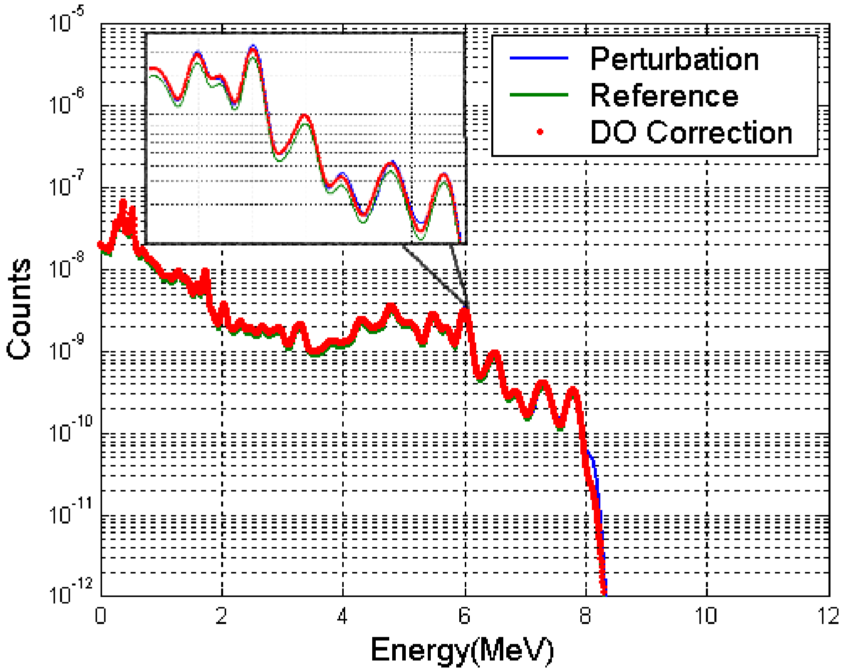

Figure 6-9 The calculated library spectra of mercury

7 CONCLUSIONS AND DISCUSSIONS

Prompt Gamma-Ray Neutron Activation Analysis (PGNAA) is a non-destructive, rapid on-line method for determination of the elemental composition of bulk coal and other granular solid samples. However, PGNAA has an inherently large background due to the neutron source, natural radioactivity and non-sample response. Introducing the gamma-gamma coincidence technology into PGNAA could highly suppress all interferences and eliminate some entirely. To overcome or alleviate the main drawback of coincidence PGNAA, which is a low coincidence counting rate, the system has to be optimized. This optimization at present relies on Monte Carlo simulation. The CEARCPG specific purpose code is the first and only code that is now available to simulate the normal and coincidence spectra of PGNAA. The MCNP5 code has been used in parameter study, dose rate and other suitable parts of this work.

To achieve a better accuracy and efficiency, the detector response function (DRF) used in CEARCPG has been updated with DRFs that generated by a new code named CEARDRFs. CEARDRFs can generate relatively accurate detector response functions for cylindrical or rectangular NaI and BGO detectors. With empirical implements of scintillation detector nonlinearity, flat continuum adjustment and Gaussian broadening, the generated DRF has a very good agreement with experiment. Also, the generation of detector response function is hundreds of times faster than MCNP5, which is benefited from the hybrid empirical approaches. Also, CEARDRFs can be easily expanded to other type of scintillators such LaBr and LSO.

CEARCPG has also been modified to execute on Linux clusters. Other improvements have been made to the code, including parallel and differential operator (DO) features. The parallel feature is accomplished by a simple script approach, which dramatically simplified the job to parallelize the code while keeping all the original features and could nearly reach the ideally linear speed-up feature. With derivatives to second order Taylor expansion, the DO has also been implemented into CEARCPG, including the consideration of collision, transportation and variance reduction kernels. A preliminary validation has been done to show that DO could be used to correct the library spectra without running simulation again.

With all the improvements to Monte Carlo simulation codes, the coincidence PGNAA could be optimized. It has been shown in two cases, lab size sample and large sample that similar to bulk coal sample on conveyor belt. Also, with proper shielding, the dose rate around the analyzer is pretty low.

For lab size samples, simply changing the paraffin moderator to 7.3 cm instead of 13 cm could have a ratio of increase (ROI) of 4.3 and 3.4 in single response and coincidence response, respectively; rearranging the two 6”x6” cylindrical NaI detectors to left-right sides of the sample with neutron source on top could gain the ROI of 6.9 and 13.0; further replacing the detectors with two 2”x4”x16” slab NaI detectors could gain the ROI of 66.5 and 223.7. All ROI are based on comparison with the original coincidence setup. Another important improvement is higher efficiency for higher energy gamma-rays in the last setup, although the detector is thinner and has smaller detection volume than the 6”x6” NaI detector. This is very promising, because prompt gamma-rays could reach as high as 11 MeV.

For large size samples, the self-moderation of the bulk coal is sufficient to thermalize neutrons from ^{252}Cf source. A new detector choice, a plastic scintillation detector, has been investigated to utilize its large volume and excellent time resolution. Coincidence technology could overcome its drawback of no peak property. Three setups have been investigated, including two 6”x6” cylindrical NaI detectors under the large sample with neutron source on top, two 2”x4”x16” slab NaI detectors under the large sample with neutron source on top and a special setup utilizing a 70cm x 50cm x 10cm plastic detector as a trigger to a 6”x6” cylindrical NaI detector. The simulation results show replacing the two 6”x6” cylindrical detectors with two 2”x4”x16” slab NaI detectors could gain the ROI of 1.6 and 6.2 in single response and coincidence response, respectively and the special setup could gain the ROI of 2.5 and 1.7. The special setup has the potential to achieve the similar coincidence response by increasing the detector thickness to improve efficiency. It has also been found that the NaI detector in the special setup has a better efficiency to high energy gamma-rays in single response while the slab detectors setup has better efficiency to high energy gamma-rays in coincidence response. The simulated 2D coincidence spectra show the feasibility of using the plastic detector as a trigger to another detector that has better energy resolution.

Among all the interferences, the fission gamma-rays source remains the major one while the interference from the analyzer structural material still contributes significantly. Q-value projection on the 2D spectra could further suppress the interference. The MCLLS analysis on the Q-value projected spectra shows better accuracy than using the total coincidence spectra.

8 FUTURE WORKS

The main work needed to done in the future is to validate the results with benchmark experiments, although the accuracy of CEARCPG has already been proved with experiments in the past.

More efforts need to be made in nuclear data libraries, because the nuclear structure data libraries are still incomplete. The author is also looking for more angular correlations between prompt gamma-rays, as they are assumed to be isotropic at present.

New elemental analysis method is also need to be developed with elemental libraries, especially when the library spectra have multiple orders of magnitude of difference. The analysis method based on true 2D spectra is also needed as some information might have been lost in projection.

Other neutron sources like D-T generator are worth a look. The D-T generator is an electronic source that produces neutrons by accelerating deuterium ions onto a target that contains tritium; the resulting fusion reaction creates 14 MeV neutrons. It is easy to control and no gamma-rays from the source. Also, Californium is produced in very small quantities. Oak Ridge National Laboratory currently produces only about 0.25 grams of californium-252 per year The Research Institute for Atomic Reactors in Dmitrovgrad, Russia, is the only other facility that produces this radionuclide, and its production capacity is estimated at 0.025 grams per year.

The light transport in large size detector is also an interesting area to look.

REFERENCES

Agostinelli, S. et al., (2003), "GEANT4 - a simulation toolkit", Nucl. Instr. Meth. A. Vol. 506, pp. 250-303.

Amdahl, Gene, (1967), "Validity of the Single Processor Approach to Achieving Large-Scale Computing Capabilities", AFIPS Conference Proceedings (30), 483-485.

Anderson, D.L. et al., (1982), "Neutron-capture Prompt Gamma-ray Spectroscopy as a Quantitative Analytical Method", Neutron-capture Gamma-ray Spectroscopy and Related Topics, Inst. Phys. Ser. 62, Institute of Physics, London, 655-668.

ANS-6.1.1 Working Group, Battat, M. E., (1977), "American National Standard Neutron and Gamma-Ray Flux-to-Dose Rate Factors", ANSI/ANS-6.1.1-1977 (N666), American Nuclear Society, LaGrange Park, Illinois.

Arinc, F., Gardner, R.P., Wielopolski, L., and Stiles, A.R., (1975), "Applications of the least-squares method to the analysis of XRF spectral intensities from atmospheric particulates collected on filters", Advances in X-ray Analysis, 19, pp. 367-380.

Berger, M. J. and Seltzer, S. M., (1972), Nuclear Instruments and Methods, 104,317-322.

Bozkurt, A., Chao, T.C. and Xu, X.G., (2000), "Fluence-to-dose conversion coefficients from monoenergetic neutrons below 20Mev based on the VIP-Man anatomical model", Phys. Med. Biol. 45 3059-3079.

Brown B.F., et al., (2004), "Monte Carlo Parameter Studies and Uncertainty Analyses with MCNP5", PHYSOR 2004 -The Physics of Fuel Cycles and Advanced Nuclear Systems: Global Developments Chicago, Illinois, April 25-29.

Clark, T. C., Gardner, R. P., and Verghese, K., (1982), "A Monte Carlo Model for In-Situ Prompt Gamma-Ray Analysis Probs", Nucl. Instru. Methods, 193, 365.

Demanins, F. and Raicich, F., (1992), “Excited States in ^{93}Nb”, Il Nuovo Cimento, 105, 245.

Demanins F. and Raicich, F., (1994), “Level and Decay Scheme of ^{141}Pr by means of the (n,n.γ) and (n,n. γ-γ) Reactions”, Il Nuovo Cimento, 107, 2727.

Ehmann, W.D., Vance, D.E., (1991), “Radiochemistry and Nuclear Methods of Analysis”, Wiley-Interscience, New York, pp. 302-303 (Chapter 9.6.4).

Ember, P. P., Belgya, T. and Molnar, G. L., (2002), “Improvement of the capabilities of PGAA by coincidence techniques”, Applied Radiation and Isotopes, Volume 56, Issue 3, Pages 535-541.

Ember, P. P., Belgya, T., Weil, J. L. and Molnar, G. L., (2004), “A practical test of a γ-γ coincidence measurement setup for PGAA”, Nuclear Instruments and Methods in Physics Research Section B: Beam Interactions with Materials and Atoms, Volume 213, Pages 406-409.

Frank, B.C. et al, (2005), “ITS Version 5.0: The Integrated TIGER Series of Coupled Electron/Photon Monte Carlo Transport Codes with CAD Geometry”, SAND2004-5172.

Gardner, R.P., El-Sayyed, E.S., Zheng, Y., Hayden, S. and Mayo, C.W., (2000), “NaI Detector Neutron Activation Spectra for PGNAA Application”, Appl. Radiat. Isotopes, 53, 483.

Gardner, R.P., Mayo, C.W., El-Sayyed, E.S., Metwally, W.A., Zheng, Y. and Poezart, M., (2000), “A feasibility study of a coincidence counting approach for PGNAA applications”, Applied Radiation and Isotopes, Volume 53, Issues 4-5, Pages 515-526.

Gardner, R.P., Metwally, W.A., Han, X. and Mayo, C.W., (2004), “Q-Value Summing for Coincidence Prompt Gamma-Ray Neutron Activation Analysis", Transactions of the American Nuclear Society, Volume 91, pp. 881-882.

Gardner, R.P., Sood, A., Wang, Y.Y., Liu, L., Guo, P. and Gehrke, R.J., (1997), “Single Peak Versus Library Least-Squares Analysis Methods for the PGNAA Analysis of Vitrified Waste”, Applied Radiation and Isotopes, Vol. 48, No. 10-12, pp.1331-1335.

Gardner, R.P., and Sood, A, (2004), “A Monte Carlo Simulation Approach for Generating NaI Detector Response Functions (DRF's) that Accounts for Nonlinearity and Variable Flat Continua”, Nuclear Instruments and Methods B, pp. 87-99.

Gardner, R.P., (2005), “Detector Response Function Status and Needs”, Transactions of the American Nuclear Society, Vol. 93, pp. 423-424.

Gardner, R.P., Xu, L. and Wang, J., (2007), “Some Lessons Learned From Mcnp Usage”, SPWLA 48th Annual Logging Symposium, June 4-7.

Greenwood, R.C., (1979), “Practical Applications of Neutron Capture Gamma Rays”, Proc. Third Int. Sysp. Neutron-capture Gamma-ray Spectroscopy and Ralated Topics, Plenum, New York, 441-460.

Gladney, E.S. et al, (1979), “A Literature Survey of Chemical Analysis by Thermal Neutron-induced Capture Gamma-ray Spectroscopy”, Los Alamos Scientific Laboratory Report LA-8023-MS.

Glascock, M.D., (1984), “A Literature Survey of Elemental Analysis by Neutron-induced Prompt Gamma-ray Spectroscopy and Related Topics”, University of Missouri Report, Columbia.

Guo, P., (1997), “CEARPGA User's Guide”, Center for Engineering Application of Radioisotopes.

Guo, W., (2003), “Improving the MCLLS Method Applied to the In Vivo XRF Measurement of Lead in Bone by Using the Differential Operator Approach (MCDOLLS) and X-ray Coincidence Spectroscopy”, PhD Dissertation, North Carolina State University.

Guo, W., Gardner, R.P. and Metwally, W.A., (2004), “Preliminary Studies on K and L Coincidence Spectroscopy for Optimizing the in vivo XRF Measurement of Lead in Bone,” Nucl. Instru. Meth. B 213, p. 574.

Halbleib, J.A., Kensek, R.P., Mehlhorn, T.A., Valdez, G., Seltzer, S.M. and Berger, M.J., (1992), “ITS version 3.0: The Integrated TIGER Series of coupled electron/ photon Monte Carlo transport codes”, Report SAND91-1634, Sandia Nat. Labs.

Han, X., (2005), “Development of Monte Carlo Code for Coincidence Prompt Gamma-ray Neutron Activation analysis”, PhD Dissertation, North Carolina State University.

Han, X., and Gardner, R.P., (2005), “Status of an Inverse Approach for Normal and Coincidence PGNAA", Transactions of the American Nuclear Society, Vol. 93, pp. 493-495.

Han, X., Gardner, R.P. and Metwally, W.A., (2007), “CEARCPG: A Monte Carlo Simulation Code for Normal and Coincidence Prompt Gamma-ray Neutron Activation Analysis (PGNAA)”, Nuclear Science and Engineering, 155 (1), 143-153.

Han, X., (2009), personal communication and CEAR internal report.

He, T., Gardner, R.P. and Verghese, K., (1990), “An Improved Si(Li) Detector Response Function”, Nuclear Instruments and Methods in Physics Research A299, pp. 354-366.

Heath, R.L., (1957), "Scintillation Spectrometry, Gamma-ray Spectrum Catalogue", 1st edition, USAEC Report IDO-16408.

Heath, R.L., (1964), "Scintillation Spectrometry, Gamma-ray Spectrum Catalogue", 2nd edition, 2 Volumes, USAEC Report IDO-16880.

Heath, R.L., (1974), "Gamma-ray Spectrum Catalogue, Ge (Li) Spectrometry" USAEC Report ANC-1000.

Hofstadter, R., (1948), Phys. Rev. 74 100.

Holloway, J.P. and Akkurt, H., (2004), “The fixed point formulation for large sample PGNAA—Part 1: theory”, Nuclear Instruments and Methods in Physics Research A 522, 529–544.

IAEA, (2006), Database for Prompt Gamma-ray Neutron Activation Analysis, http://www-nds.iaea.org/pgaa/pgaa7/index.html

Jakubek, J. et al., (1998), “Coindence gamma gamma spectroscopy system for instrumental neutron activation analysis”, Nucl. Instrum. Methods A 414, 261-264.

Jin, Y., Gardner R.P. and Verghese, K., (1986), “A Semi-Empirical Model for the Gamma-Ray Response Function of Germanium Detectors Based on Fundamental Interaction Mechanisms”, Nuclear Instruments and Methods in Physics Research, A242, 416-426.

Jokovic, D.R. et al., (2009), “Monte Carlo simulations of the response of a plastic scintillator and an HPGe spectrometer in coincidence”, Applied Radiation and Isotopes, 67, 719–722.

Jungclaus, A., Casten, R.F., Gill, R.L. and Borner, H.G., (1994), “Levels in ^{168}Er above 2 MeV and the onset of Chaos”, Physical Review C 49, 88.

Kahn, H, (1954), “Application of Monte Carlo”, USAEC Report AECU-3259, Rand Corporation.

Katz, L. and Penfold, A.S., (1952), Reviews of Modern Physics, 24, 28.

Kawrakow, I. and Rogers, D. W. O., (2000), “The EGSnrc Code System: Monte Carlo simulation of electron and photon transport”, Technical Report PIRS-701, National Research Council of Canada, Ottawa, Canada.

Kim, J.I. and Hoste, J., (1965), “Non-destructive Neutron Activation Determination of Silver and Antimony in Bismuth by gamma-gamma Coincidence Spectrometry”, Analytica. Chimica. Acta 33, 449-458.

Kim J.I. et al., (1965), “Neutron Activation Analysis of Copper in Bismuth by gamma-gamma Coincidence Measurement”, Analytica Chimica Acta 33, 123-130.

Knoll, G. F., (2000), “Radiation detection and measurement”, Wiley, New York.

Koeberl, C. and Huber, H., (2000), “Optimalization of the multiparameter g-g coincidence spectrometry for the determination of iridium geological materials”, J. Radioanal. Nucl. Chem 244, 655-660.

Lee, M.C., Verghese, K. and Gardner, R.P., (1987), “A Semiempirical Detector Response Function for 0.06- to 6.1-MeV Gamma Rays”, Transactions of the American Nuclear Society, Vol. 55, 555-557.

Lee, S.H., (2000), “Use of Differential Operators in the Monte Carlo Library Least – Square Method for X-ray Fluorescence Analysis,” PhD Dissertation, North Carolina State University.

Li, F., (2008), “Monte Carlo Simulation of Energy-Dispersive X-Ray Fluorescence and Applications”, PhD Dissertation, North Carolina State University.

Lindstrom, R.M. et al., (1994), “Analytical Applications of Cold Neutron Capture and Opportunities for Nuclear Physics”, Capture Gamma-ray Spectroscopy and Related Topics, World Scientific, Singapore, 955-961.

Lindstrom, R.M. et al., (1997), “Analytical Applications of Neutron Capture Gamma Rays”, Proc. 9th Int. Capture Gamma-ray Spectroscopy and Related Topics, Springer, Budapest, 693-704.

Luca, A., De Felice, P., Tanase, G., (2000), “Low level gamma spectrometry by beta-gamma coincidence”, Applied Radiation and Isotopes 53, 221-224.

MacFarlane, R. E., (1994), Rept. No.LA-12740-M, Los Alamos, N.M.

Mckinney, G., (1984), “A Monte Carlo (MCNP) Sensitivity Code Development and Application,” M.S. Thesis, University of Washington.

Metwally, W.A., Gardner, R.P. and Mayo, C.W., (2004), “Elemental PGNAA Analysis Using Gamma Gamma Coincidence Counting with the Library Least-Squares Approach,” Nucl. Instrum. Methods Phys. Res. B, 213, 394.

Medeiros J. et al., (2001), “Decay of ^{72}Ga”, Applied Radiation and Isotopes 54 245-259.

Meyer, G., Piccot, S., Rocchia, R., Toutain, J.P.J., (1993), “Simultaneous determination of Ir and Se in K-T boundary clays and volcanic sublimates”, Radioanal. Nucl. Chem. 168, 125-131.

Meyer, G., (1987), “Multiparameter coincidence spectrometry applied to the instrumental activation analysis of rocks and minerals”, Radioanal. Nucl. Chem. 114, 223-230.

Mickael M., Gardner R. P., and Verghese K., (1988), “McDNL: A New Specific Purpose Monte Carlo Code for Simulation of Dual Spaced Neutron Porosity Logs”, SPWLA 29th Annual logging Symposium, San Antonio, TX.

Molnar, G. and Lindstrom, R.M., (1998), “Nuclear Methods in Mineralogy and Geology”, Plenum Press, New York, London, pp. 145-164 (Chapter 3).

Moon, C.B. et al., (2001), “Level Structure of ^{120}Cs”, Nuclear Physics A 696 45-63.

National Academy of Sciences, (2008), “Radiation source use and replacement: Abbreviated Version”, Washington, DC, The National Academies Press.

NCRP Scientific Committee 4 on Heavy Particles, Rossi, H.H., (1971), “Protection Against Neutron Radiation”, NCRP-38, National Council on Radiation Protection and Measurements.

Olhoeft, J.E., (1962), “The Doppler Effect for a Non-Uniform Temperature Distribution in Reactor Fuel Elements”, WCAP-2048, Westinghouse Electric Corporation, Atomic Power Division, Pittsburgh.

Pages, L. et al, (1972), “Energy loss, range, and bremsstrahlung yield for 10-keV to 100-MeV electrons in various elements and chemical compounds, Atomic Data and Nuclear Data Tables”, Volume 4, Pages 1-27.

Pallone, A.K. and Demaree, J.D., (2009), **“**CASSPERR: A γ–γ cascade detectorfor resonant nuclear reaction analysis”, Nuclear Instruments and Methods in Physics Research Section B: Beam Interactions with Materials and Atoms, Volume 267, Issue 17, Pages 2927-2933.

Paul, R.L. et al., (2000), “Prompt Gamma-ray Activation Analysis: Fundamental and Applications”, J. Radioanal. Nucl. Chem. 243, 181-189.

Peplow, D.E., Gardner, R.P. and Verghese, K., (1994), “Sodium Iodide Detector Response Functions Using Simplified Monte Carlo Simulation and Principal Components”, Nuclear Geophysics, Vol. 8, No. 3, pp. 243-259.

Rief, H., (1984), “Generalized Monte Carlo Perturbation Algorithms for Correlated Sampling and a Sceond-Order Taylor Series Approach”, *Ann. Nucl. Energy* 11, 455.

Rief, H., (1994), “A Synopsis of Monte Carlo Perturbation Algorithms”, Journal of Computational Physics, 111, pp. 33-48.

Rooney, B.D. and Valentine, J.D., (1997), “Scintillator light yield non-proportionality: calculating photon response using measured electron response”, IEEE Trans. Nucl. Sci. 43 (3) 1271.

Shultis, J.K. and Faw, R.E., (2000), “Radiation shiledling”, Amer Nuclear Society.

Shyu, C.M., He, T., Verghese, K. and Gardner, R.P., (1988), “Monte Carlo-library least-squares principle for nuclear analysers”, Transactions of the American Nuclear Society, Suppl. 3, 56, 4446.

Shyu, C.M., (1991), “Development of Monte Carlo Library Least-Square Method of Analysis for Neutron Capture Prompt Gamma Ray Analyzer”, PhD Dissertation, North Carolina State University.

Shyu, C.M., Gardner, R.P. and Verghese, K., (1993), “Development of the Monte Carlo library least-squares method of analysis for neutron capture prompt gamma-ray analyzers”. Nuclear Geophysics 7(2), 241-268.

Siciliano, E.R. et al, (2005), “Comparison of PVT and NaI(Tl) scintillators for vehicle portal monitor applications”, Nucl. Instrum. Methods Phys. Res. A, 550, 647-674.

Tomlin, B.E., Zeisler, R. and Lindstrom, R.M., (2008), “γ-γ coincidence spectrometer for instrumental neutron-activation analysis”, Nuclear Instruments and Methods in Physics Research Section A: Accelerators, Spectrometers, Detectors and Associated Equipment, Volume 589, Issue 2, Pages 243-249.

Verbinski, V.V., Weber, H. and Sund, R.E., (1973), “Prompt Gamma Rays from ^{236}U(n,f), ^{239}Pu(n,f),and Spontaneous Fission of ^{252}Cf”, Phy. Rev. C, 7, 3.

Valentine, J.D. and Rooney, B.D., (1994), “Design of a Compton spectrometer experiment for studying scintillator non-linearity and intrinsic energy resolution”, Nucl. Instr. and Meth. A 353, 37.

Valentine, J.D., Rooney, B.D. and Li, J., (1998), “The light yield nonproportionality component of scintillator energy resolution”, IEEE Trans. Nucl. Sci. 45 (3) 512.

Wang, J. and Gardner, R.P., (2008), “Optimizing the Design of a Coincidence PGNAA System for Bulk Analysis”, Transactions of the American Nuclear Society, Vol. 99, pp. 45-46.

Wang, J., Calderon, A., Peeples, C.R., Ai, X. and Gardner, R.P., (2010), “Monte Carlo investigation and optimization of coincidence prompt gamma-ray neutron activation analysis” , Nuclear Instruments and Methods in Physics Research Section A: Accelerators, Spectrometers, Detectors and Associated Equipment, In Press.

Wang, Z., Speaker, D.P. and Gardner, R.P., (2008), “Two Monte Carlo Approaches for the Generation of Scintillation Detector Response Functions (DRF's)”, Transactions of the American Nuclear Society, Vol. 98, pp.585-586.

X-5 Monte Carlo Team, (2008), “MCNP — A General Monte Carlo N-Particle Transport Code, Version 5”, LA-UR-03-1987, Los Alamos National Laboratory.

Xu, L., (2006), “Prompt Gamma-ray Imaging for Small Animals”, PhD Dissertation, North Carolina State University.

Yacout, A.M., Gardner, R.P. and Verghese, K., (1986), “A Semi-Empirical Model for the X-Ray Si(Li) Detector Response Function”, Nuclear Instruments and Methods in Physics Research, A243, 121-130.

Zhang, W., (2003), “The Analog Linear Interpolation Approach for Monte Carlo Simulation of Prompt Gamma-Ray Neutron Activation Analysis”, PhD Dissertation, North Carolina State University

Zhang, W. and Gardner. R.P., (2004), “The analog linear interpolation approach for Monte Carlo simulation of PGNAA: The CEARPGA code”, Nuclear Instruments and Methods in physics Research B. 213, 116-123.

APPENDICES

Appendix A: Sample Input File of CEARCPG

```
C sample input for lab coal sample with 6x6NaI detectors under sample
    1     1  -11.34     -1  2  -4  5  -6  7
    2     1  -11.34     5  -4  -2  40  7  -6  8
    3     3  -0.001193  -8  -2  40
    4     2  -0.92      -3  10  13  -9  12  -11
    5     4  -1.185     -18  19  -13  14  21  -20
    6     4  -1.185     -14  16  19  -23  21  -20
    7     4  -1.185     22  -18  -14  16  -20  21
    8     4  -1.185     -16  17  19  -18  21  -20
    9     4  -1.185     21  -25  -14  16  23  -22
   10     4  -1.185     24  -20  16  -14  23  -22
   11     3  -0.001193  23  -22  -14  15  25  -24
   12     5  -2.076     23  -22  -15  16  25  -24
   13     6  -1.06      -26  27  -34
   14     8  -2.7       -27  28  -33
   15     8  -2.7       -28  29  -33  31
   16     7  -3.667     -28  -31  29
   17     1  -11.34     -34  42  29  -27
   18     6  -1.06      -26  27  -36
   19     8  -2.7       -27  28  -35
   20     8  -2.7       -35  32  -28  30
   21     7  -3.667     -28  -32  30
   22     1  -11.34     30  -27  41  -36
   23     3  -0.001193  -37  1  -39
   24     3  -0.001193  -39  -5  -1  3
   25     3  -0.001193  -39  4  -1  3
   26     3  -0.001193  -39  5  -4  6  -1  3
   27     3  -0.001193  -39  5  -4  -7  -1  3
   28     3  -0.001193  -39  -10  -3  13
   29     3  -0.001193  -39  9  -3  13
   30     3  -0.001193  -39  10  -9  11  -3  13
   31     3  -0.001193  -39  10  -12  -9  -3  13
   32     3  -0.001193  -39  -19  -13  17
   33     3  -0.001193  -39  18  -13  17
   34     3  -0.001193  -39  19  -18  20  -13  17
   35     3  -0.001193  -39  19  -21  -18  -13  17
   36     3  -0.001193  -39  -17  26
   37     3  -0.001193  -39  34  36  -26  38
   38     3  -0.001193  -34  38  -29
   39     3  -0.001193  -36  -30  38
   40     3  -0.001193  -39  -38
   41     3  -0.001193  39
   42     3  -0.001193  37  -39
   43     1  -11.34     -40  7  -6  3  5  -4
   44     6  -1.06      -41  35  -27  30
   45     6  -1.06      -42  33  -27  29
```

```
    1        pz       23.5
    2        pz         23
    3        pz       13.3
    4        px          5
    5        px         -5
    6        py          5
    7        py         -5
    8        cz       0.25
    9        px         24
   10        px        -24
   11        py       14.5
   12        py      -14.5
   13        pz          0
   14        pz       -1.3
   15        pz         -4
   16        pz      -10.7
   17        pz        -12
   18        px         28
   19        px        -28
   20        py          6
   21        py         -6
   22        px         27
   23        px        -27
   24        py        4.7
   25        py       -4.7
   26        pz      -17.5
   27        pz      -17.8
   28        pz     -18.18
   29        pz     -33.42
   30        pz     -33.41
   31       c/z        -14          0       7.62
   32       c/z         14          0       7.62
   33       c/z        -14          0          8
   34       c/z        -14          0       11.5
   35       c/z         14          0          8
   36       c/z         14          0       11.5
   37        pz         30
   38        pz        -50
   39        cz         50
   40        pz       17.5
   41       c/z         14          0        8.3
   42       c/z        -14          0        8.3

m1    82000             -1.0
m2    01001           -0.14669
      06000           -0.85331
m3    07014             -0.767
      08016             -0.233
m4    01000           -0.13587
      06000           -0.86413
```

```
m5    01001  -0.02892   06012   -0.7528  08016 -0.05487
      07014  -0.014     11023   -0.01121 13027 -0.0238
      14028  -0.01943   16032   -0.056   17000 -0.01729
      80000  -0.02168
m6    01001           -0.13568
      03006           -0.075    06000     -0.78932
m7    11023         -0.153373
      53127         -0.846627
m8    13027             -1
imp  1 1 1 1 1 1 1 1 1 1 1 1 1 1 1 1 1 1 1 1 1 1 1 1 1 1 1 1 1 1 1
     1 1 1 1 1 1 1 1 0 0 0 1 1 1
sdef   cf x=0.0  y=0.0  z=18  icel=3
nps    2000000
prdmp  10000
number_detector 2
detector  -14.0 0 -25.8  7.62  15.24  16
          12.73 0 -24.53 7.62  15.24  21
sample   12
c trunc cell=12
c pert cell=12 num=1 80000 Mode=1
wcut 1d-6 1d-7 1d-10 1d-11 0.02
spect    2048 512 0 0  0.0055575  18000  0.0055575 0.02223
detcoin 1 ( 16 : 21 )
```

Appendix B: Neutron Flux-to-Dose Rate Conversion Factors

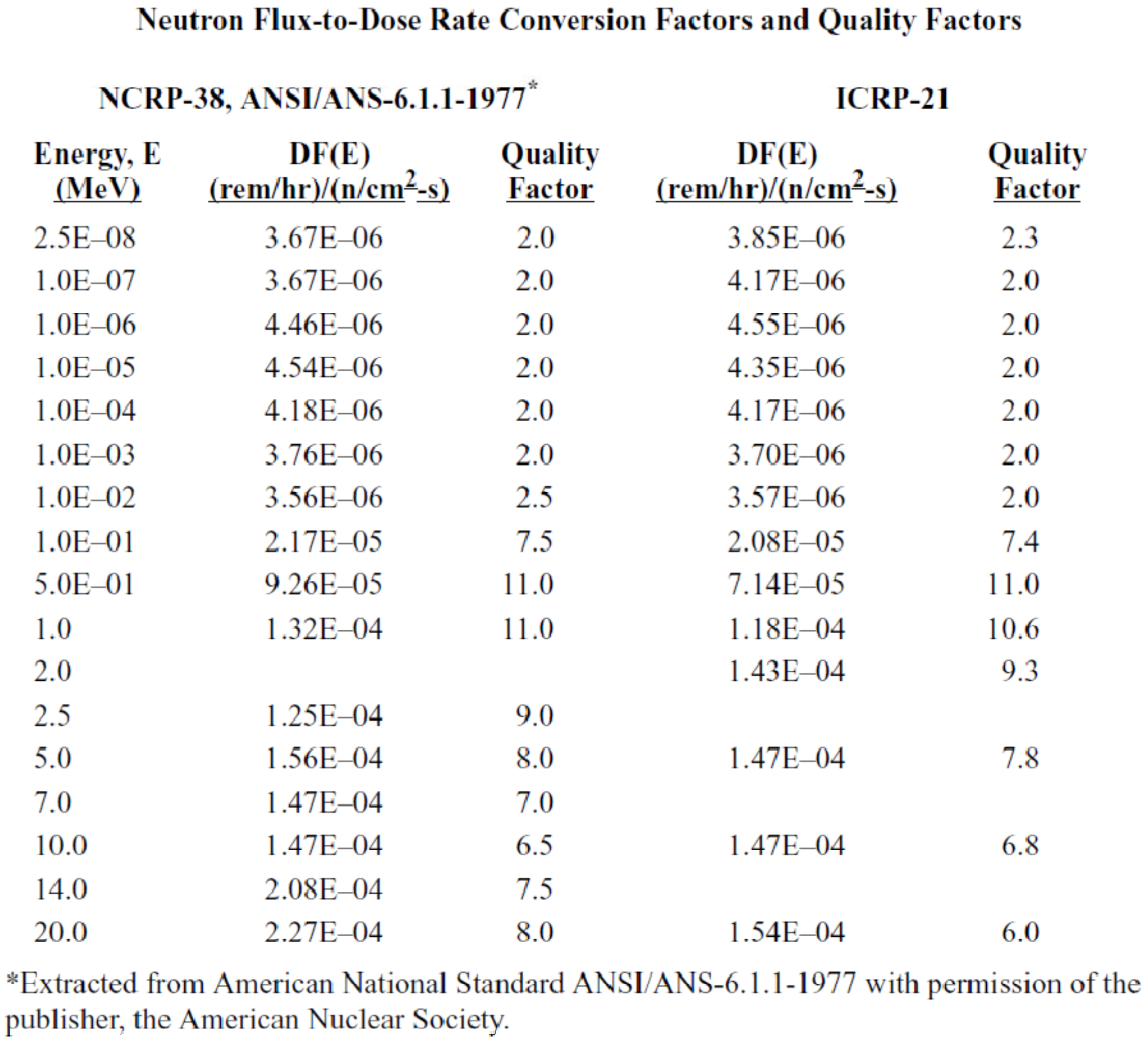

Neutron Flux-to-Dose Rate Conversion Factors and Quality Factors

NCRP-38, ANSI/ANS-6.1.1-1977*			ICRP-21	
Energy, E (MeV)	**DF(E) (rem/hr)/(n/cm^2-s)**	**Quality Factor**	**DF(E) (rem/hr)/(n/cm^2-s)**	**Quality Factor**
2.5E–08	3.67E–06	2.0	3.85E–06	2.3
1.0E–07	3.67E–06	2.0	4.17E–06	2.0
1.0E–06	4.46E–06	2.0	4.55E–06	2.0
1.0E–05	4.54E–06	2.0	4.35E–06	2.0
1.0E–04	4.18E–06	2.0	4.17E–06	2.0
1.0E–03	3.76E–06	2.0	3.70E–06	2.0
1.0E–02	3.56E–06	2.5	3.57E–06	2.0
1.0E–01	2.17E–05	7.5	2.08E–05	7.4
5.0E–01	9.26E–05	11.0	7.14E–05	11.0
1.0	1.32E–04	11.0	1.18E–04	10.6
2.0			1.43E–04	9.3
2.5	1.25E–04	9.0		
5.0	1.56E–04	8.0	1.47E–04	7.8
7.0	1.47E–04	7.0		
10.0	1.47E–04	6.5	1.47E–04	6.8
14.0	2.08E–04	7.5		
20.0	2.27E–04	8.0	1.54E–04	6.0

*Extracted from American National Standard ANSI/ANS-6.1.1-1977 with permission of the publisher, the American Nuclear Society.

Appendix C: Photon Flux-to-Dose Rate Conversion Factors

Photon Flux-to-Dose Rate Conversion Factors

ANSI/ANS–6.1.1–1977		ICRP-21	
Energy, E (MeV)	**DF(E) (rem/hr)/(p/cm^2-s)**	**Energy, E (MeV)**	**DF(E) (rem/hr)/(p/cm^2-s)**
0.01	3.96E–06	0.01	2.78E–06
0.03	5.82E–07	0.015	1.11E–06
0.05	2.90E–07	0.02	5.88E–07
0.07	2.58E–07	0.03	2.56E–07
0.1	2.83E–07	0.04	1.56E–07
0.15	3.79E–07	0.05	1.20E–07
0.2	5.01E–07	0.06	1.11E–07
0.25	6.31E–07	0.08	1.20E–07
0.3	7.59E–07	0.1	1.47E–07
0.35	8.78E–07	0.15	2.38E–07
0.4	9.85E–07	0.2	3.45E–07
0.45	1.08E–06	0.3	5.56E–07
0.5	1.17E–06	0.4	7.69E–07
0.55	1.27E–06	0.5	9.09E–07
0.6	1.36E–06	0.6	1.14E–06
0.65	1.44E–06	0.8	1.47E–06
0.7	1.52E–06	1.	1.79E–06
0.8	1.68E–06	1.5	2.44E–06
1.0	1.98E–06	2.	3.03E–06
1.4	2.51E–06	3.	4.00E–06
1.8	2.99E–06	4.	4.76E–06
2.2	3.42E–06	5.	5.56E–06
2.6	3.82E–06	6.	6.25E–06
2.8	4.01E–06	8.	7.69E–06
3.25	4.41E–06	10.	9.09E–06
3.75	4.83E–06		
4.25	5.23E–06		
4.75	5.60E–06		
5.0	5.80E–06		
5.25	6.01E–06		
5.75	6.37E–06		
6.25	6.74E–06		

Appendix D: 2D Coincidence Spectra for Common Elements in Coal

The lower and upper limits of display range (from light to dark) are noted in brackets.

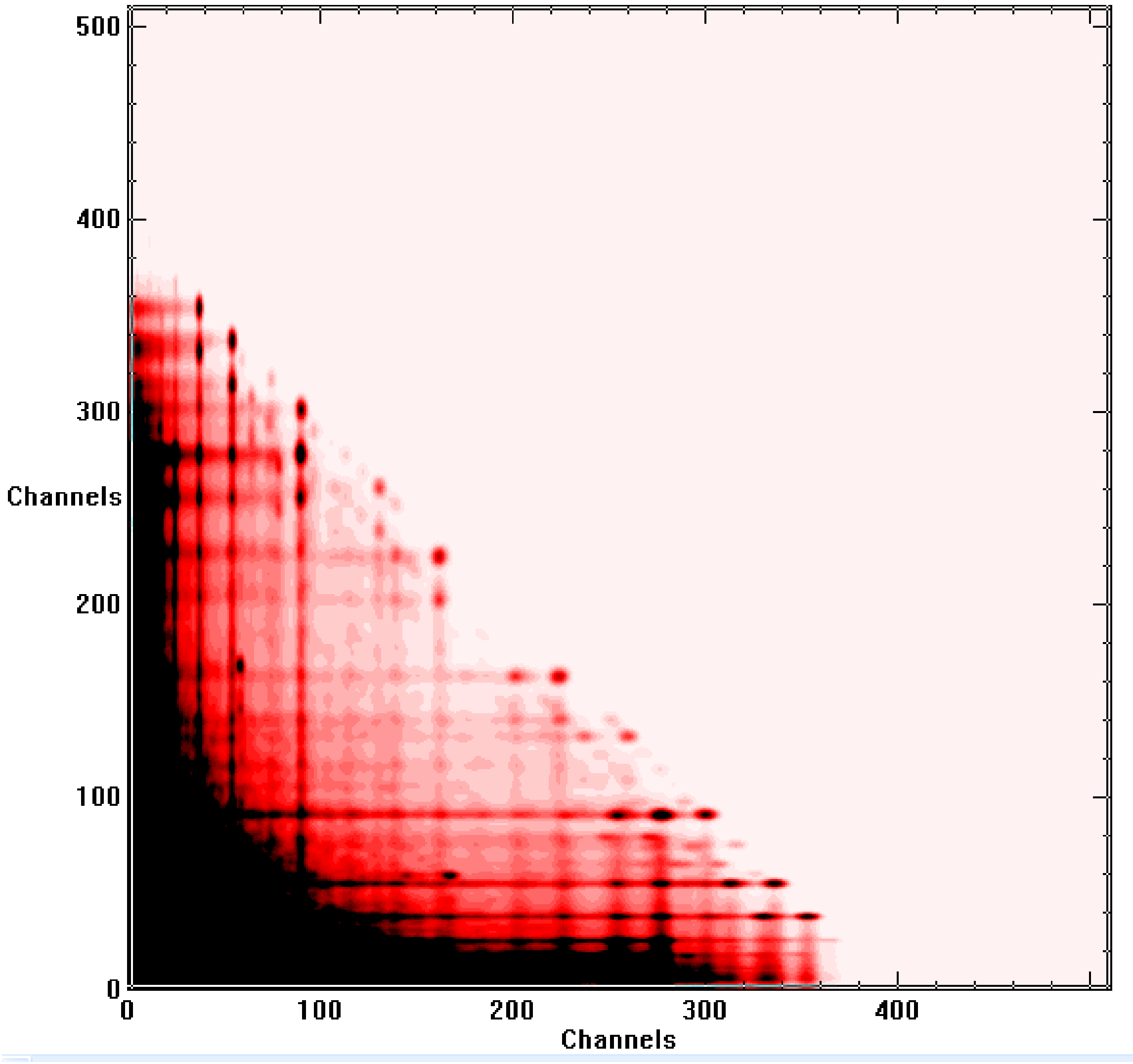

Total Coincidence (0-300000 counts)

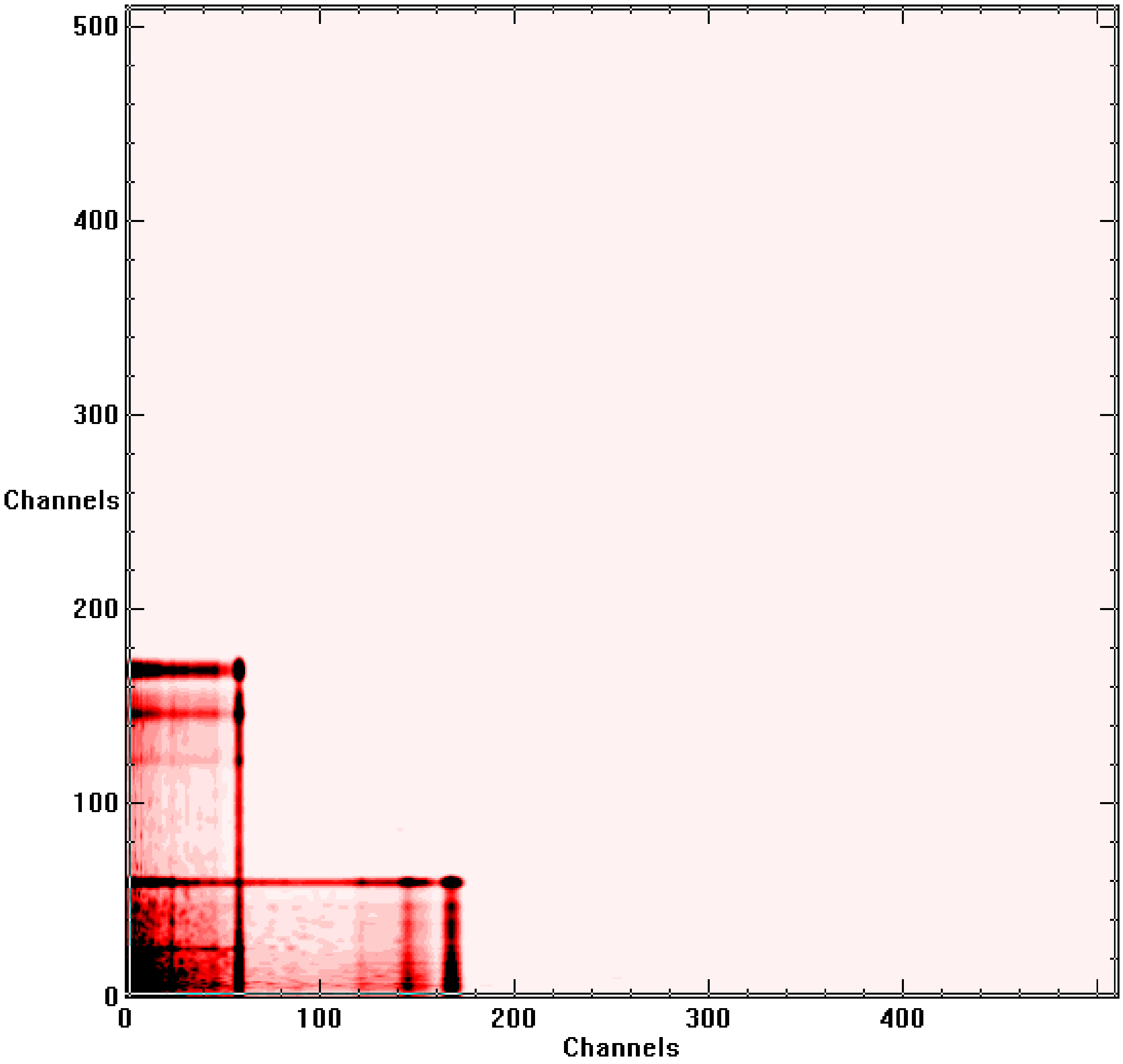

Coincidence from structural materials (0-30000 counts)

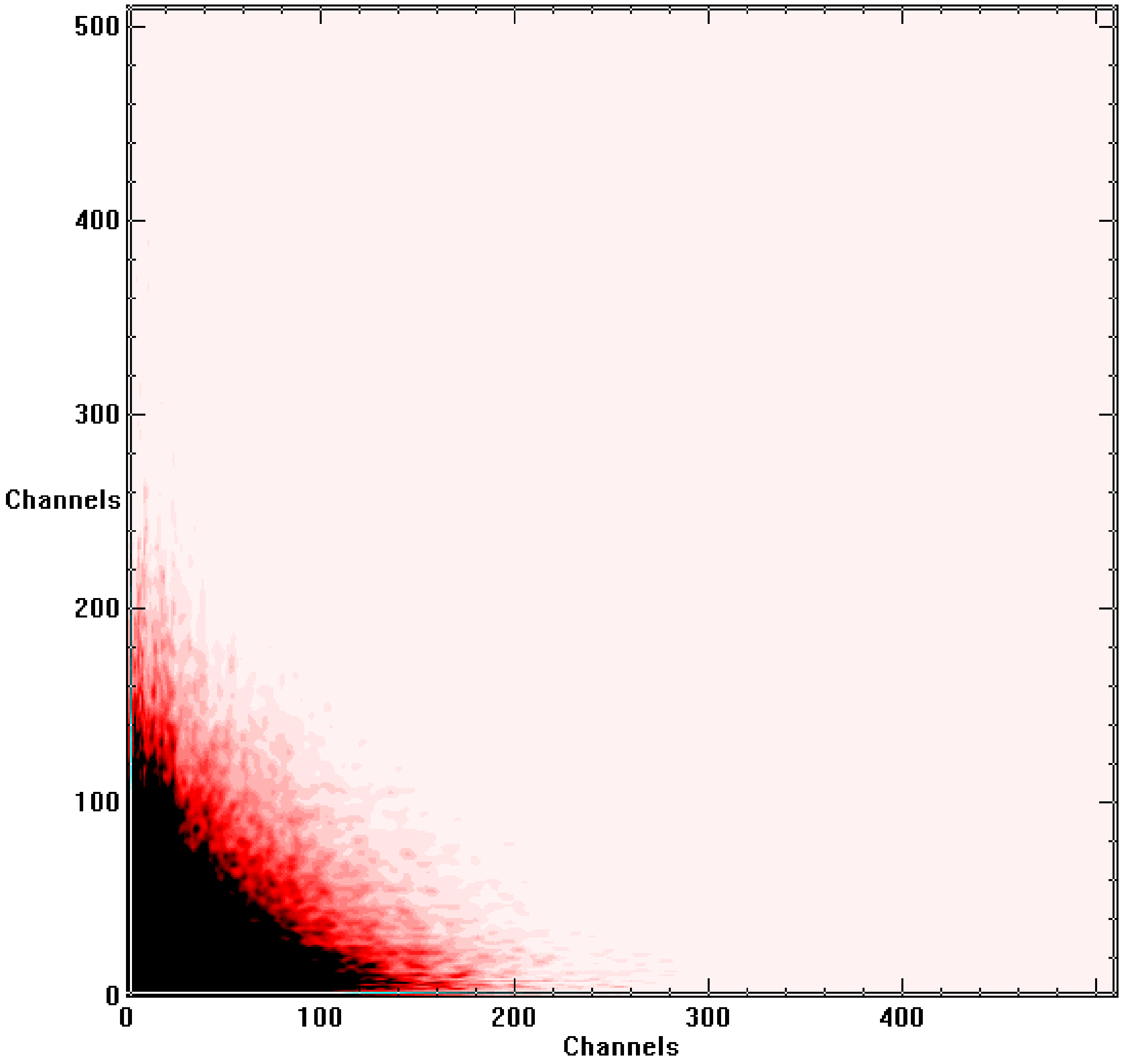

Fission Gamma Coincidence (0-300000 counts)

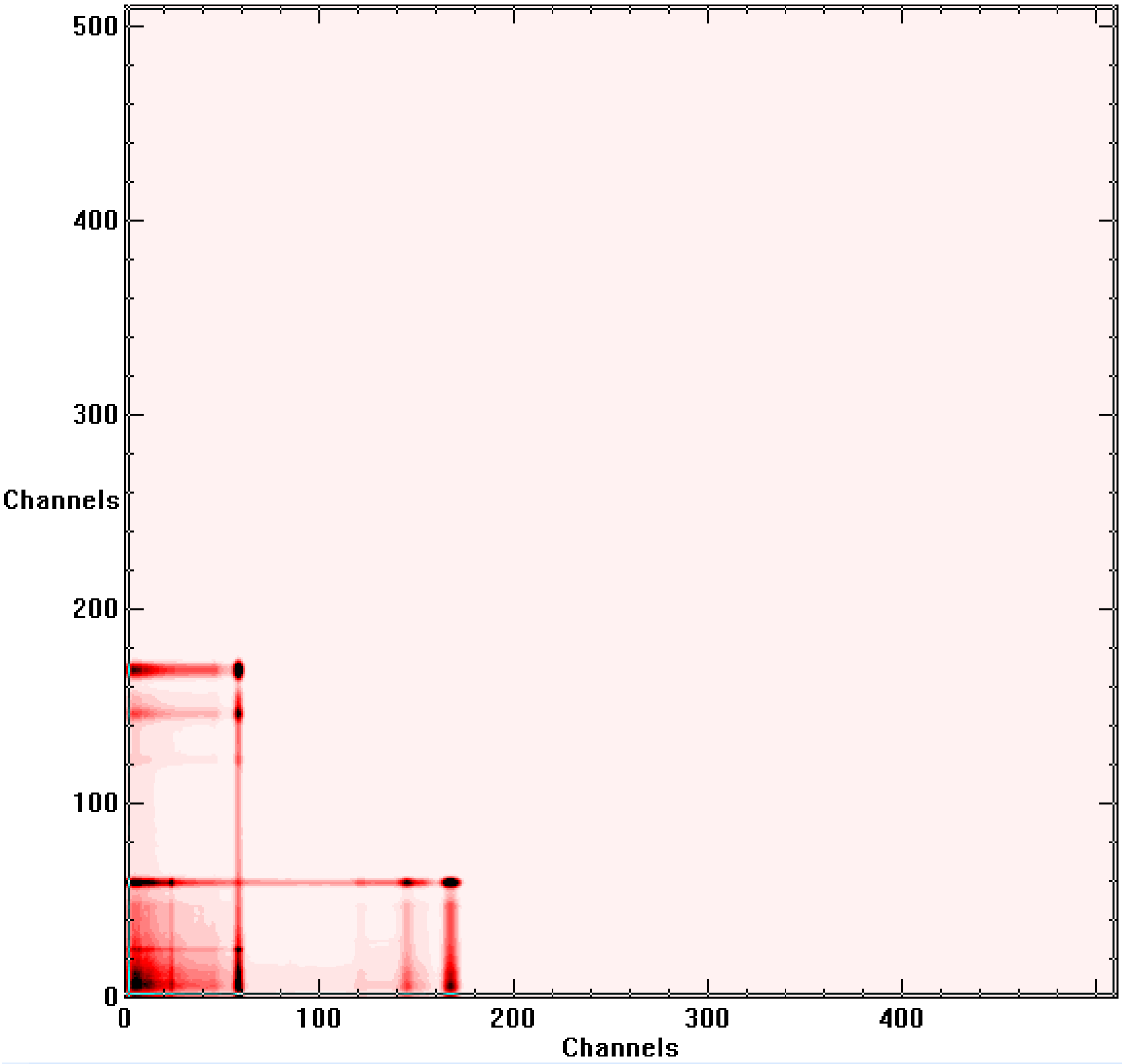

Coincidence from Carbon in Sample (0-30000 counts)

Q-Value: 4.946 MeV

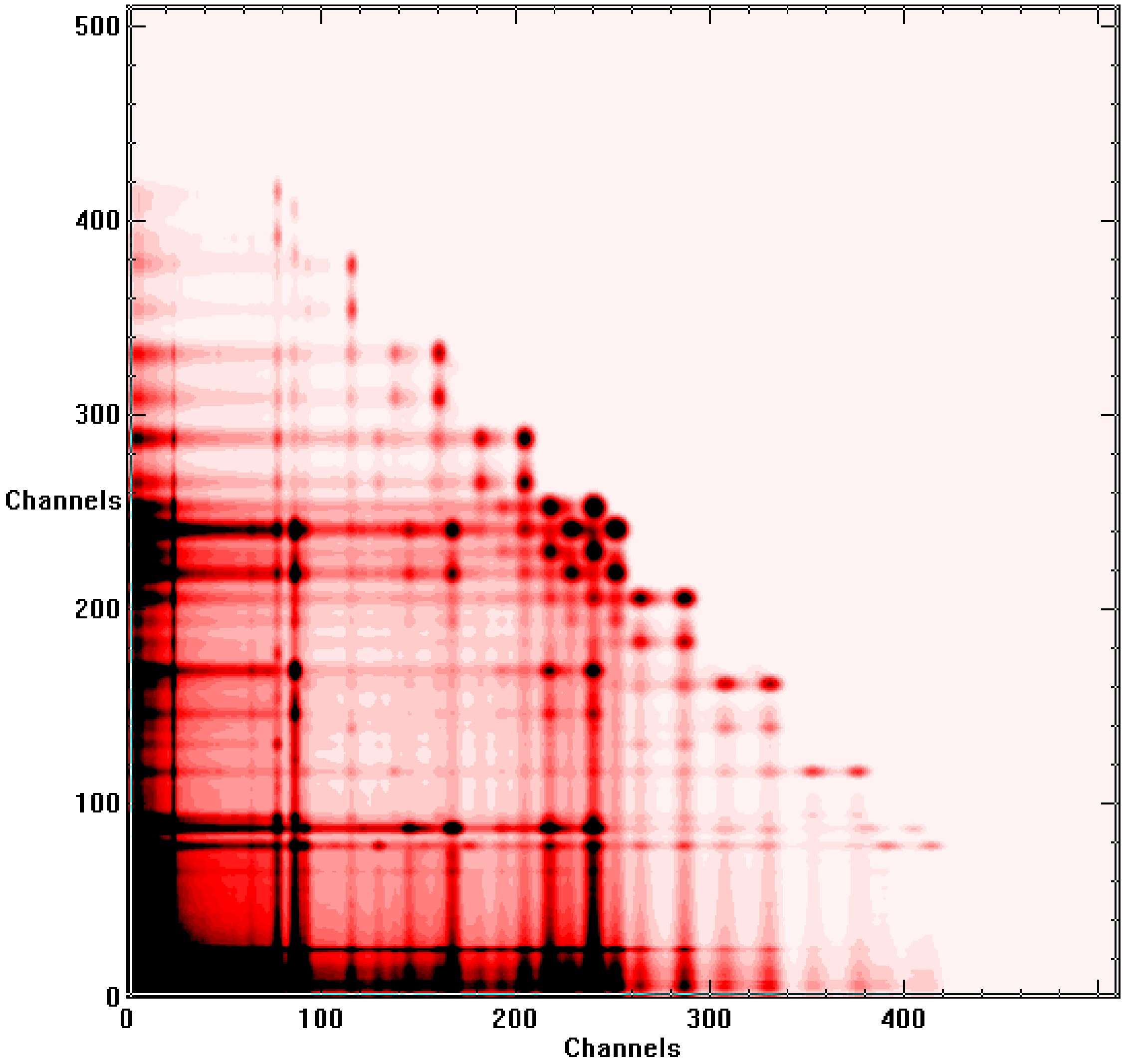

Coincidence from Nitrogen in Sample (0-3000 counts)

Q-Value: 10.833 MeV

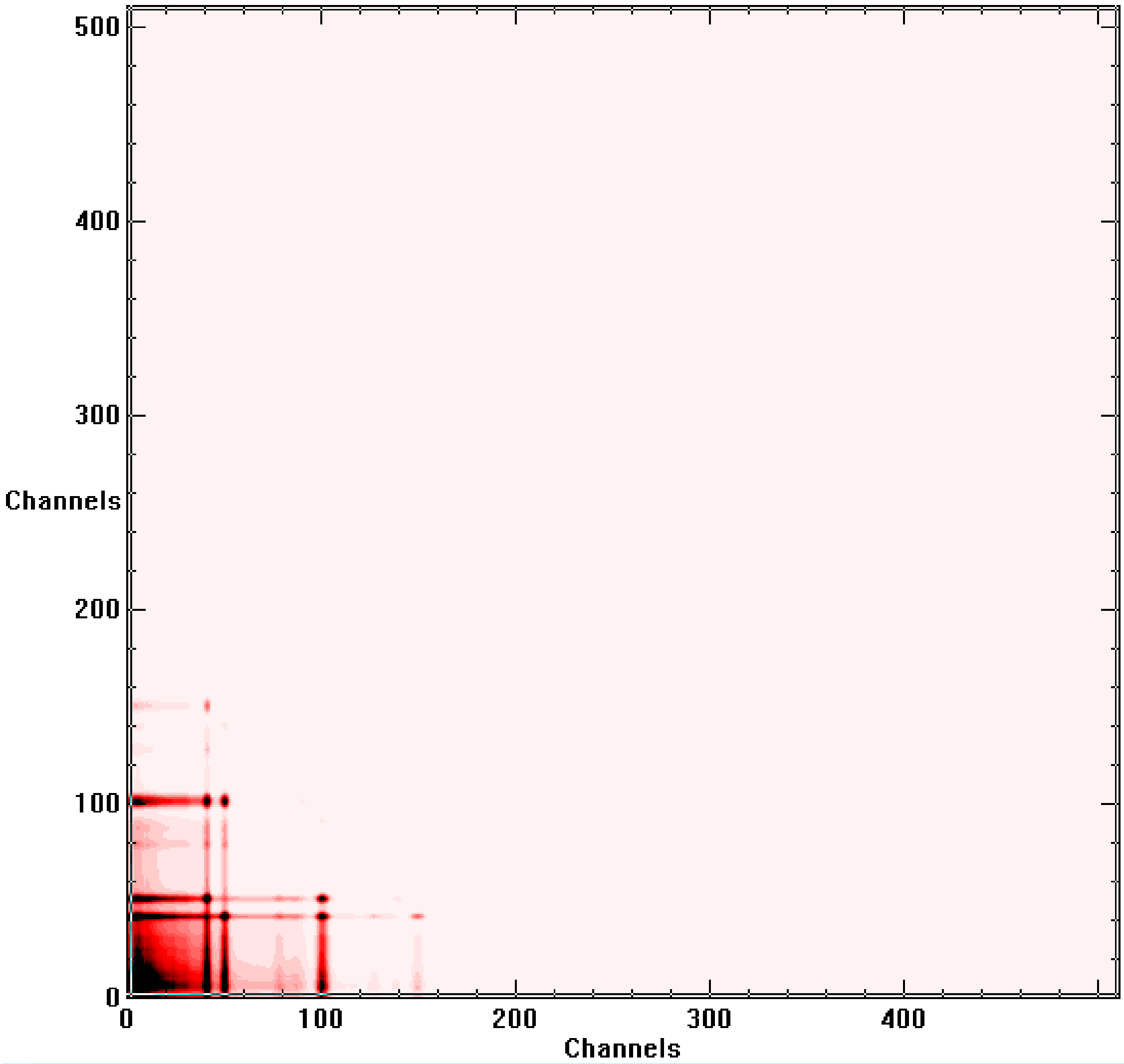

Coincidence from Oxygen in Sample (0-2000 counts)

Q-Value: 4.143 MeV

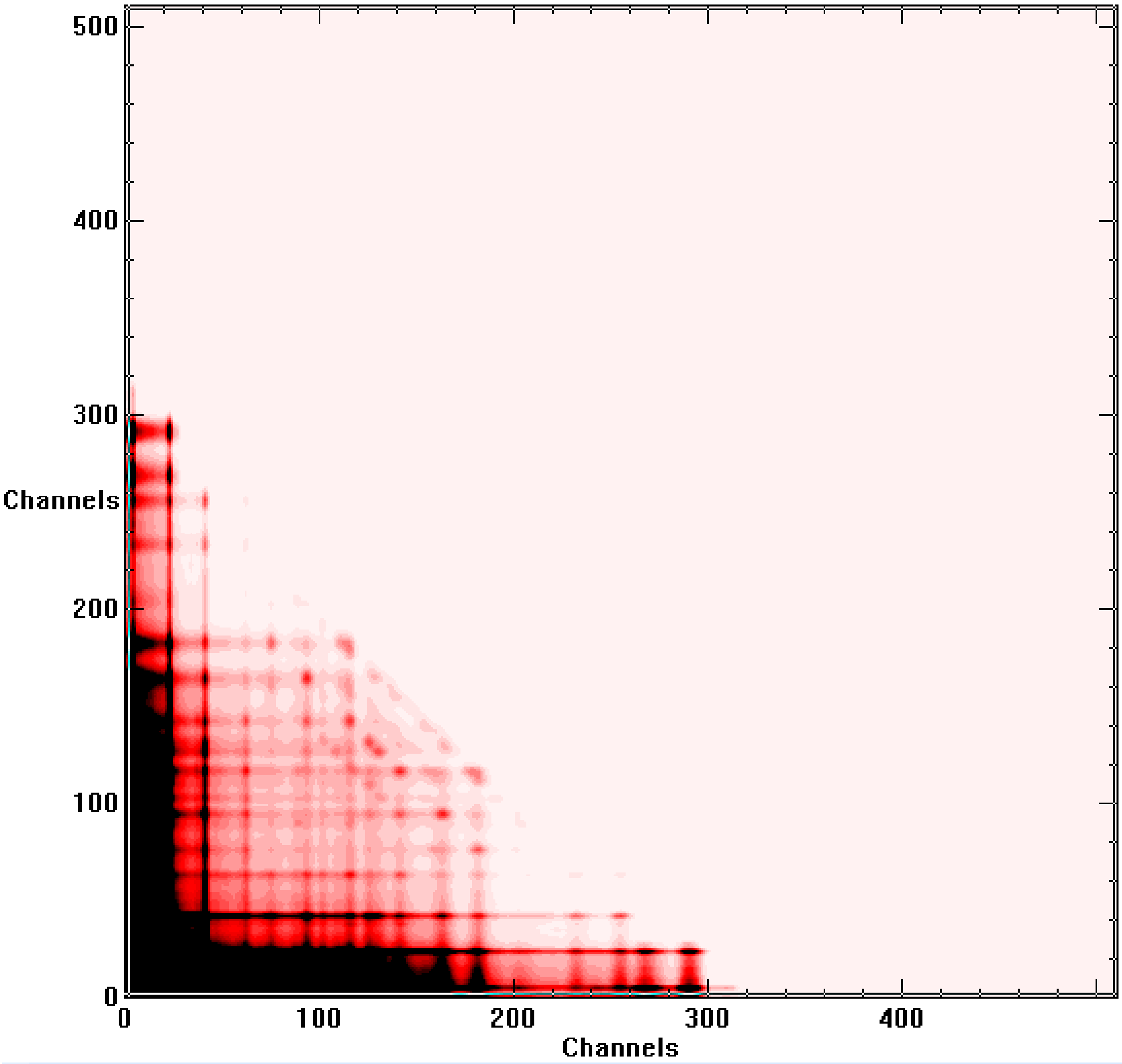

Coincidence from Sodium in Sample (0-3000 counts)

Q-Value: 6.959 MeV

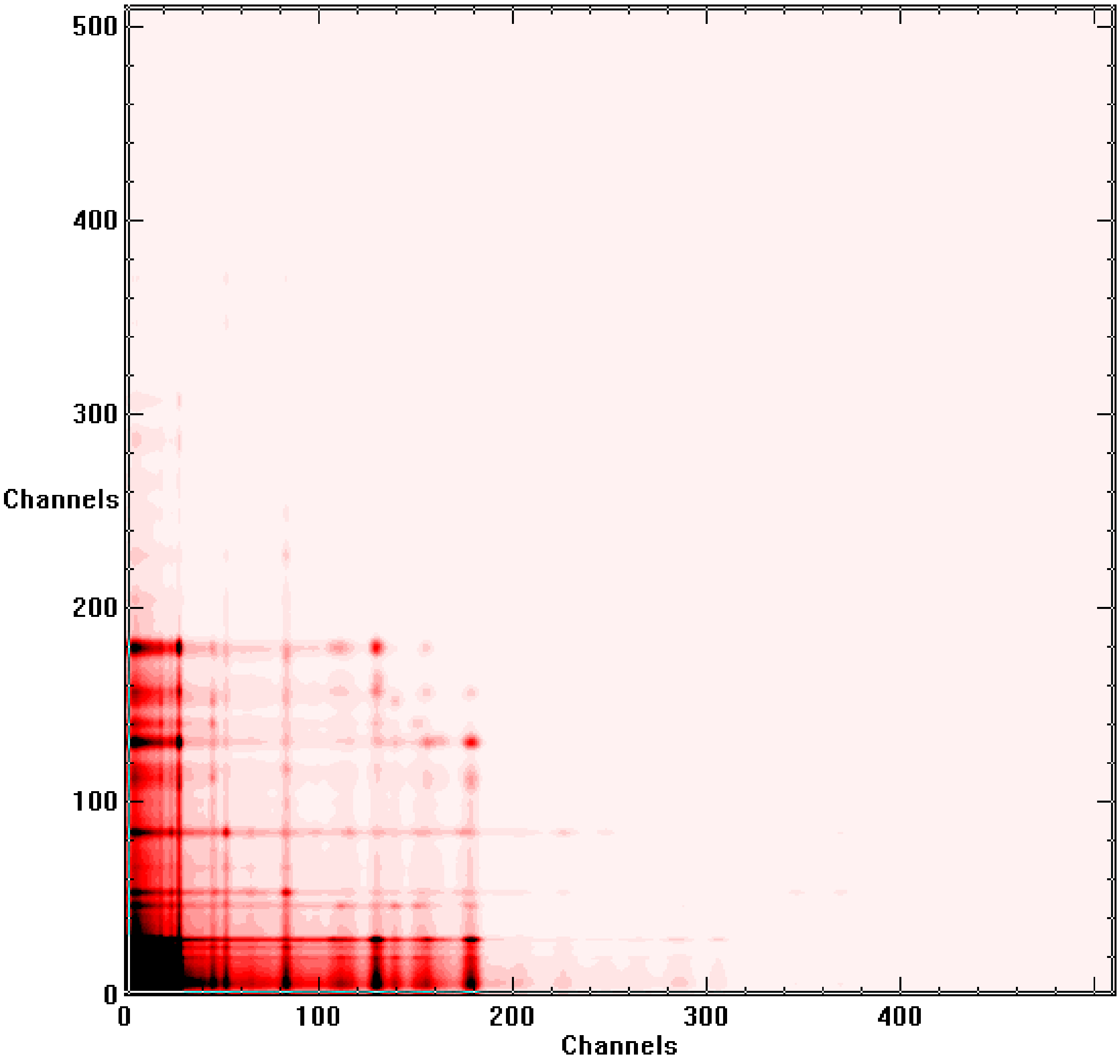

Coincidence from Magnesium in Sample (0-1000 counts)

Isotopes	Abundance (%)	Q-Value(MeV)
Mg-24	78.99	7.329
Mg-25	10.00	11.090
Mg-26	11.01	6.442

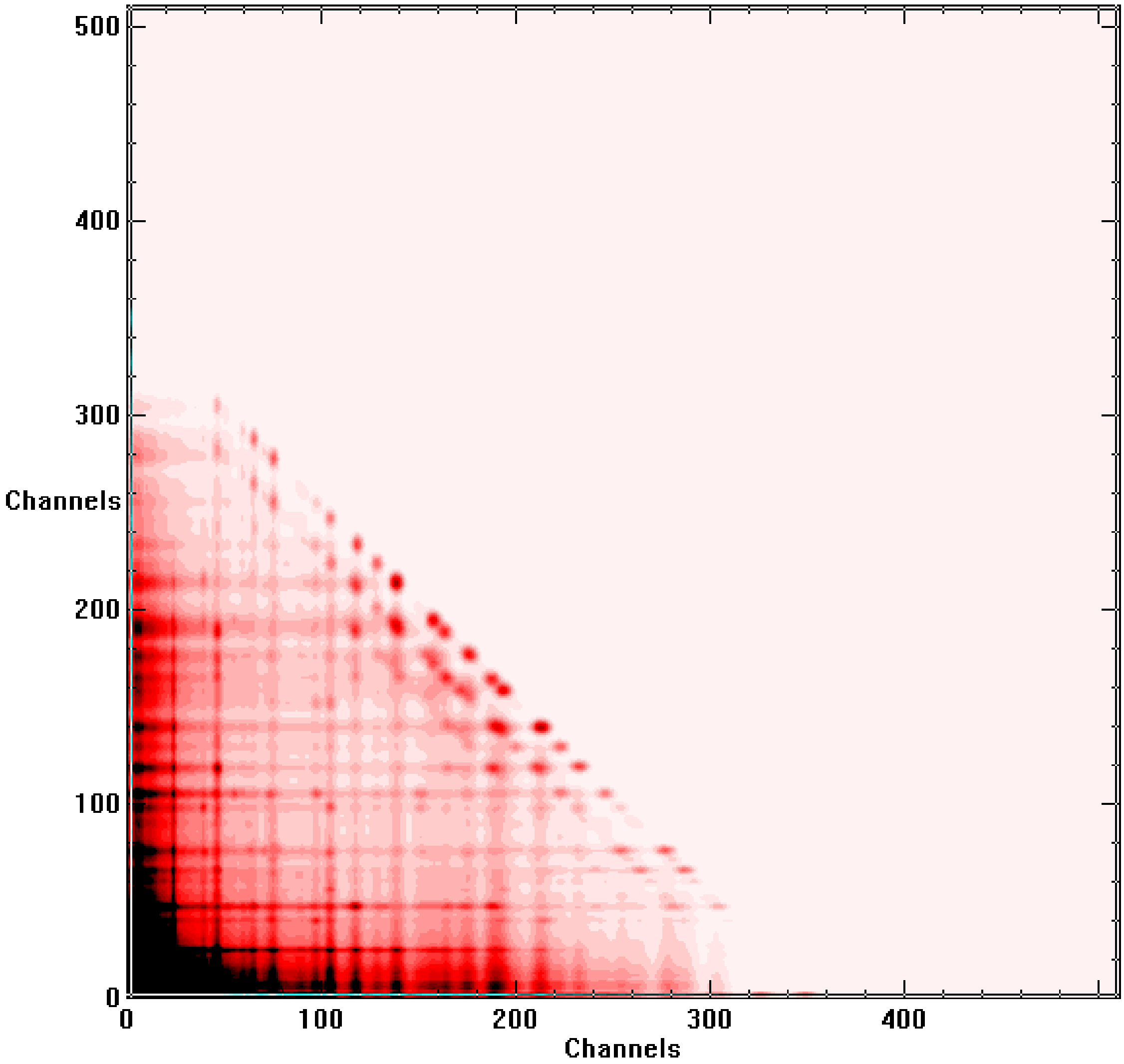

Coincidence from Aluminum in Sample (0-10000 counts)

Q-Value: 7.724 MeV

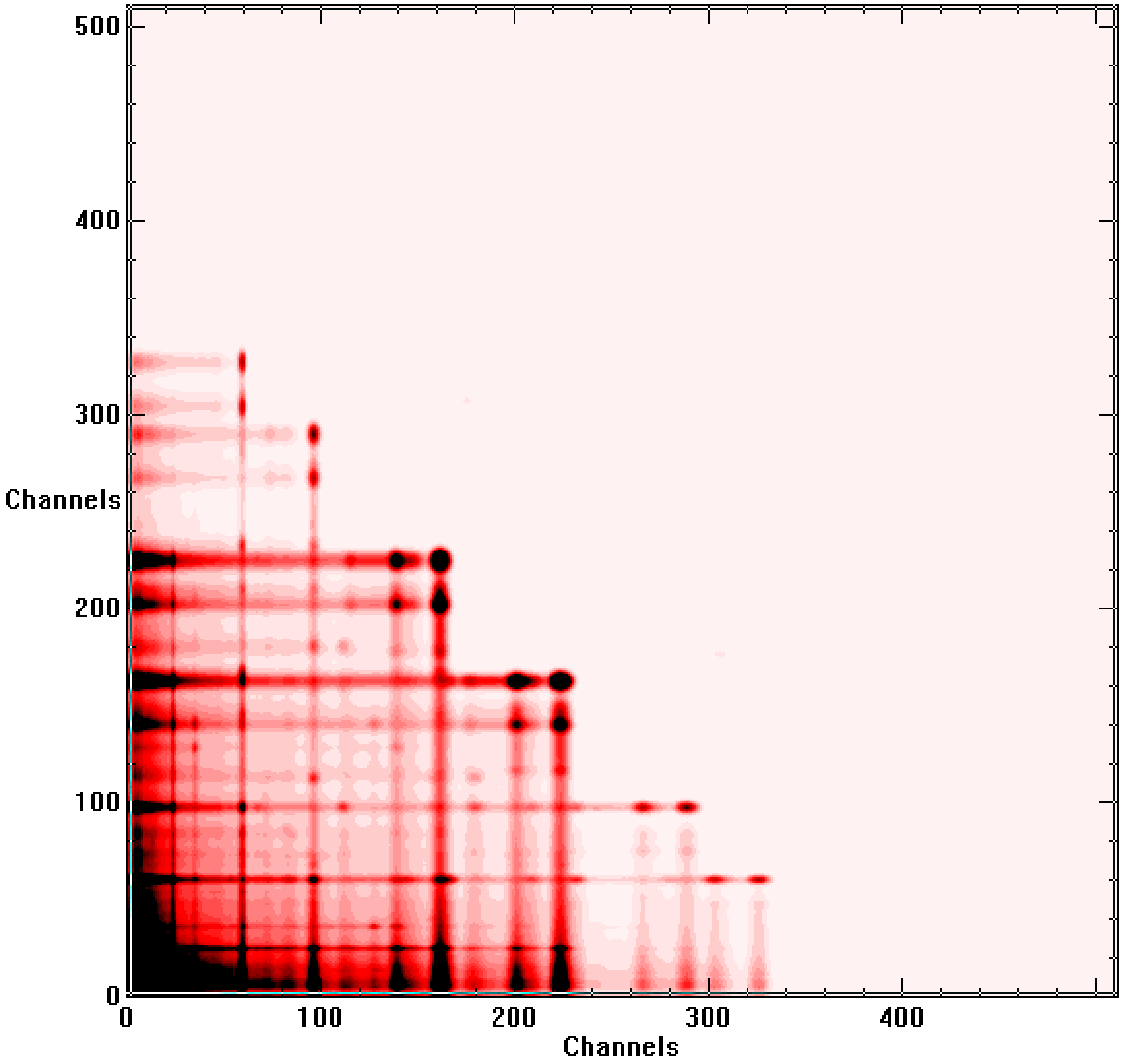

Coincidence from Silicon in Sample (0-50000 counts)

Isotopes	Abundance (%)	Q-Value(MeV)
Si-28	92.23	8.472
Si-29	4.68	10.607
Si-30	3.09	6.586

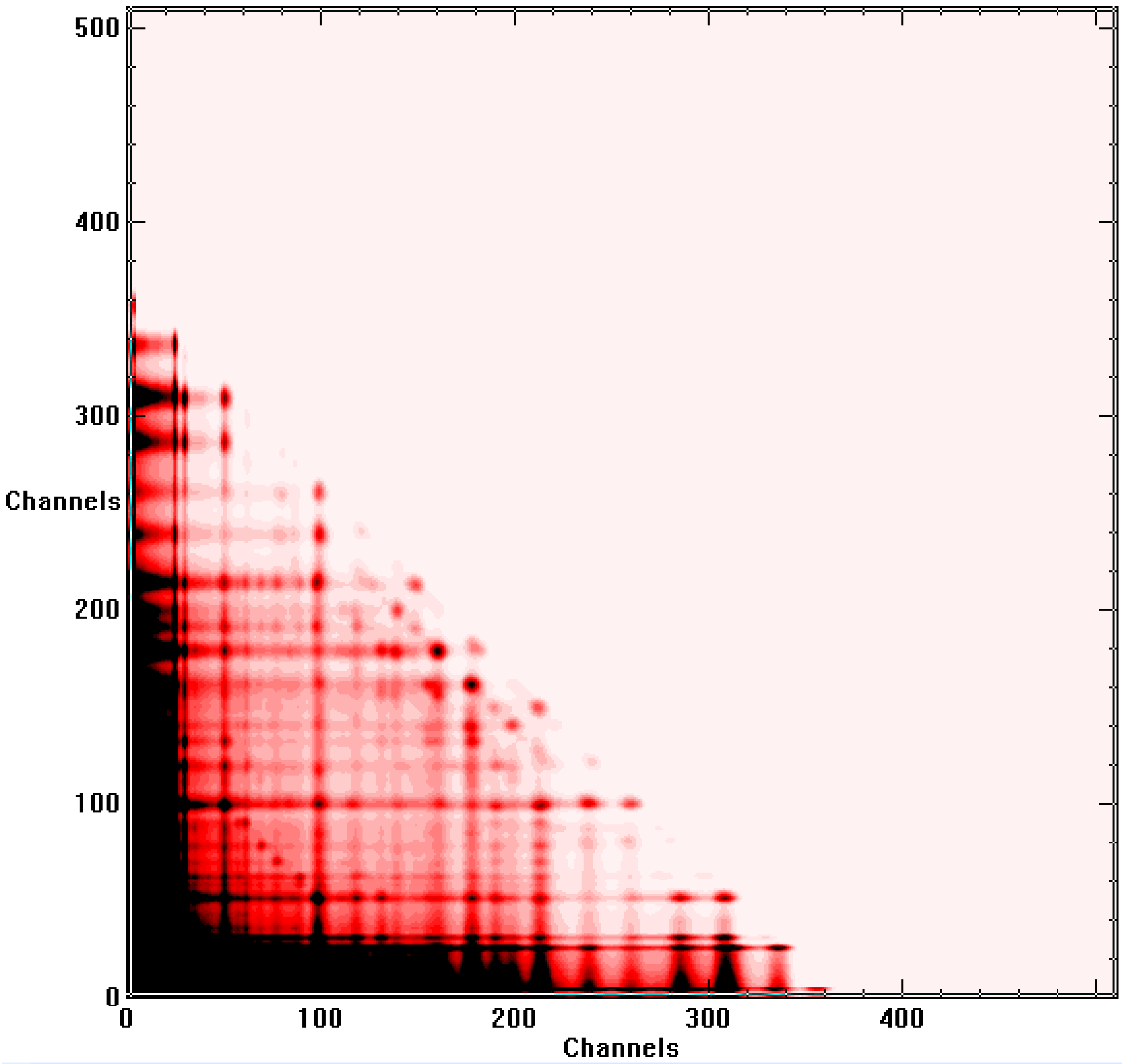

Coincidence from Phosphorous in Sample (0-200 counts)

Q-Value: 7.934 MeV

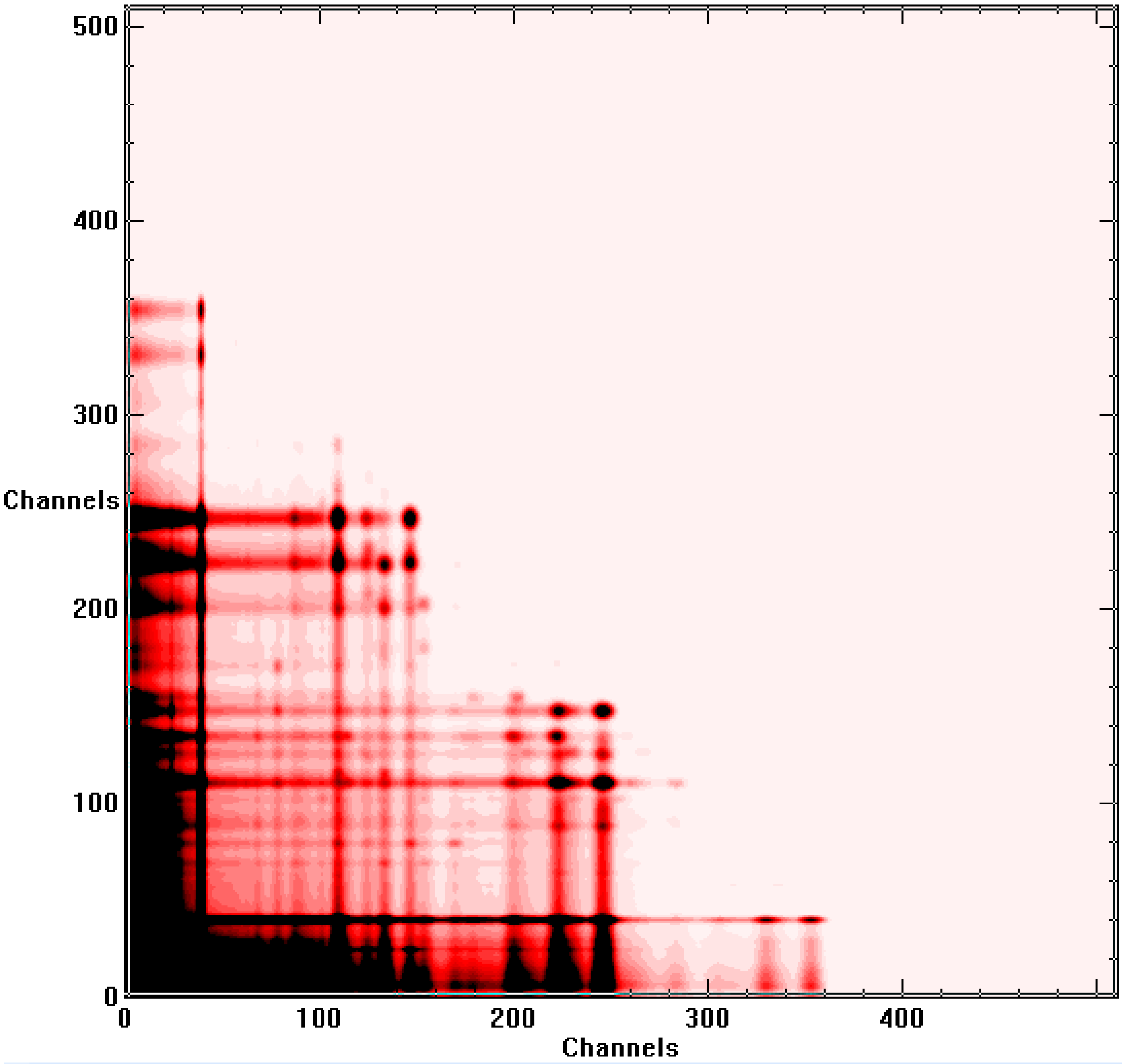

Coincidence from Sulfur in Sample (0-5000 counts)

Q-Value: 8.641 MeV (only S-32 is considered)

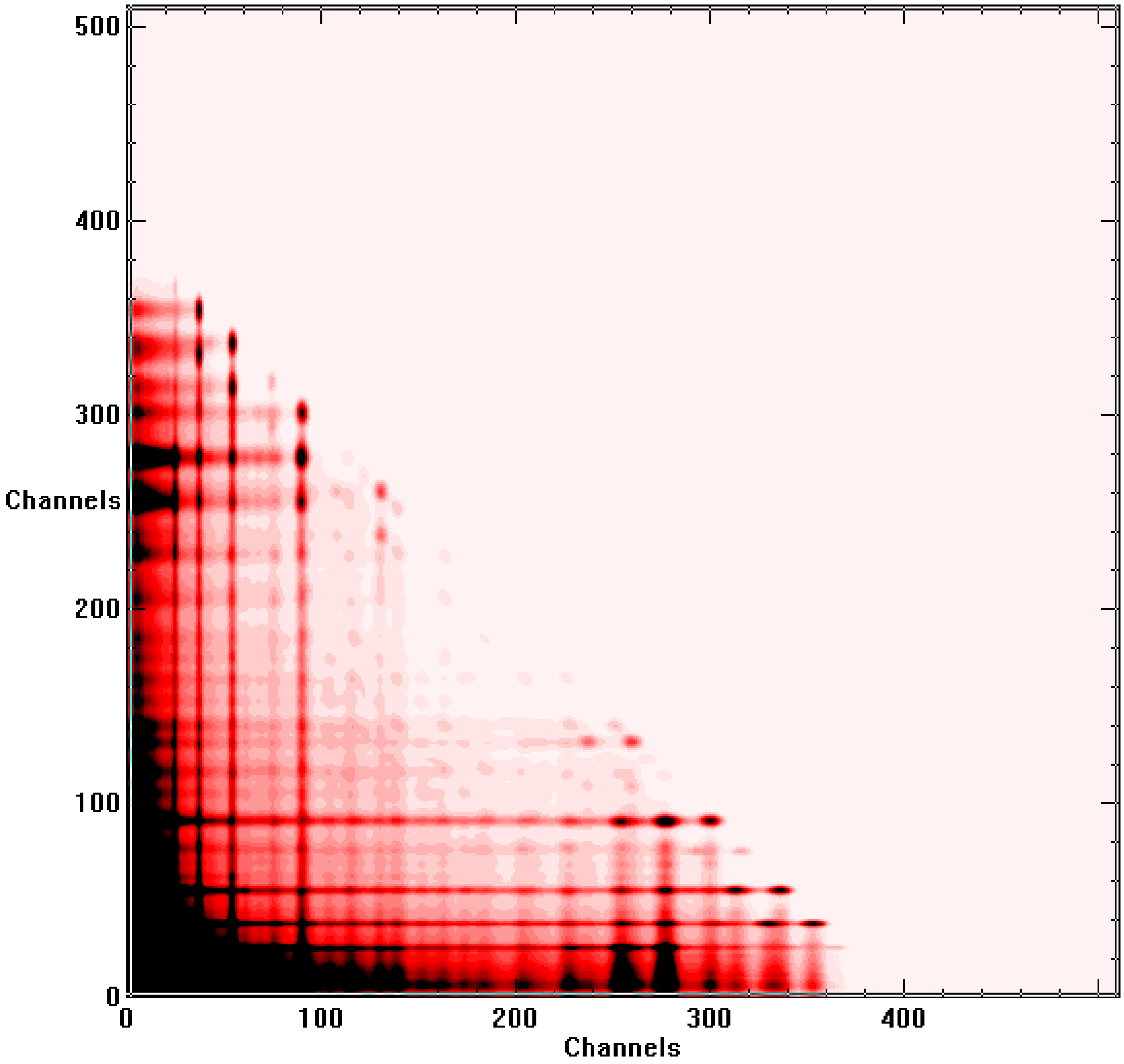

Coincidence from Chlorine in Sample (0-300000 counts)

Isotopes	Abundance (%)	Q-Value(MeV)
Cl-35	75.78	8.579
Cl-37	24.22	6.107

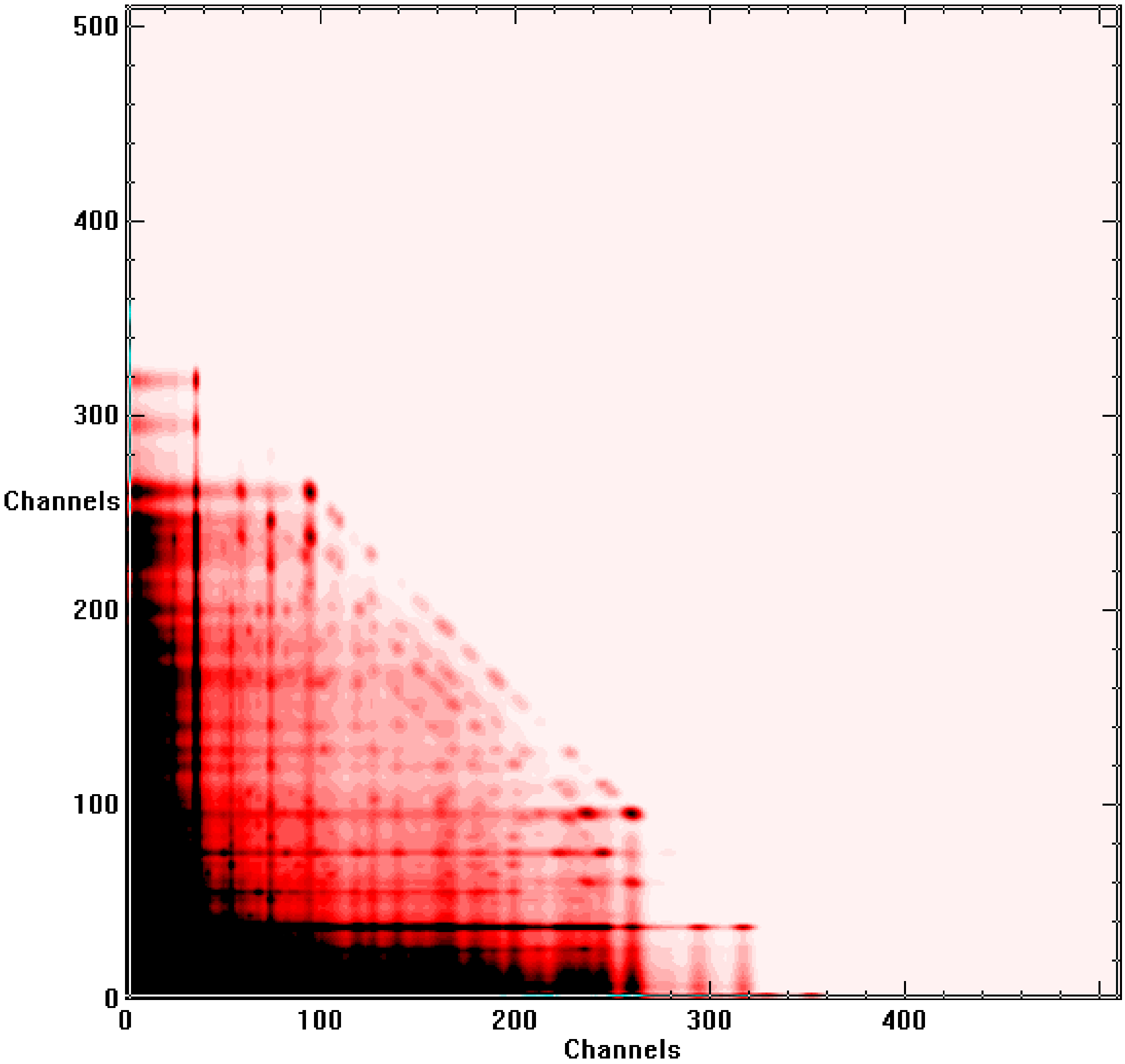

Coincidence from Potassium in Sample (0-3000 counts)

Q-Value: 7.769 MeV (only K-39 is considered)

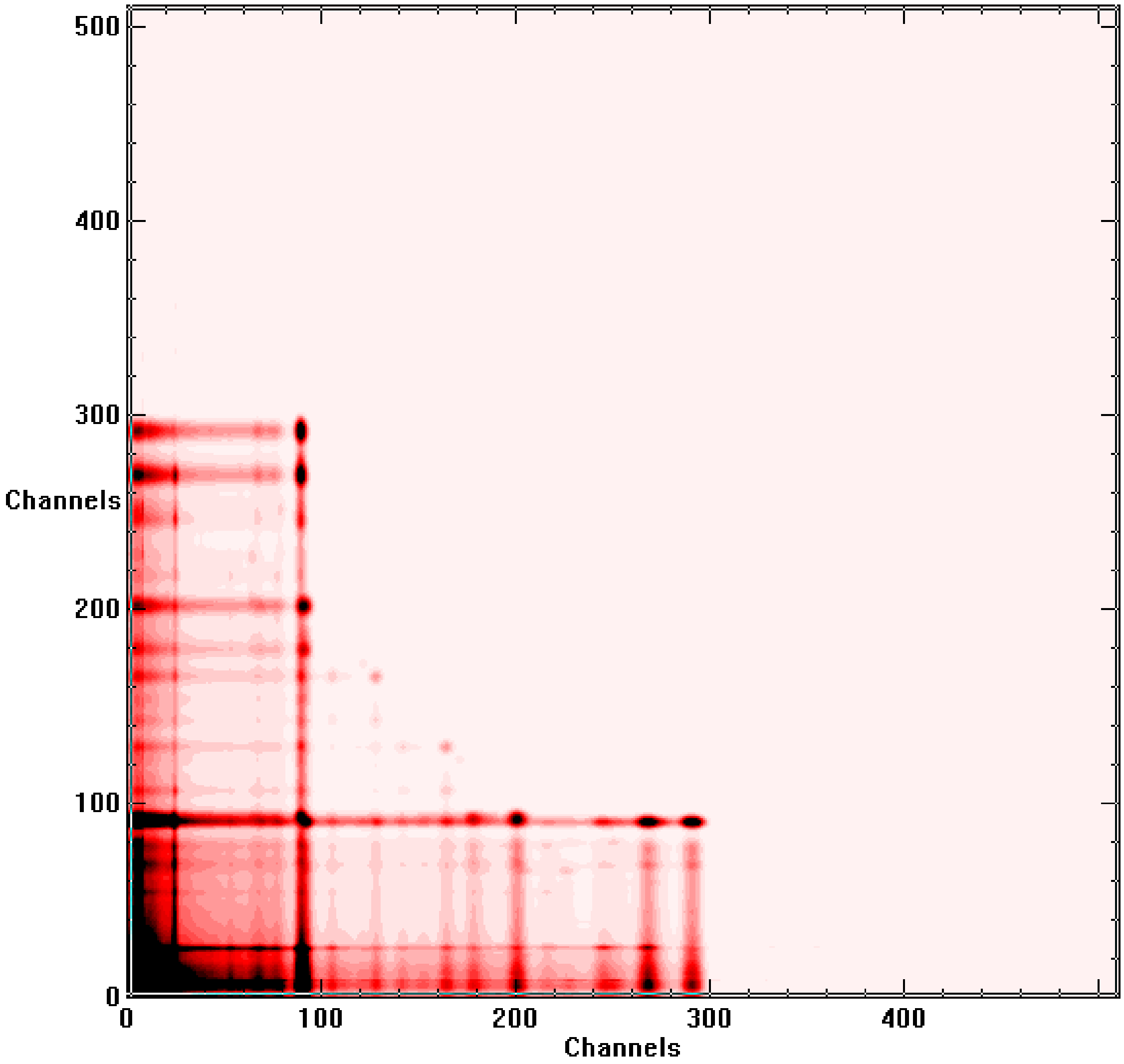

Coincidence from Calcium in Sample (0-3000 counts)

Isotopes	Abundance (%)	Q-Value(MeV)
Ca-40	96.94	6.419
Ca-44	2.09	5.980

*Other isotopes are not considered here.

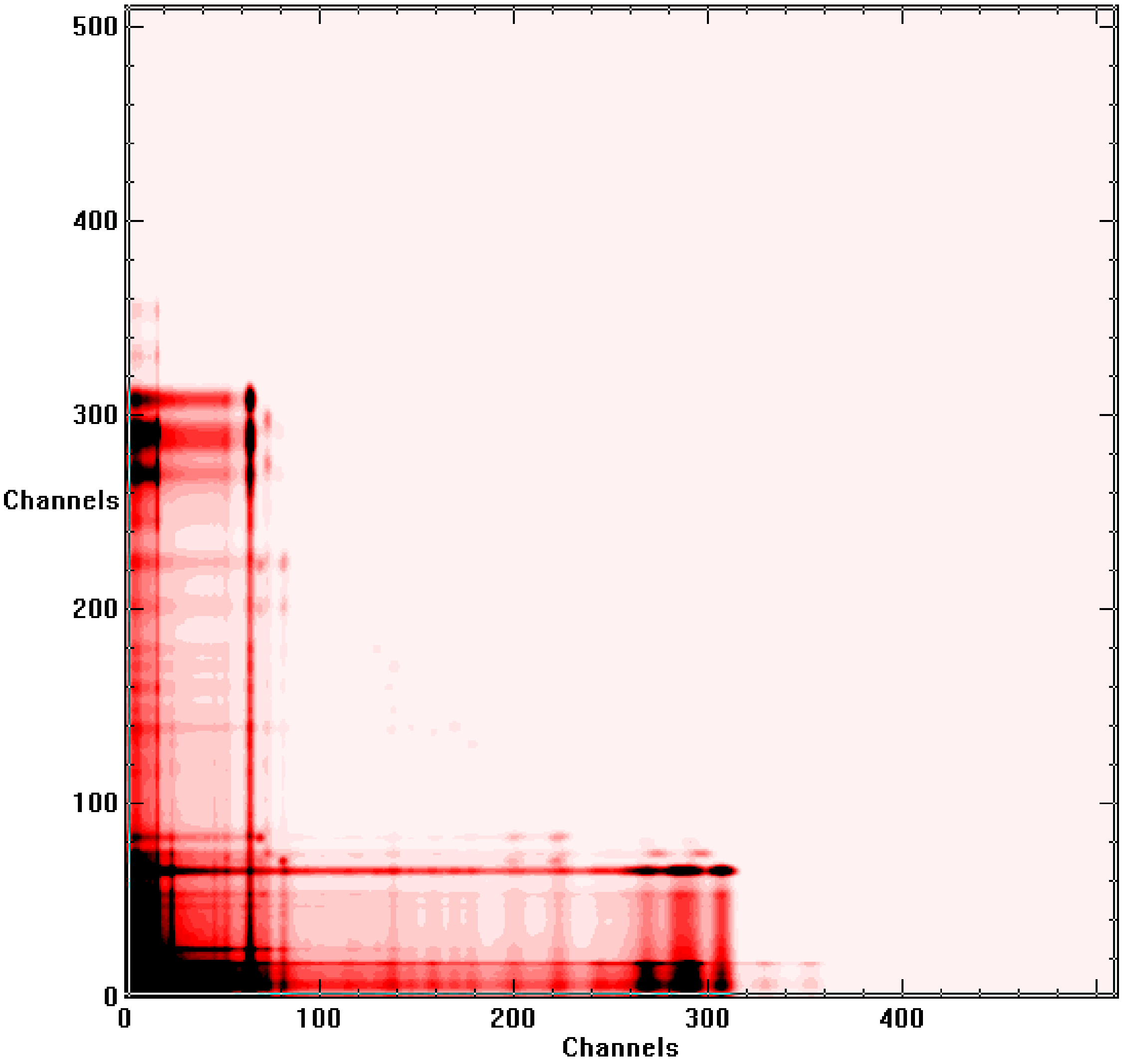

Coincidence from Titanium in Sample (0-30000 counts)

Isotopes	Abundance (%)	Q-Value(MeV)
Ti-46	8.25	7.330
Ti-47	7.44	10.642
Ti-48	73.72	6.760
Ti-49	5.41	9.384
Ti-50	5.18	6.373

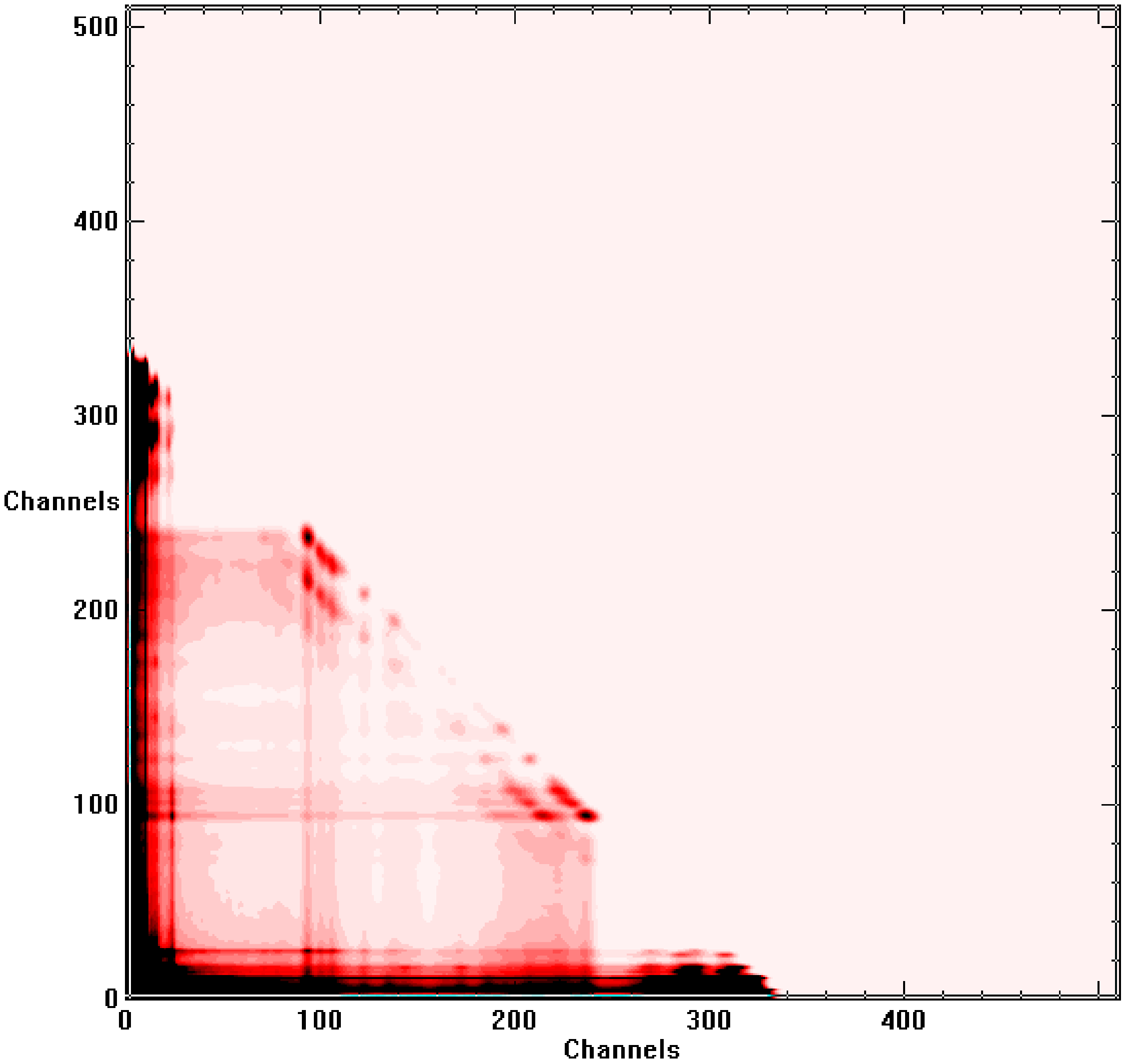

Coincidence from Manganese in Sample (0-3000 counts)

Q-Value: 7.270 MeV

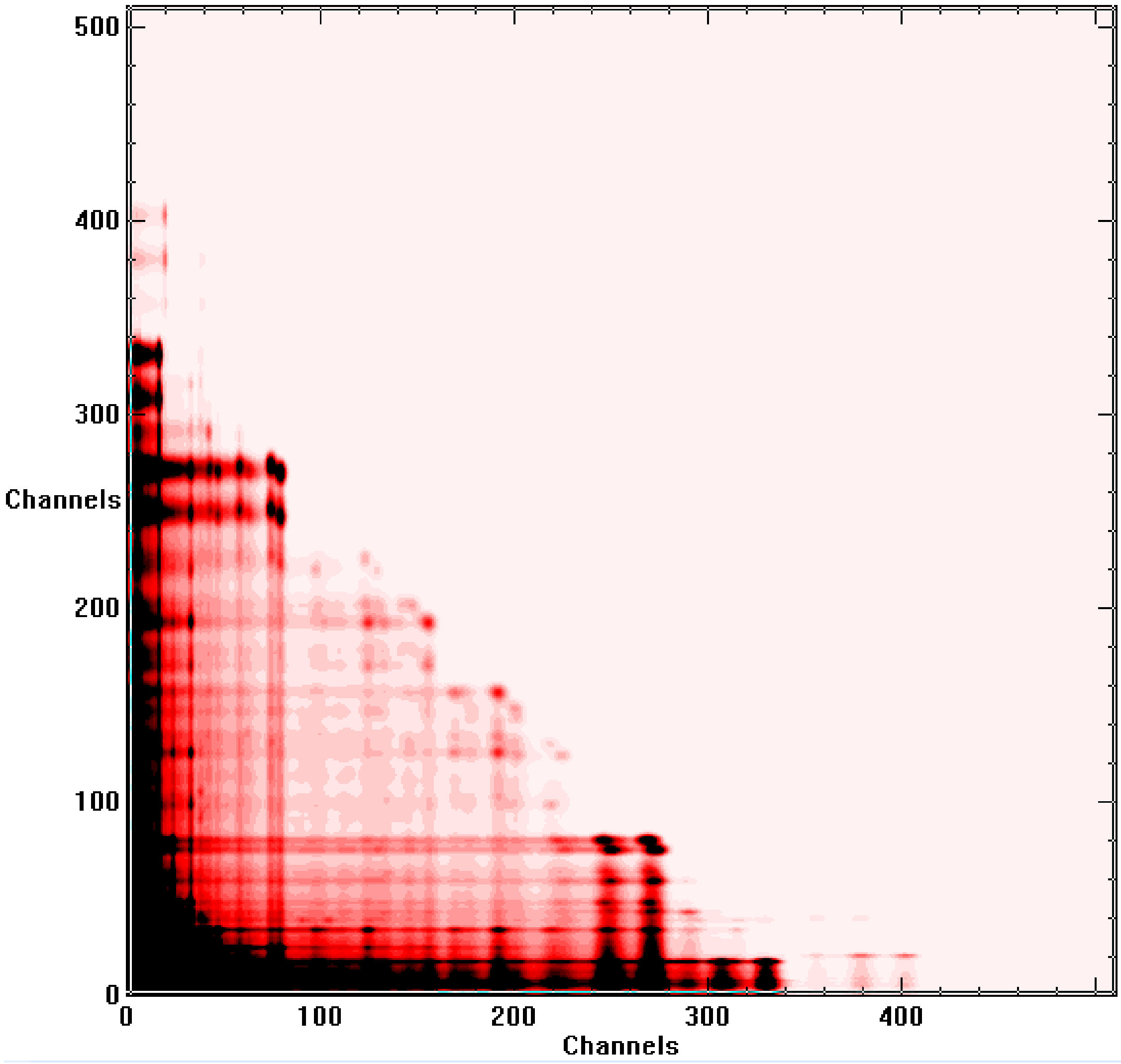

Coincidence from Iron in Sample (0-10000 counts)

Isotopes	Abundance (%)	Q-Value(MeV)
Fe-54	5.845	9.298
Fe-56	91.754	7.646
Fe-57	2.119	8.369

*Other isotopes are not considered here.

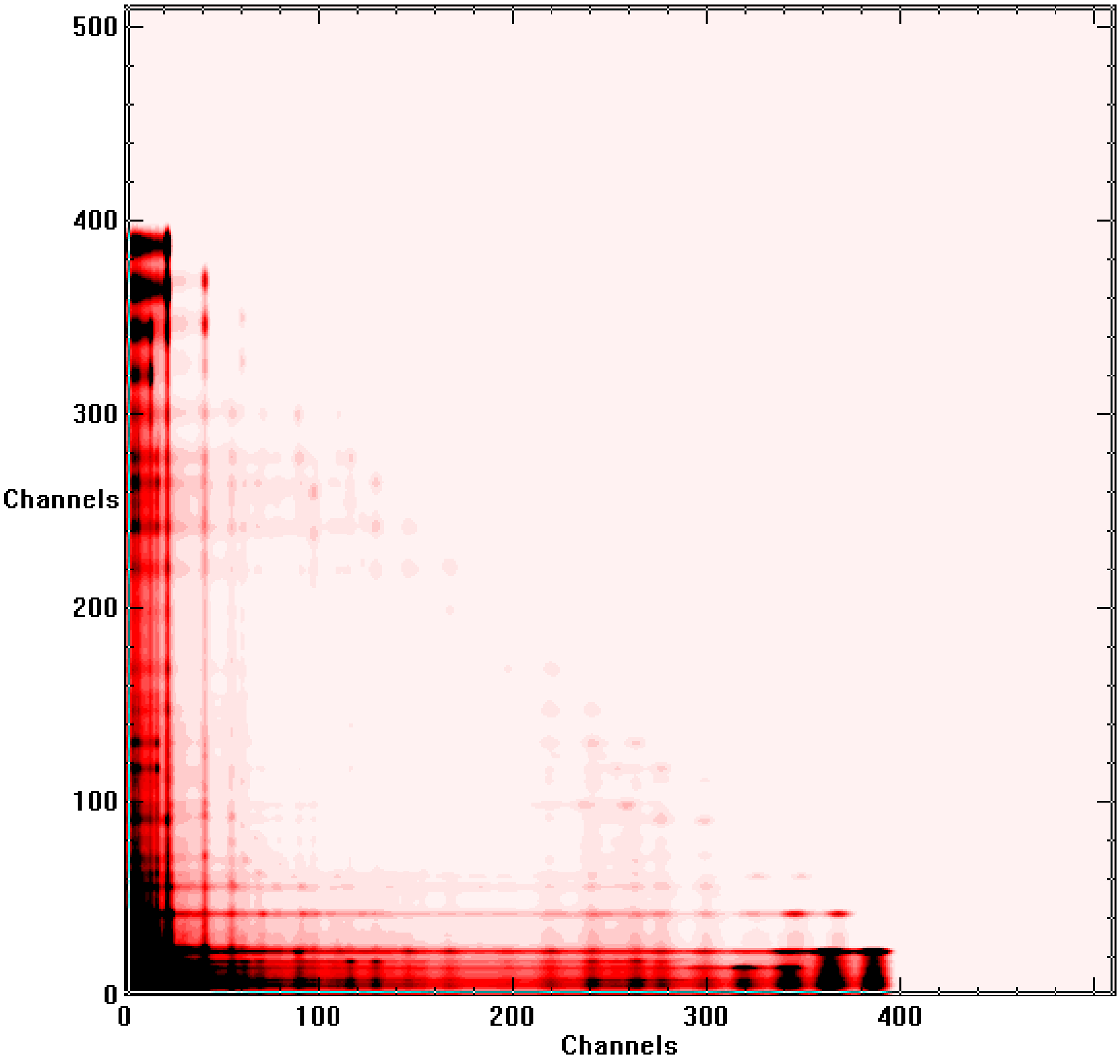

Coincidence from Nickel in Sample (0-300 counts)

Isotopes	Abundance (%)	Q-Value(MeV)
Ni-58	68.08	8.998
Ni-60	26.22	7.820
Ni-61	1.140	10.595
Ni-62	3.63	6.838

*Other isotopes are not considered here.

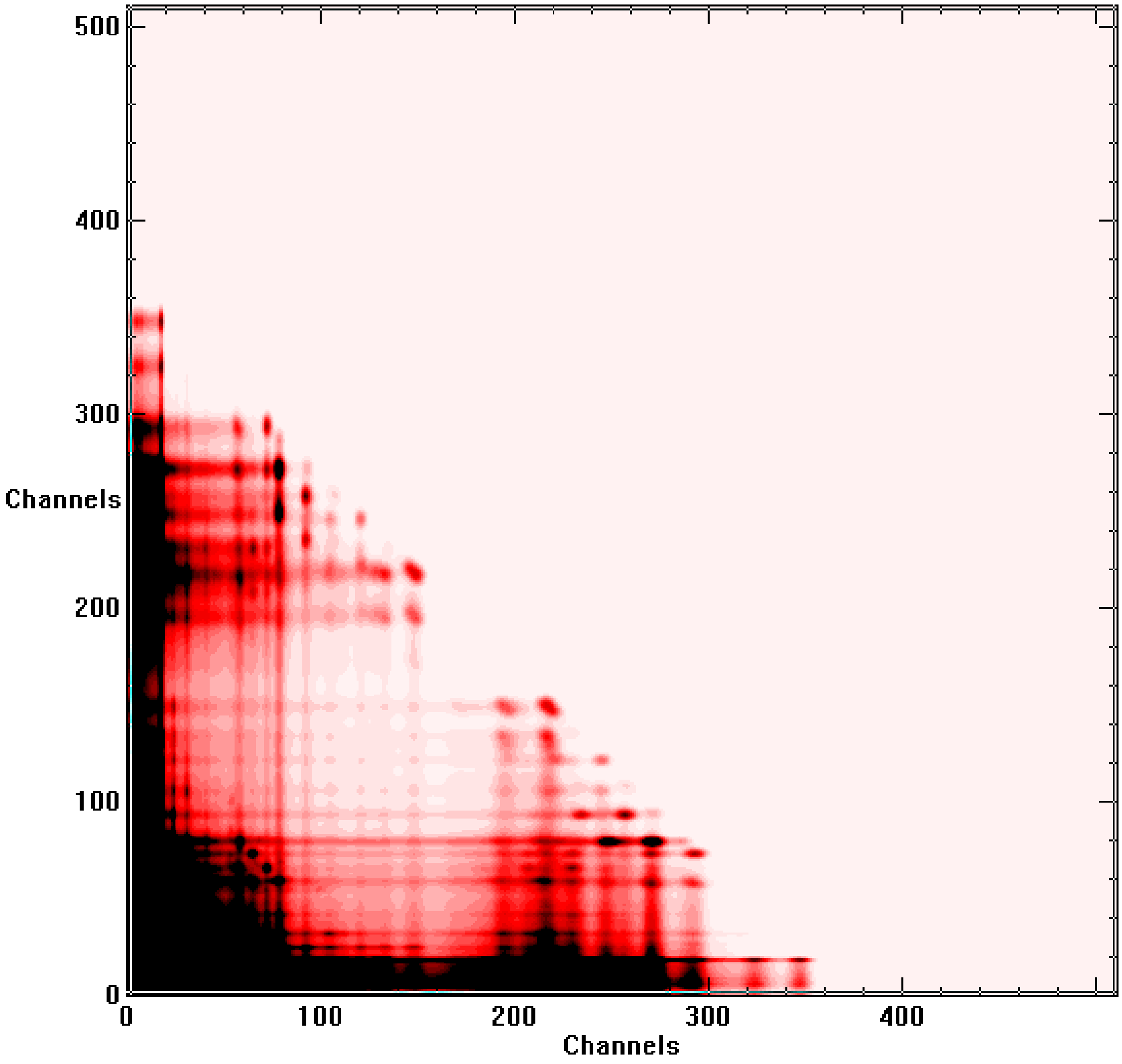

Coincidence from Mercury in Sample (0-50000 counts)

Q-Value: 8.028 MeV (only Hg-199 is considered)